Planar Near-Field Measurements of GPR Antennas and Applications to Imaging

Lenler-Eriksen, Hans-Rudolph

Publication date:
2006

Document Version
Publisher's PDF, also known as Version of record

Planar Near-Field Measurements of GPR Antennas and Applications to Imaging

Hans-Rudolph Lenler-Eriksen

April 2006

The present work was carried out at Ørsted-DTU in partial fulfillment of the requirements for the Ph.D. degree from the Technical University of Denmark. This is a revised version of the original thesis.

Supervisor: Associate Professor Peter Meincke, Ph.D.

Abstract

Planar Near-Field Measurements of GPR Antennas and Applications to Imaging

Ground penetrating radar (GPR) systems are used for detection of objects in soil. The objects are detected by transmission of an electromagnetic field in the soil from a transmitting antenna. The transmitted electromagnetic field causes a scattered electromagnetic field by interactions with the objects in the soil, and the scattered field is detected by a receiving antenna. The detected scattered electromagnetic field contains information about the shape and position of the objects in the soil. To obtain a good extraction of information about the objects in the soil as much a priory information as possible should be used. Knowledge about the electromagnetic properties of the soil like the velocity of propagation is necessary. Furthermore, knowledge about the electromagnetic properties of the antennas is desirable. For non-dispersive and linearly polarized antennas it is often sufficient to simulate the antennas as simple Hertzian dipoles.

In this thesis GPR antennas are characterized by the transmitted electromagnetic field in the soil. The transmitted electromagnetic field can be written as a superposition of plane waves by means of a plane-wave transmitting spectrum. The plane-wave transmitting spectrum can be calculated using measurements of the voltage transfer function between the GPR antenna and a buried loop antenna in the soil. To perform the calculations, knowledge of the electromagnetic properties of the soil and the loop antenna is necessary. The electromagnetic properties of the loop antenna are described using a plane-wave receiving spectrum that expresses the sensitivity to the transmitted electromagnetic plane waves in the soil. Development of methods for estimation of the electromagnetic properties of the soil is also important.

Subsequently, the calculated plane-wave transmitting spectra are used in a method for image reconstruction of objects in the soil. This method gives a possibility to use the GPR system with an arbitrary antenna for imaging provided that the scattered field from the objects in the soil is detectable. In this thesis two types of antennas are measured and used for image reconstruction. These antennas are a non-dispersive linearly polarized bowtie antenna and a dispersive circularly polarized equiangular spiral antenna, respectively. The experimental work shows that both types of antennas are suitable as GPR antennas if the plane-wave transmitting spectrum is used in the imaging reconstruction.

Resumé (in Danish)

Plane nærfeltsmålinger af GPR antenner og anvendelse af disse til billeddannelse

GPR (ground penetrating radar) systemer bruges til detektering af objekter i jorden. Disse systemer fungerer ved at en elektromagnetisk bølge transmitteres til jorden fra en senderantenne. Det transmitterede elektromagnetiske felt giver anledning til et spredt electromagnetisk felt ved objekterne i jorden, som derefter detekteres med en modtagerantenne. Det detekterede spredte elektromagnetiske felt indeholder informationer om objekternes form og position i jorden. For at få en god ekstrahering af information om objekterne i jorden, gælder det om at anvende så meget a priori-viden som muligt. Det er nødvendigt at have kendskab til jordens elektromagnetiske egenskaber, så som udbredelseshastigheden for de elektromagnetiske bølger. Det er ligeledes ønskeligt at anvende informationer om de anvendte antenner. For ikke-dispersive og lineært polariserede antenner er det ofte tilstrækkeligt at simulere antennerne som simple punktkilder i form af Hertz-dipoler.

I denne afhandling karakteriseres GPR-antenner ved det transmitterede elektromagnetiske felt i jorden. Det transmitterede elektromagnetiske felt kan skrives som en superposition af plane bølger, der kan udtrykkes ved hjælp af et sendeplanbølgespektrum. Sendeplanbølgespektret kan beregnes ud fra målinger af overføringsfunktionen mellem en GPR-antenne og en nedgravet loop-antenne. Beregningerne forudsætter et kendskab til jordens og loop-antennens elektromagnetiske egenskaber. Loop-antennens elektromagnetiske egenskaber beskrives ved hjælp af et modtageplanbølgespektrum, der beskriver loop-antennens sensitivitet over for de transmitterede plane bølger i jorden. Udvikling af metoder til estimering af jordens elektromagnetiske egenskaber er ligeledes væsentlig.

De beregnede sendeplanbølgespektra er derefter blevet anvendt i en metode til billeddannelse af objekter i jorden. Denne metode giver mulighed for at anvende en vilkårlig antenne til billeddannelse såfremt det spredte elektromagnetiske felt fra objekterne i jorden er måleligt. Bredbåndede dispersive antenner med en vilkårlig polarisering kan derfor anvendes med denne metode. To antennetyper bliver målt og anvendt til billeddannelse i denne afhandling. Den ene antennetype er bowtie-antennen, der er en ikke-dispersiv lineært polariseret antenne. Den anden antennetype er den plane spiral-antennne, der er en dispersiv cirkulært polariseret antenne. Det eksperimentelle arbejde viser, at begge antennetyper er velegnede GPR-antenner, såfremt at sendeplanbølgespektret for antennerne anvendes.

Preface

This thesis was carried out at the Section for Electromagnetic Systems, Ørsted·DTU, Technical University of Denmark (DTU). The work was started in September 2002 and finished in April 2006. Six months were spent as visiting scholar at Norges Teknisk-Naturvitenskapelige Universitet (NTNU) in Trondheim in the spring of 2004.

I want to express my gratitude to my supervisor Peter Meincke for numerous fruitful discussions and continuous support. I would also like to thank Brian Karlsen for support and inspiration. Brian has done a great work on the measurement facility and we have had fruitful discussions about practical problems in the facility and about the application of ground penetrating radar systems. I also wish to acknowledge the help of a number of people: Erik Jørgensen, Sergey Pivnenko, Kaj Bjarne Jakobsen, Jesper Thaysen, Tommi Laitinen, and Tonny Rubæk.

I would also like to thank for the co-operation with Antenna Centre of Excellence (ACE). It has been a pleasure to do measurements of ground penetrating radar antennas during December 2004.

I thank Dr. Egil Eide for his hospitality during my stay in Trondheim. It was a pleasure to work with the antenna arrays produced by 3d-radar and designed by Dr. Egil Eide. I thank Sigve Tjora, Bjørn Pedersen, and Pål-Aanund Sandnes for discussions.

Finally, I thank Birgitte Helleshøj for carefully proof reading the manuscript.

Hans-Rudolph Lenler-Eriksen, April 2006.

List of Symbols

Greek Symbols	Decription	Unit
α_ω	Loss constant, p. 27.	dBm^{-1}
α	Constant, Eq. (3.30).	
ε_0	Permittivity in free space.	Fm^{-1}
ε_1	Frequency independent permittivity of the soil, p. 76 and p. 77.	Fm^{-1}
$\varepsilon_{1,\omega}$	Complex permittivity in the soil, p. 11.	Fm^{-1}
$\varepsilon'_{1,\omega}$	Real part of the complex permittivity in the soil, p. 11.	Fm^{-1}
$\varepsilon''_{1,\omega}$	Imaginary part of the complex permittivity in the soil, p. 11.	Fm^{-1}
ε'_1	Frequency independent imaginary part of the complex permittivity in the soil, p. 34.	Fm^{-1}
$\varepsilon_{c,\omega}$	Complex permittivity of a good conductor, p. 7.	Fm^{-1}
$\varepsilon'_{c,\omega}$	Real part of the complex permittivity of a good conductor, p. 7.	Fm^{-1}
$\varepsilon''_{c,\omega}$	Imaginary part of the complex permittivity of a good conductor, p. 7.	Fm^{-1}
$\varepsilon_{d,\omega}$	Complex permittivity of dielectric, p. 7.	Fm^{-1}
$\varepsilon'_{d,\omega}$	Real part of the complex permittivity of dielectric, p. 7.	Fm^{-1}
$\varepsilon''_{d,\omega}$	Imaginary part of the complex permittivity of dielectric, p. 7.	Fm^{-1}
$\varepsilon_{n,\omega}$	Complex permittivity of soil, Eq. (3.30).	Fm^{-1}
$\varepsilon_{ST,\omega_{ST}}$	Complex permittivity of dielectric, p. 28.	Fm^{-1}
$\varepsilon'_{ST,\omega_{ST}}$	Real part of the permittivity of dielectric, p. 28.	Fm^{-1}
$\varepsilon''_{ST,\omega_{ST}}$	Imaginary part of the complex permittivity, p. 28.	Fm^{-1}
$\varepsilon_{p,\omega}$	Complex permittivity of soil particles, Eq. (3.39).	Fm^{-1}
$\varepsilon'_{p,\omega}$	Real part of the complex permittivity of soil particles, Eq. (3.39).	Fm^{-1}
$\varepsilon''_{p,\omega}$	Imaginary part of the complex permittivity of soil particles, Eq. (3.39).	Fm^{-1}
$\varepsilon_{b,\omega}$	Complex permittivity of bounded water, Eq. (3.39).	Fm^{-1}
$\varepsilon'_{b,\omega}$	Real part of the complex permittivity of bounded water, Eq. (3.39).	Fm^{-1}
$\varepsilon''_{b,\omega}$	Imaginary part of the complex permittivity of bounded water, Eq. (3.39).	Fm^{-1}
$\varepsilon_{b,0}$	Permittivities of bounded water at zero frequency, p. 43.	Fm^{-1}
$\varepsilon_{b,\infty}$	Permittivities of bounded water at an infinitely high frequency, p. 43.	Fm^{-1}
$\varepsilon_{\mathrm{sca},\omega}$	Permittivity of the scatterer in the soil, p. 77.	Fm^{-1}
$\varepsilon_{u,\omega}$	Complex permittivity of unbounded water, Eq. (3.39).	Fm^{-1}
$\varepsilon'_{u,\omega}$	Real part of the complex permittivity of unbounded water, Eq. (3.39).	Fm^{-1}
$\varepsilon''_{u,\omega}$	Imaginary part of the complex permittivity of unbounded water, Eq. (3.39).	Fm^{-1}
$\varepsilon_{u,0}$	Permittivities of unbounded water at zero frequency, p. 43.	Fm^{-1}
$\varepsilon_{u,\infty}$	Permittivities of unbounded water at an infinitely high frequency, p. 43.	Fm^{-1}
$\varepsilon_{ds,\omega}$	Complex permittivity of dry soil, Eq. (3.41).	Fm^{-1}
$\varepsilon'_{ds,\omega}$	Real part of the complex permittivity of dry soil, Eq. (3.41).	Fm^{-1}

$\varepsilon''_{ds,\omega}$	Imaginary part of the complex permittivity of dry soil, Eq. (3.41).	Fm^{-1}
μ_0	Permeability in free space	Hm^{-1}
$\gamma_{0,\omega}$	The $\hat{\mathbf{z}}$-component of the wavevector $\mathbf{k}^{\pm}_{0,\omega}$ in free space as defined in equation (2.7).	m^{-1}
$\gamma_{1,\omega}$	The $\hat{\mathbf{z}}$-component of the wavevector $\mathbf{k}^{\pm}_{1,\omega}$ in free space as defined in equation (2.23).	m^{-1}
$\gamma_{c,\omega}$	Propagation constant, p. 27.	m^{-1}
$\Gamma_{A1,\omega}$	Reflection coefficient of the GPR antenna, Eq. (2.29).	
$\Gamma_{A11,\omega}$	Reflection coefficient of GPR antenna 1 with no object in the soil, Eq. (5.2).	
$\Gamma_{A22,\omega}$	Reflection coefficient of GPR antenna 2 with no object in the soil, Eq. (5.2).	
$\Gamma_{A21,\omega}$	Transfer function between GPR antenna 1 and 2 with no objects in the soil, Eq. (5.2).	
$\Gamma_{A12,\omega}$	Transfer function between GPR antenna 2 and 1 with no objects in the soil, Eq. (5.2).	
ω	Angular frequeny $\omega = 2\pi f$	s^{-1}
ω_{min}	Minimum angular frequeny used for image reconstruction, Eq. (5.21).	s^{-1}
ω_{max}	Maximum angular frequeny used for image reconstruction, Eq. (5.21).	s^{-1}
ω_{ST}	Angular frequeny used for calculation of the current distribution at the loop antenna, p. 28.	s^{-1}
$\lambda_{0,\omega}$	Wavelength in free space $\lambda_{0,\omega} = \frac{2\pi}{k_{0,\omega}}$, p. 6.	m
$\lambda_{1,\omega}$	Wavelength in the soil $\lambda_{1,\omega} = \frac{2\pi}{\omega\sqrt{\mu_0\varepsilon'_{1,\omega}}}$, Eq. 2.17.	m
$\sigma_{1,\omega}$	Conductivity of soil, p. 37.	Sm^{-1}
$\sigma_{c,\omega}$	Conductivity of good conductor, p. 7.	Sm^{-1}
σ_{Ag}	Conductivity of silver, p. 25.	Sm^{-1}
σ_{Cu}	Conductivity of cobber, p. 25.	Sm^{-1}
σ_1	Frequency independent conductivity, p. 34.	Sm^{-1}
ς_{phase}	Error-function, Eq. (3.27).	
ρ	Coordinate in cylindrical coordinate system, p. 6.	m
ρ_0	Initial outer radius of spiral arm, p. 63.	m
ρ_1	Outer radius of spiral arm, p. 63.	m
ρ_2	Inner radius of spiral arm, p. 63.	m
ϕ	Coordinate in cylindrical coordinate system, p. 6.	rad
ϕ_0	Constant, Eq. (3.48).	rad
$\overline{\mathbf{L}}_{01,\omega}$	Transmission dyadic, Eq. (2.33).	
$\eta_{A,\omega}$	Transmission efficiency, Eq. (2.37).	
η_A	The total transmission efficiency, Eq. (2.51).	
$\eta_{Ax,\omega}$	Partial transmission efficiency, Eq. (2.38).	
$\eta_{Ay,\omega}$	Partial transmission efficiency, Eq. (2.39).	
$\eta_{Arhcp,\omega}$	Partial transmission efficiency, Eq. (2.43).	

$\eta_{Alhcp,\omega}$	Partial transmission efficiency, Eq. (2.44).	
$\boldsymbol{W}_{nP,\omega}$	Vector for probe n, $n = 1, 2$, Eq. (2.59) .	
$\tan\delta_{1,\omega}$	Loss tangent of the soil, p. 12.	
$\tan\delta_{c,\omega}$	Loss tangent of good conductor, p. 7.	
$\tan\delta_{d,\omega}$	Loss tangent of dielectric, p. 7.	
$\tan\delta_{ST,\omega_{ST}}$	Loss tangent of soil, p. 28.	
Φ_ω	Angle between $\boldsymbol{W}_{1,\omega}$ and $\boldsymbol{W}_{2,\omega}$, Eq. (2.63).	rad
ξ	Maximum for $\lvert\cos(\Phi_\omega)\rvert$, p. 19.	
Δl	Length of Hertzian dipole, Eq. (4.4).	m
Δt	Two-way travel time, p. 27.	s
ΔC	Shunt capacitance, p. 31.	F
ΔG	Shunt conductance, p. 31.	S
Δx	Horizontal resolution, Eq. (5.22).	m
Δy	Horizontal resolution, Eq. (5.22).	m
Δz	Vertical resolution, Eq. (5.22).	m
$\Delta\sigma_{1,\omega}$	Uncertainty of the estimated conductivity, Eq. (3.47).	Sm^{-1}
$\Delta\varepsilon_{1,\omega}$	Uncertainty of the estimated conductivity, Eq. (3.49).	Fm^{-1}
$\Delta\varepsilon_\omega$	Difference between the permittivity of the object and the soil, Eq. (5.5).	Fm^{-1}
$\widetilde{\Delta\varepsilon}_\omega$	Fourier-transformed difference between the permittivity of the object and the soil, Eq. (5.8).	Fm
τ_b	Relaxation times for bounded water, p. 43.	s
τ_u	Relaxation times for free water, p. 43.	s

Roman Symbols	**Decription**	**Unit**
a	Radius of center conductor in coaxial cable, p. 7.	m
a_0	Growth rate of spiral antennna, p. 63.	rad^{-1}
a_c	Slope, p. 41	$\text{Sm}^{-1}\text{Hz}^{-1}$
a_Δ	Frequency independent object function, p. 79	
$\widetilde{a}_\Delta$	Fourier-transformed object function, Eq. (5.14).	m^3
$\overline{\mathbf{A}}$	Matrix, p. 75.	
b	Radius of outer conductor in coaxial cable, p. 7.	m
$b_{\Delta,\omega}$	Factor, p. 79	Fm^{-1}
$\mathbf{b}$	Vector, p. 75.	
B	Bandwidth of frequencies, Eq. (5.22).	Hz
$B_{Zero-Offset}$	Object function for image reconstruction, Eq. (5.29).	
$B_{Fixed-offset}$	Object function for image reconstruction, Eq. (5.30).	
c_1	Velocity of propagation in the soil, Eq. (5.22).	ms^{-1}
c_0	Velocity of propagation in the free space, Eq. (5.24).	ms^{-1}
C_P	The circumference of the loop antenna, Eq. (3.22).	m
d	Parameter in Cosine roll-off window function, Eq. (5.27) and Eq. (5.28).	m
d_A	Distance, p. 36.	m
E_{rp}	Phase uncertainty of the reflection measurement, App. C.	rad
E_{tp}	Phase uncertainty of the transmission measurement, App. C.	rad
E_{rm}	Amplitude uncertainty of the reflection measurement, App. C.	
E_{tm}	Amplitude uncertainty of the transmission measurement, App. C.	
$\mathbf{E}^+_{0,t}$	The time-domain electric field of a wave propagating in the positive z-direction in the free space.	
	$\mathbf{E}^+_{0,t} = \hat{\mathbf{x}}E^+_{0x,t} + \hat{\mathbf{y}}E^+_{0y,t} + \hat{\mathbf{z}}E^+_{0z,t}$	Vm^{-1}
$\mathbf{E}^-_{0,t}$	The time-domain electric field of a wave propagating in the negative z-direction in the free space, Eq. (2.49).	
	$\mathbf{E}^-_{0,t} = \hat{\mathbf{x}}E^-_{0x,t} + \hat{\mathbf{y}}E^+_{0y,t} + \hat{\mathbf{z}}E^-_{0z,t}$	Vm^{-1}
$\mathbf{E}_{0,t}$	The total time-domain electric field in the free space.	
	$\mathbf{E}_{0,t} = \mathbf{E}^+_{0,t}. + \mathbf{E}^-_{0,t}$	Vm^{-1}
$\mathbf{E}^+_{1,t}$	The total time-domain electric field of a wave propagating in the positive z-direction in the soil.	
	$\mathbf{E}^+_{1,t} = \hat{\mathbf{x}}E^+_{1x,t} + \hat{\mathbf{y}}E^+_{1y,t} + \hat{\mathbf{z}}E^+_{1z,t}$	Vm^{-1}
$\mathbf{E}^-_{1,t}$	The time-domain electric field of a wave propagating in the negative z-direction.	
	in the soil $\mathbf{E}^-_{1,t} = \hat{\mathbf{x}}E^-_{1x,t} + \hat{\mathbf{y}}E^+_{1y,t} + \hat{\mathbf{z}}E^-_{1z,t}$	Vm^{-1}
$\mathbf{E}^+_{0,\omega}$	The frequency-domain electric field of a wave propagating in the positive z-direction in the free space, p. 7.	
	$\mathbf{E}^+_{0,\omega} = \hat{\mathbf{x}}E^+_{0x,\omega} + \hat{\mathbf{y}}E^+_{0y,\omega} + \hat{\mathbf{z}}E^+_{0z,\omega}$	Vsm^{-1}
$\mathbf{E}^-_{0,\omega}$	The frequency-domain electric field of a wave propagating in the negative z-direction in the free space, p. 7.	

	$\mathbf{E}^-_{0,\omega} = \hat{\mathbf{x}}E^-_{0x,\omega} + \hat{\mathbf{y}}E^-_{0y,\omega} + \hat{\mathbf{z}}E^-_{0z,\omega}$	Vsm^{-1}
$\mathbf{E}_{0,\omega}$	The total frequency-domain electric field in the free space, p. 7.	
	$\mathbf{E}_{0,\omega} = \mathbf{E}^+_{0,\omega} + \mathbf{E}^-_{0,\omega}$	Vsm^{-1}
$\mathbf{E}^+_{1,\omega}$	The frequency-domain electric field of a wave propagating in the positive z-direction in the soil, p. 11.	
	$\mathbf{E}^+_{1,\omega} = \hat{\mathbf{x}}E^+_{1x,\omega} + \hat{\mathbf{y}}E^+_{1y,\omega} + \hat{\mathbf{z}}E^+_{1z,\omega}$	Vsm^{-1}
$\mathbf{E}^-_{1,\omega}$	The frequency-domain electric field of a wave propagating in the negative z-direction in the soil, p. 11.	
	$\mathbf{E}^-_{1,\omega} = \hat{\mathbf{x}}E^-_{1x,\omega} + \hat{\mathbf{y}}E^-_{1y,\omega} + \hat{\mathbf{z}}E^-_{1z,\omega}$	Vsm^{-1}
$\mathbf{E}_{1,\omega}$	The total frequency-domain electric field in the soil.	
	$\mathbf{E}_{1,\omega} = \mathbf{E}^+_{1,\omega} + \mathbf{E}^-_{1,\omega}$.	Vsm^{-1}
$\mathbf{E}_{d,\omega}$	Electrictric field in dielectric, Eq. (2.3).	Vsm^{-1}
$\widetilde{\mathbf{E}}^+_{0,\omega}$	The frequency-domain and k-domain electric field of a wave propagating in the positive z-direction in the free space, Eq. (2.5).	
	$\widetilde{\mathbf{E}}^+_{0,\omega} = \hat{\mathbf{x}}\widetilde{E}^+_{0x,\omega} + \hat{\mathbf{y}}\widetilde{E}^+_{0y,\omega} + \hat{\mathbf{z}}\widetilde{E}^+_{0z,\omega}$	mVs
$\widetilde{\mathbf{E}}^-_{0,\omega}$	The frequency-domain and k-domain electric field of a wave propagating in the negative z-direction in the free space, Eq. (2.5).	
	$\widetilde{\mathbf{E}}^-_{0,\omega} = \hat{\mathbf{x}}\widetilde{E}^-_{0x,\omega} + \hat{\mathbf{y}}\widetilde{E}^-_{0y,\omega} + \hat{\mathbf{z}}\widetilde{E}^-_{0z,\omega}$	mVs
$\widetilde{\mathbf{E}}^\pm_{0,\omega}$	Either $\widetilde{\mathbf{E}}^+_{0,\omega}$ or $\widetilde{\mathbf{E}}^-_{0,\omega}$.	mVs
$\widetilde{\mathbf{E}}^+_{1,\omega}$	The frequency-domain and k-domain electric field of a wave propagating in the positive z-direction in the free space, Eq. (2.21).	
	$\widetilde{\mathbf{E}}^+_{1,\omega} = \hat{\mathbf{x}}\widetilde{E}^+_{1x,\omega} + \hat{\mathbf{y}}\widetilde{E}^+_{1y,\omega} + \hat{\mathbf{z}}\widetilde{E}^+_{1z,\omega}$	mVs
$\widetilde{\mathbf{E}}^-_{1,\omega}$	The frequency-domain and k-domain electric field of a wave propagating in the negative z-direction in the free space, Eq. (2.21).	
	$\widetilde{\mathbf{E}}^-_{1,\omega} = \hat{\mathbf{x}}\widetilde{E}^-_{1x,\omega} + \hat{\mathbf{y}}\widetilde{E}^-_{1y,\omega} + \hat{\mathbf{z}}\widetilde{E}^-_{1z,\omega}$	mVs
$\widetilde{\mathbf{E}}^\pm_{1,\omega}$	Either $\widetilde{\mathbf{E}}^+_{1,\omega}$ or $\widetilde{\mathbf{E}}^-_{1,\omega}$.	mVs
f	Frequency	Hz
f_{max}	Maximum frequency for image reconstruction, Eq. (5.22).	Hz
f_{ST}	Frequency, p. 28.	Hz
$\overline{\mathbf{F}}_\omega$	Dyad, Eq. (3.25).	m
$\mathbf{H}^+_{0,t}$	The time-domain magnetic field of a wave propagating in the positive z-direction in the free space.	
	$\mathbf{H}^+_{0,t} = \hat{\mathbf{x}}H^+_{0x,t} + \hat{\mathbf{y}}H^+_{0y,t} + \hat{\mathbf{z}}H^+_{0z,t}$	Am^{-1}
$\mathbf{H}^-_{0,t}$	The time-domain magnetic field of a wave propagating in the negative z-direction in the free space.	
	$\mathbf{H}^-_{0,t} = \hat{\mathbf{x}}H^-_{0x,t} + \hat{\mathbf{y}}H^+_{0y,t} + \hat{\mathbf{z}}H^-_{0z,t}$	Am^{-1}
$\mathbf{H}^+_{1,t}$	The time-domain magnetic field of a wave propagating in the positive z-direction in the soil.	
	$\mathbf{H}^+_{1,t} = \hat{\mathbf{x}}H^+_{1x,t} + \hat{\mathbf{y}}H^+_{1y,t} + \hat{\mathbf{z}}H^+_{1z,t}$	Am^{-1}

$\mathbf{H}^-_{1,t}$	The time-domain magnetic field of a wave propagating in the negative z-direction in the soil, Eq. (2.49). $\mathbf{H}^-_{1,t} = \hat{\mathbf{x}}H^-_{1x,t} + \hat{\mathbf{y}}H^+_{1y,t} + \hat{\mathbf{z}}H^-_{1z,t}$	Am^{-1}
$\mathbf{H}^+_{0,\omega}$	The frequency-domain magnetic field of a wave propagating in the positive z-direction in the free space. $\mathbf{H}^+_{0,\omega} = \hat{\mathbf{x}}H^+_{0x,\omega} + \hat{\mathbf{y}}H^+_{0y,\omega} + \hat{\mathbf{z}}H^+_{0z,\omega}$	Asm^{-1}
$\mathbf{H}^-_{0,\omega}$	The frequency-domain magnetic field of a wave propagating in the negative z-direction in the free space. $\mathbf{H}^-_{0,\omega} = \hat{\mathbf{x}}H^-_{0x,\omega} + \hat{\mathbf{y}}H^-_{0y,\omega} + \hat{\mathbf{z}}H^-_{0z,\omega}$	Asm^{-1}
$\mathbf{H}^+_{1,\omega}$	The frequency-domain magnetic field of a wave propagating in the positive z-direction in the soil. $\mathbf{H}^+_{1,\omega} = \hat{\mathbf{x}}H^+_{1x,\omega} + \hat{\mathbf{y}}H^+_{1y,\omega} + \hat{\mathbf{z}}H^+_{1z,\omega}$.	Asm^{-1}
$\mathbf{E}^-_{1,\omega}$	The frequency-domain magnetic field of a wave propagating in the negative z-direction in the soil. $\mathbf{H}^-_{1,\omega} = \hat{\mathbf{x}}H^-_{1x,\omega} + \hat{\mathbf{y}}H^-_{1y,\omega} + \hat{\mathbf{z}}H^-_{1z,\omega}$	Asm^{-1}
$\widetilde{\mathbf{H}}^+_{1,\omega}$	Plane-wave spectrum of the frequency-domain magnetic field of a wave propagating in the positive z-direction in the soil. $\widetilde{\mathbf{H}}^+_{1,\omega} = \hat{\mathbf{x}}\widetilde{H}^+_{1x,\omega} + \hat{\mathbf{y}}\widetilde{H}^+_{1y,\omega} + \hat{\mathbf{z}}\widetilde{H}^+_{1z,\omega}$	Asm
$\widetilde{\mathbf{H}}^-_{1,\omega}$	Plane-wave spectrum of the frequency-domain magnetic field of a wave propagating in the negative z-direction in the soil. $\widetilde{\mathbf{H}}^-_{1,\omega} = \hat{\mathbf{x}}\widetilde{H}^-_{1x,\omega} + \hat{\mathbf{y}}\widetilde{H}^-_{1y,\omega} + \hat{\mathbf{z}}\widetilde{H}^-_{1z,\omega}$	Asm
$I_{A,t}$	Total current at the reference plane, Eq. (2.50).	A
$I_{21,\omega}$	Function, Eq. (5.10).	m
$I_{A21,\omega}$	Function, Eq. (5.12).	
$I_{A11,\omega}$	Function, Eq. (5.20).	
$\mathbf{J}_{nP,\omega}$	Current distribution on the probe n, $n = 1, 2$, p. 17.	Asm^{-1}
$\mathbf{J}_{ST,\omega_{ST}}$	Current distribution, p. 28.	Asm^{-1}
$\mathbf{J}_{MoM,\omega}$	Current distribution used in the MoM model, Eq. (3.12).	Asm^{-1}
$\mathbf{J}_{MoMA,\omega}$	Current distribution used in the MoM model, Eq. (3.17).	Asm^{-1}
$\mathbf{J}_{MoMB,\omega}$	Current distribution used in the MoM model, Eq. (3.18).	Asm^{-1}
$k_{0,\omega}$	Wavenumber in the free space, $k_{0,\omega} = \omega\sqrt{\mu_0\varepsilon_0}$, p. 6.	m^{-1}
$k_{1,\omega}$	Wavenumber in the soil, $k_{1,\omega} = \omega\sqrt{\mu_0\varepsilon_{1,\omega}}$, p. 11.	m^{-1}
$k^r_{1,\omega}$	Real wavenumber, $k^r_{1,\omega} = \omega\sqrt{\mu_0\varepsilon'_{1,\omega}}$, p. 64.	m^{-1}
K_0	Constant, Eq. (4.2).	
$\mathbf{k}^{\pm}_{0,\omega}$	Propagation vector in free space, $\mathbf{k}^{\pm}_{0,\omega}(k_x, k_y) = \hat{\mathbf{x}}k_x + \hat{\mathbf{y}}k_y \pm \hat{\mathbf{z}}\gamma_{0,\omega}(k_x, k_y)$.	m^{-1}
$\mathbf{k}^{\pm}_{1,\omega}$	Propagation vector in soil, $\mathbf{k}^{\pm}_{1,\omega}(k_x, k_y) = \hat{\mathbf{x}}k_x + \hat{\mathbf{y}}k_y \pm \hat{\mathbf{z}}\gamma_{1,\omega}(k_x, k_y)$.	m^{-1}
k_x	The angular spatial frequencies in the x-direction, p. 8.	m^{-1}
k_y	The angular spatial frequencies in the y-direction, p. 8.	m^{-1}
k_{xy}	$k_{xy} = \sqrt{k_x^2 + k_y^2}$.	m^{-1}

$\mathbf{l}_{A0,\omega}$	The vector effective length of an antenna, Eq. (2.15).	m
l_c	Length of cable, p. 27.	m
$P_{S,\omega}$	The power transmitted through the air-soil interface, Eq. (2.34).	Js
P_S	Total transmitted power in the soil, Eq. (2.49).	J
$P_{Sx,\omega}$	Partial power transmitted through the air-soil interface, Eq. (2.38).	Js
$P_{Sy,\omega}$	Partial power transmitted through the air-soil interface, p. 15.	Js
$P_{Srhcp,\omega}$	Partial power transmitted through the air-soil interface, Eq. (2.45).	VAs^2
$P_{Slhcp,\omega}$	Partial power transmitted through the air-soil interface, p. 16.	VAs^2
$P_{A,\omega}$	Power accepted by the antenna, Eq. (2.36).	VAs^2
P_A	Total power accepted by the antenna, Eq. (2.50).	J
q_P	Constant, Eq. (3.10).	
q	Constant, Eq. (3.46).	
$\mathbf{r}$	Position in space, $\mathbf{r} = \hat{\mathbf{x}}x + \hat{\mathbf{y}}y + \hat{\mathbf{z}}z$.	m
$\mathbf{r}_A$	Position of antenna, $\mathbf{r}_A = \hat{\mathbf{x}}x_A + \hat{\mathbf{y}}y_A$, p. 6.	m
$\mathbf{R}_{A0,\omega}$	Plane-wave receiving spectrum in free space, $\mathbf{R}_{A0,\omega} = R_{A0x,\omega}\hat{\mathbf{x}} + R_{A0y,\omega}\hat{\mathbf{y}} + R_{A0z,\omega}\hat{\mathbf{z}}$, Eq. (2.13).	m
$\mathbf{R}_{A1,\omega}$	Plane-wave receiving spectrum for a GPR antenna, $\mathbf{R}_{A1,\omega} = R_{A1x,\omega}\hat{\mathbf{x}} + R_{A1y,\omega}\hat{\mathbf{y}} + R_{A1z,\omega}\hat{\mathbf{z}}$, Eq. 2.28.	m
$\mathbf{R}_{nP,\omega}$	Plane-wave receiving spectrum for probe n, $n = 1, 2$, $\mathbf{R}_{nP,\omega} = R_{nPx,\omega}\hat{\mathbf{x}} + R_{nPy,\omega}\hat{\mathbf{y}} + R_{nPz,\omega}\hat{\mathbf{z}}$, p. (2.52).	m
$\overline{\mathbf{S}}_{A0,\omega}$	Scattering dyadic, p. 9.	m^2
t	Time.	s
$S_{A11,\omega}$	Reflection coefficient of GPR antenna 1, Eq. (5.1).	
$S_{A22,\omega}$	Reflection coefficient of GPR antenna 2, Eq. (5.1).	
$S_{A21,\omega}$	Transfer function between GPR antenna 1 and 2, Eq. (5.1).	
$S_{A12,\omega}$	Transfer function between GPR antenna 2 and 1, Eq. (5.1).	
S_{11}	Voltage transfer function, p. 45.	
$S_{12,\omega}$	Voltage transfer function, p. 27.	
$S_{21,\omega}$	Voltage transfer function, p. 27.	
$S_{nPA,\omega}$	Voltage transfer function between the GPR antenna under test and the probe, Eq. (2.53).	
$S_{nAP,\omega}$	Voltage transfer function between the GPR antenna under test and the probe, Eq. (2.54).	
$S_{AA,\omega}$	Reflection coefficient, p. 65.	
$S_{EE,\omega}$	Reflection coefficient in the excitation cut, Eq. (3.3).	
$S_{F11,\omega}$	Reflection coefficient of GPR antenna 1 due to objects in the soil, Eq. (5.3).	
$\widetilde{S}_{F11,\omega}$	Fourier-transformed reflection coefficient of GPR antenna 1 due to objects in the soil, Eq. (5.6).	m^2
$S_{F21,\omega}$	Transfer function between GPR antenna 1 and 2 due to objects in the soil, Eq. (5.4).	
$\widetilde{S}_{F21,\omega}$	Fourier-transformed transfer function between GPR antenna 1 and 2 due to objects in the soil, Eq. (5.7).	m^2
$S_{PP,\omega}$	Reflection coefficient, Eq. (3.2).	

$\widetilde{S}_{nPA,\omega}$	Fourier-transformed voltage transfer function $S_{nPA,\omega}$, Eq. (2.57).	m^2
T	Temperature.	^oC
$\mathbf{T}_{A0,\omega}$	Plane-wave transmitting spectrum in free space, $\mathbf{T}_{A0,\omega} = T_{A0x,\omega}\hat{\mathbf{x}} + T_{A0y,\omega}\hat{\mathbf{y}} + T_{A0z,\omega}\hat{\mathbf{z}}$, Eq. (2.5).	m
$\mathbf{T}_{A1,\omega}$	Plane-wave transmitting spectrum in the soil, $\mathbf{T}_{A1,\omega} = T_{A1x,\omega}\hat{\mathbf{x}} + T_{A1y,\omega}\hat{\mathbf{y}} + T_{A1z,\omega}\hat{\mathbf{z}}$, Eq. (2.26).	m
$V^+_{1,\omega}$	Voltage in reference plane, p. 27.	Vs
$V^-_{1,\omega}$	Voltage in reference plane, p. 27.	Vs
$V^+_{2,\omega}$	Voltage in reference plane, p. 27.	Vs
$V^-_{2,\omega}$	Voltage in reference plane, p. 27.	Vs
$V_{A,\omega}$	Total voltage of the waves in the reference plane of the antenna, p. 6.	Vs
$V^+_{A,\omega}$	Voltage of the incoming wave in the reference plane of the antenna, p. 6.	Vs
$V_{A,\omega}$	Voltage of the outgoing wave in the reference plane of the antenna, p. 6.	Vs
$V^+_{A1,\omega}$	Voltage of the incoming wave in the reference plane of the GPR antenna 1, p. 76.	Vs
$V^-_{A1,\omega}$	Voltage of the outgoing wave in the reference plane of the GPR antenna 1, p. 76.	Vs
$V^+_{A2,\omega}$	Voltage of the incoming wave in the reference plane of the GPR antenna 2, p. 76.	Vs
$V^-_{A2,\omega}$	Voltage of the outgoing wave in the reference plane of the GPR antenna 2, p. 76.	Vs
$V_{nP,\omega}$	Total voltage of the waves in the reference plane of the probe n, $n = 1, 2$, p. 17.	Vs
$V^+_{nP,\omega}$	Voltage of the incoming wave in the reference plane of the probe n, $n = 1, 2$, p. 17.	Vs
$V_{nP,\omega}$	Voltage of the outgoing wave in the reference plane of the probe n, $n = 1, 2$, p. 17.	Vs
$V_{Aoc,\omega}$	The open circuit voltage of an antenna, p. 9.	Vs
$V_{A,t}$	Total voltage at the reference plane, Eq. (2.50).	V
$V_{Cut,\omega}$	Total voltage in the excitation cut of the loop antenna, p. 28.	Vs
$V^+_{E,\omega}$	Voltage of the incoming wave in the reference plane at the excitation cut, Eq. (3.3).	Vs
$V^-_{E,\omega}$	Voltage of the outgoing wave in the reference plane at the excitation cut, Eq. (3.3).	Vs
$V_{MoM,\omega}$	Impressed voltage in the MoM model, Eq. (3.14).	Vs
$V_{MoMA,\omega}$	Impressed voltage in the MoM model, Eq. (3.17).	Vs
$V_{MoMB,\omega}$	Impressed voltage in the MoM model, Eq. (3.18).	Vs
$V^+_{P,\omega}$	Voltage of the incoming wave in the reference plane at the excitation cut, Eq. (3.2).	Vs
$V^-_{P,\omega}$	Voltage of the outgoing wave in the reference plane at the excitation cut, Eq. (3.2).	Vs

$V_{ST,\omega_{ST}}$	Impressed voltage, p. 28.	Vs
V_{total}	Total volume of soil, Eq. (3.31).	m^3
V_a	Volume of air in soil with a total volume V_{total}, Eq. (3.31).	m^3
V_p	Volume of soil particle in soil with a total volume V_{total}, Eq. (3.31).	m^3
V_b	Volume of bounded water in soil with a total volume V_{total}, Eq. (3.31).	m^3
V_u	Volume of unbounded water in soil with a total volume V_{total}, Eq. (3.31)	m^3
W	Volumetric fraction of water in soil, Eq. (3.36).	
W_t	Maximum volumetric fraction of bounded water, Eq. (3.37).	
W_n	Volumetric fraction of component n in soil, Eq. (3.30).	
W_a	Volumetric fraction of air in soil, Eq. (3.32).	
W_p	Volumetric fraction of soil particles in soil, Eq. (3.33).	
W_b	Volumetric fraction of bounded water in soil, Eq. (3.34).	
W_u	Volumetric fraction of unbounded water in soil, Eq. (3.34).	
W_F	Window function, Eq. (4.3).	
W_{xy}	Window function, Eq. (5.26).	
W_x	Cosine roll-off window function, Eq. (5.26).	
W_y	Cosine roll-off window function, Eq. (5.26).	
x	Horizontal position.	m
$\mathbf{x}$	Vector, p. 75.	
(x_m, y_m)	Measurement coordinate system, p. 58.	m
(x_c, y_c)	Common measurement system, p. 58.	m
x_A	Horizontal position of antenna, p. 6.	m
$x_{A,min}$	Minimum of x_A in scan for image reconstruction, Eq. (5.27).	m
$x_{A,max}$	Maximum of x_A in scan for image reconstruction, Eq. (5.27).	m
y	Horizontal position.	m
y_A	Horizontal position of antenna, p. 6.	m
$y_{A,min}$	Minimum of y_A in scan for image reconstruction, Eq. (5.28).	m
$y_{A,max}$	Maximum of y_A in scan for image reconstruction, Eq. (5.28).	m
Y_c	Characteristic admittance of the cable, p. 6	S
$Y_{Cut,\omega}$	Admittance of the loop antenna in the excitation cut, p. 28.	S
$Y^I_{Cut,\omega}$	Admittance of the loop antenna in the excitation cut, p. 31.	S
$Y^{II}_{Cut,\omega}$	Admittance of the loop antenna in the excitation cut, p. 31.	S
$Y_{A0,\omega}$	Admittance of an antenna, p. 9.	S
$Y_{MoM,\omega}$	Admittance of an antenna in the MoM model, Eq. (3.15).	S
$Y_{ST,\omega_{ST}}$	Admittance of an antenna, p. 28.	S
z	Horizontal position.	m
z_G	Constant, p. 6.	m

List of Acronyms

Acronym	Decription
ACE	Antenna Centre of Excellence.
AUT	Antenna under test.
CMP	Common midpoint.
EMC	Electromagnetic compatibility.
GPR	Ground penetrating radar.
GUI	Graphical user interface.
HP	Hewlett-Pachard.
IF	Intermediate frequency.
MoM	Method of moment.
PEC	Perfect electric conducting.
PTFE	Polytetrafluoroethylene.
PWRS	Plane-wave receiving spectrum.
PWTS	Plane-wave transmitting spectrum.
SPCW	Silver plated cobber wire.
TEM	Tranverse electromagnetic.

Contents

Chapter 1

Introduction

Image reconstruction of subsurface layers and objects using GPR systems is used in many applications ranging from road survey, detection of cables and pipes, geological research and archaeological research, etc. [1]. Road survey using GPR systems provides a fast and inexpensive method for mapping of asphalt thickness using vehicle-mounted systems as suggested by Eide and Hjelmstad in [2] and Jung et al. in [3]. The use of GPR systems for geological research has increased in recent years. Bristow reports that processing and interpretation of data for stratigraphic studies are improved by tests of radar performance in [4]. The suitability of GPR systems are often limited by the conductivity of the soil. Even dry soil can be highly conductive and consequently have a poor suitability [5]. In recent years tests of GPR systems for archaeological research have been performed. Conyers has tested the usability of GPR systems for archaeological research at test sites with different soil types and moisture content [6]. It is reported that the moisture content is the dominant factor influencing the complex permittivity of the soil and the scattering from objects in the soil. The influence of the moisture content on the complex permittivity is described by Mironov in [7]. Mironov suggests a model of the complex permittivity of the soil which is experimentally verified. This model predicts that both the velocity of propagation and the losses are highly dependent on the moisture content. The losses due to moisture are described using the Debye model that predicts losses that increase rapidly with the frequency. Therefore, low frequencies yield a better penetration through the soil. Traditional radar theory predicts that the minimum detectable distance between two objects is inversely proportional to the frequency bandwidth used [8]. The resolution is referred to as high if the minimum detectable distance is small. The frequency-dependent losses due to soil moisture as described by Mironov can limit the usable frequency bandwidth, and hence it follows that the obtainable resolution can be limited. A poor resolution and a more inhomogeneous environment due to fluctuations in the soil moisture content can mask the objects in the soil. Therefore, research in super-resolution methods is ongoing [9]. A number of non-invasive methods for the estimation of the complex permittivity of the soil have been developed. The common

midpoint (CMP) data acquisition method as suggested by Sato et al. in [10] is based on transmission measurements between antennas. Measured impedances of a dipole antenna located at an air-soil interface can be used for estimation of the complex permittivity as suggested by Wakita in [11].

Since high resolution can be obtained using a wide band of frequencies it is desirable to develop broadband GPR antennas. A number of GPR antennas consist of modifications of classical ultrawideband antennas, as described in [12]. The bowtie antenna is a classical antenna that is used in a number of GPR antenna designs. Resistively loaded bowtie antennas can be used in a vehicle mounted array as suggested by Eide in [13] and [14]. A number of different designs using bowtie antennas are proposed by Lestari et al. in [15] and [16]. Further, non-dispersive linearly polarized antennas like the dielectric filled TEM horn and the dielectric embedded shielded dipole are treated by Yarovoy and Ligthart in [17]. Dispersive broadband antennas like the equiangular planar spiral antenna are used in design of GPR antennas as discussed by Daniels in [1, pp. 155-156] and Thaysen in [18]. However, it is necessary to take into account the dispersive behavior of this antenna.

To compare the broadband properties of GPR antennas it is desirable to develop measurements for GPR antennas. The loop antenna is reported to be a usable for wideband measurements of GPR antennas by Yarovoy et al. in [19]. Time-domain measurement procedure using the loop antenna buried in dry soil is presented by Jongh et al. in [20]. The electromagnetic field radiated by the GPR antenna under test is measured as peak values of the transmit waveform within a horizontal plane.

The radiated electromagnetic field by antennas in free space can be written as an expansion of plane waves as suggested by Kerns in [21]. This plane-wave expansion can also be used for electromagnetic wave in soil radiated by GPR antennas. Based on this plane-wave expansion, a measurement procedure using a step-frequency system is suggested by Meincke and Hansen in [22]. In this procedure the GPR antenna is characterized using a plane-wave spectrum that describes the spatial response of the GPR antenna.

Several methods for imaging have been developed based on scalar models of seismic wave propagation [23]. Further methods are based on a vectorial description of the electromagnetic field as suggested by Meincke and Hansen in [24] where the GPR antennas are modelled as Hertzian dipoles close to the air-soil interface. This model can be used for a number of non-dispersive and linearly polarized GPR antennas. However, for broadband dispersive antennas a better model is desirable. If the plane-wave transmitting spectrum is measured, then this spectrum can be used in an imaging procedure as suggested by Meincke in [25]. From a theoretical point of view dispersive broadband GPR antennas are usable by use of the plane-wave transmitting spectrum.

Chapter 2 is an introduction to classical plane-wave theory as described by Hansen and Yaghjian in [26]. Plane-wave theory is used for an accurate description of the electromagnetic field in the soil radiated by GPR antennas and development of a measurement procedure as suggested by Meincke and Hansen in [22]. A method for the calculation of the plane-wave transmitting spectrum is presented, and the stability of

the matrix equation is investigated as suggested by Kerns in [21]. Antenna parameters defined by Lenler-Eriksen and Meincke in [27] are presented.

In Chapter 3 the loop antenna for measurement of the GPR antennas is presented [19]. The loop antenna is characterized by the plane-wave receiving spectrum that is calculated using a method of moment program as suggested by Jørgensen in [28]. To calculate the plane-wave receiving spectrum, information about the constitutive parameters of the soil is necessary. A method for estimation of the complex permittivity based on measurements of the admittance of the loop antenna buried in dry loam can be performed as suggested by Lenler-Eriksen and Meincke in [29] and [30]. Another method based on transmission measurements between loop antennas is used for estimation of the complex permittivity of moist loam. The estimated complex permittivities are compared with measurements of the complex permittivity for similar types of soil as presented by Mironov in [7].

In Chapter 4 the Joint ACE ground penetrating radar antenna test facility at the Technical University of Denmark is presented. This measurement facility can be used for comparison of GPR antennas using the measured transfer functions between the loop antenna buried in the soil and the GPR antenna above the air-soil interface as described by Lenler-Eriksen et al. in [31]. Measurements of the plane-wave transmitting spectra of GPR antennas can also be performed as suggested by Lenler-Eriksen and Meincke in [32] and [33]. In this thesis, measurements of a bowtie antenna design by Eide in [13] and an equiangular planar spiral antenna are presented. The plane-wave transmitting spectra are measured for these two antennas in preparation for the imaging procedures presented in Chapter 5.

In Chapter 5 the Fourier method for inversion of scattering data from GPR systems is presented as suggested by Meincke in [25]. Using this method it is expected that an inversion can be performed for GPR systems with dispersive antennas. Therefore, this method is tested on synthetic data for a GPR system with a dispersive and circularly polarized equiangular planar spiral antenna in [34]. To test the usability of the Fourier method for image reconstruction using measured scattering data, the measured plane-wave transmitting spectrum for an equiangular planar spiral antenna is used for image reconstruction. Image reconstruction is also performed using the measured plane-wave spectrum for a bowtie antenna. This image is compared with constructed image using a simple Hertzian dipole model for the bowtie antenna [24].

The difference between the phasor and frequency-domain formulations is explained by Appel-Hansen in [35, pp. 1.5-1.8]. In this thesis, the frequency-domain formulation is used as defined in Appendix A.2.

Chapter 2

Plane-Wave Theory with Application to GPR Antenna Characterization

Plane-wave theory for measurements of antennas in free space was first introduced by Kerns in 1963 [36]. Kerns suggests a procedure in which the electromagnetic field is measured on a planar scan plane in the near-field region of the antenna under test (AUT). Using an appropriate set of probes, this technique gives a complete knowledge about the radiated field from the AUT in both the near-field region and the far-field region. Furthermore, Kerns developed explicit expressions of the radiated field in terms of plane-wave expansions [21], [37]. In these expressions probe correction is performed using knowledge about the transmitting or receiving characteristics of the probe. Phasor-domain formulation is used, and all expressions can be implemented in a straightforward manner if the measurements are done using a step-frequency system.

Similar expressions based on plane-wave expansions in the time-domain were suggested by Hansen and Yaghjian in 1995 [38]. These expressions are straightforward to implement if time-domain measurements are performed [26].

Other expansions, like those based on spherical and cylindrical waves, can also be used. If multiple interactions between the AUT and the probe are negligible then these expansions will give exact expressions of the radiated field in both the near-field and far-field regions. The measurement configuration influences the choice of the expansion as suggested in [39], [40]. An expansion in spherical waves is convenient if the measurements of the electromagnetic field is performed on a spherical surface. Similarly, an expansion in cylindrical waves is convenient if the measurements are performed on a cylindrical surface. In this thesis, measurements of GPR antennas on a planar surface are considered and plane-wave expansions of the field are therefore used.

Plane-wave theory is suitable to use for description of fields in any linear, homo-

geneous, and isotropic medium. Based on this fact, a measurement procedure and a plane-wave characterization of GPR antennas are suggested by Meincke and Hansen in [22].

So far only few measurement facilities for GPR antennas have been constructed. Indoor time-domain measurement facilities have been constructed at the Technical University of Delft. These facilities have been described in a number of papers [41], [20], [42]. In the description of the experimental set-up for measurement of GPR antennas it has been reported by Jongth et al [20] that two field components of the electromagnetic field have been determined just beneath the air-soil interface. However, the method for calculation of these field components has not been revealed. So far, no results have been published in the literature on practical measurements of GPR antennas using plane-wave theory.

This chapter gives an introduction to the plane-wave characterization of GPR antennas and it is organized as follows: In Section 2.1, the plane-wave expansion of the electric field in the soil radiated from a GPR antenna is presented. This section is based on results from [22]. In Section 2.2, antenna parameters are defined based on plane-wave expansions. In Section 2.3, a method for estimation of the plane-wave transmitting spectrum is suggested.

2.1 Model for the Transmitting and Receiving GPR Antenna

This section presents an introduction to plane-wave characterization of GPR antennas, as suggested by Meincke and Hansen in [22]. In Section 2.1.1, the plane-wave characterization for an antenna radiating in the free space is introduced. In Section 2.1.2, this is extended to the case of a GPR antenna radiating into soil.

2.1.1 Plane-Wave Characterization of Antennas in Free Space

An antenna in free space is considered, and the usual rectangular xyz-coordinate system, shown on the left in Figure 2.1, is used. All radiating parts of the antenna are localized in the region $z > z_G$ and the electromagnetic field is considered in the region $z < z_G$. The air has the free-space permeability μ_0 and free-space permittivity ϵ_0. The wavenumber of air is $k_{0,\omega} = \omega\sqrt{\mu_0\varepsilon_0}$ and the wavelength is $\lambda_{0,\omega} = 2\pi/k_{0,\omega}$. The reference point of the antenna is chosen as $\mathbf{r}_A = \hat{\mathbf{x}}x_A + \hat{\mathbf{y}}y_A$.

The antenna is fed through a transmission line which is assumed to be a coaxial cable. The coaxial cable is supporting a single TEM mode and the characteristic admittance of the cable is denoted by Y_c . A reference plane is chosen in the coaxial cable, and the voltages of the incoming and outgoing wave in the reference plane are denoted by $V^+_{A,\omega}$ and $V^-_{A,\omega}$, respectively. The total voltage $V_{A,\omega}$ at the reference plane is denoted by $V_{A,\omega} = V^+_{A,\omega} + V^-_{A,\omega}$.

On the right in Figure 2.1 the cross section of the coaxial cable is described using the usual rectangular $x'y'z'$-coordinate system with the associate cylindrical $\rho'\phi'z'$-

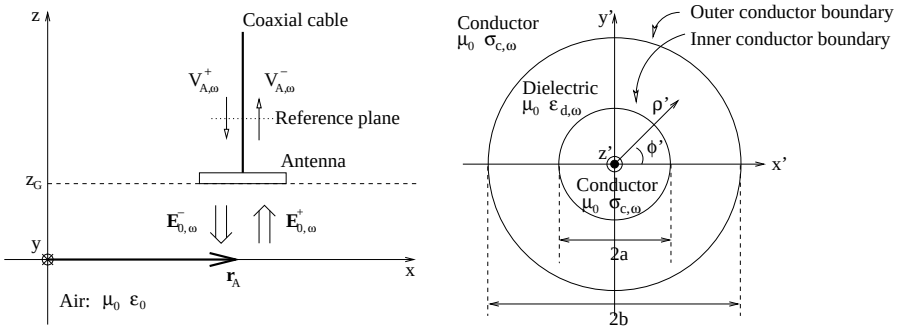

Figure 2.1: **Left:** The configuration for definition of the plane-wave spectrum in free space. All radiating parts are localized in the half-space $z > z_A$. **Right:** Cross section of the coaxial cable. The antenna is in direction of $+\hat{\mathbf{z}}'$.

system. The boundary of the center conductor is given by $\rho' = a$ and the boundary of the outer conductor is given by $\rho' = b$. The conductors have the free-space permeability μ_0 and the complex permittivity $\varepsilon_{c,\omega} = \varepsilon'_{c,\omega} + i\varepsilon''_{c,\omega}$ where $\varepsilon'_{c,\omega}$ and $\varepsilon''_{c,\omega}$ are real quantities. The imaginary part $\varepsilon''_{c,\omega}$ of the complex permittivity is written in terms of a conductivity $\sigma_{c,\omega}$ as $\varepsilon''_{c,\omega} = \sigma_{c,\omega}/\omega$. Good conductors are considered so that the loss tangent $\tan\delta_{c,\omega}$ defined as

$$\tan\delta_{c,\omega} = \frac{\sigma_{c,\omega}}{\omega\varepsilon'_{c,\omega}}, \tag{2.1}$$

is large compared to unity, that is $\tan\delta_{c,\omega} \gg 1$. The dielectric between the center conductor and the outer conductor has the free space permeability μ_0 and the complex permittivity $\varepsilon_{d,\omega} = \varepsilon'_{d,\omega} + i\varepsilon''_{d,\omega}$. Low loss dielectrics are considered so that the loss tangent $\tan\delta_{d,\omega}$ defined as

$$\tan\delta_{d,\omega} = \frac{\varepsilon''_{c,\omega}}{\varepsilon'_{c,\omega}}, \tag{2.2}$$

is small compared to unity, that is $\tan\delta_{d,\omega} \ll 1$. The total voltage is related to the electric field $\mathbf{E}_{d,\omega}$ in the dielectric of the coaxial cable through the relations

$$\mathbf{E}_{d,\omega}(\rho) = \frac{V_{A,\omega}\hat{\rho}}{\rho \ln\left(\frac{b}{a}\right)}, \quad a < \rho < b. \tag{2.3}$$

In the region $z < z_G$ below the radiating parts the total electric field $\mathbf{E}_{0,\omega} = E_{0x,\omega}\hat{\mathbf{x}} + E_{0y,\omega}\hat{\mathbf{y}} + E_{0z,\omega}\hat{\mathbf{z}}$ can be written as a superposition of the electric field $\mathbf{E}^+_{0,\omega}$ for an upward propagating wave and the electric field $\mathbf{E}^-_{0,\omega}$ for a downward propagating wave

$$\mathbf{E}_{0,\omega}(\mathbf{r}) = \mathbf{E}^+_{0,\omega}(\mathbf{r}) + \mathbf{E}^-_{0,\omega}(\mathbf{r}), \quad z < z_G, \tag{2.4}$$

where an arbitrary position $\mathbf{r} = \hat{\mathbf{x}}x + \hat{\mathbf{y}}y + \hat{\mathbf{z}}z$ is considered for $z < z_G$. The electric fields $\mathbf{E}^{+}_{0,\omega}$ and $\mathbf{E}^{-}_{0,\omega}$ are written in terms of an expansion of plane waves as

$$\mathbf{E}^{\pm}_{0,\omega}(\mathbf{r}) = \frac{1}{(2\pi)^2}\iint_{-\infty}^{\infty} \widetilde{\mathbf{E}}^{\pm}_{0,\omega}(k_x,k_y)e^{i[\mathbf{k}^{\pm}_{0,\omega}(k_x,k_y)\cdot\mathbf{r}]}dk_xdk_y, \quad z < z_G, \tag{2.5}$$

where the quantities k_x and k_y are denoted by the spatial frequencies. In this expansion the electric field is written as an expansion of plane waves with the propagating vectors

$$\mathbf{k}^{\pm}_{0,\omega}(k_x,k_y) = \hat{\mathbf{x}}k_x + \hat{\mathbf{y}}k_y \pm \hat{\mathbf{z}}\gamma_{0,\omega}(k_x,k_y), \tag{2.6}$$

where $\gamma_{0,\omega}$ is defined as

$$\gamma_{0,\omega}(k_x,k_y) = \begin{cases} \sqrt{k_{0,\omega}^2 - k_x^2 - k_y^2}, & \omega \geq 0, \\ -(\gamma_{0,-\omega}(k_x,k_y))^*, & \omega < 0, \end{cases} \tag{2.7}$$

and the asterisk $*$ denotes complex conjugation. The branch of the square root is chosen so that the imaginary part of $\gamma_{0,\omega}$ is nonnegative. The quantity $\widetilde{\mathbf{E}}^{\pm}_{0,\omega}$ is denoted by the electric plane-wave spectrum. The electric plane-wave spectrum is given by the two-dimensional Fourier transform

$$\widetilde{\mathbf{E}}^{\pm}_{0,\omega}(k_x,k_y) = \iint_{-\infty}^{\infty} \mathbf{E}^{\pm}_{0,\omega}(\mathbf{r})e^{-i[\mathbf{k}^{\pm}_{0,\omega}(k_x,k_y)\cdot\mathbf{r}]}dxdy, \quad z < z_G. \tag{2.8}$$

Due to the relation $\mathbf{k}^{\pm}_{0,\omega}(k_x,k_y)\cdot\widetilde{\mathbf{E}}^{\pm}_{0,\omega}(k_x,k_y) = 0$ a full description of the field for $z < z_G$ can be obtained from knowledge of two of the three field components.

Consider now one plane wave $\widetilde{\mathbf{E}}^{\pm}_{0,\omega}(k_x,k_y)e^{i[\mathbf{k}^{\pm}_{0,\omega}(k_x,k_y)\cdot\mathbf{r}]}$ in the expansion (2.5). If the spatial frequencies comply with the relation $k_{0,\omega}^2 > k_x^2 + k_y^2$ then the amplitude of the electric field of the plane wave is constant since $\gamma_{0,\omega}$ is a purely real quantity. Such waves are denoted by propagating waves. Only propagating waves influence the electric field in the far-field region. If the spatial frequencies comply with the relation $k_{0,\omega}^2 < k_x^2 + k_y^2$ then $\gamma_{0,\omega}$ is a purely imaginary quantity, and the amplitude of the electric field is exponentially decreasing in the z direction for upward propagating waves and exponentially increasing in the z direction for downward propagating waves. These waves are denoted by evanescent waves.

The plane-wave transmitting spectrum $\mathbf{T}_{A0,\omega} = T_{A0x,\omega}\hat{\mathbf{x}} + T_{A0y,\omega}\hat{\mathbf{y}} + T_{A0z,\omega}\hat{\mathbf{z}}$ (PWTS) is defined as

$$\widetilde{\mathbf{E}}^{-}_{0,\omega}(k_x,k_y) = V^{+}_{A,\omega}(\mathbf{r}_A)\mathbf{T}_{A0,\omega}(k_x,k_y)e^{-i[k_xx_A + k_yy_A]}, \quad z < z_G, \tag{2.9}$$

so that the radiated electric field can be expressed in terms of the plane-wave expansion as

$$\mathbf{E}^{-}_{0,\omega}(\mathbf{r}) = \frac{V^{+}_{A,\omega}(\mathbf{r}_A)}{(2\pi)^2}\iint_{-\infty}^{\infty} \mathbf{T}_{A0,\omega}(k_x,k_y)e^{i[\mathbf{k}^{\pm}_{0,\omega}(k_x,k_y)\cdot(\mathbf{r}-\mathbf{r}_A)]}dk_xdk_y, \quad z < z_G. \tag{2.10}$$

If an upward-propagating wave is present, the scattering from the antenna gives an additional contribution to the downward-propagating wave and the spectrum of the downward-propagating wave is rewritten as

$$\widetilde{\mathbf{E}}^{-}_{0,\omega}(k_x,k_y) = V^{+}_{A,\omega}(\mathbf{r}_A)\mathbf{T}_{A0,\omega}(k_x,k_y)e^{-i[k_x x_A + k_y y_A]} + \iint_{-\infty}^{\infty} \overline{\mathbf{S}}_{A0,\omega}(k_x,k_y,k'_x,k'_y)\cdot\widetilde{\mathbf{E}}^{+}_{0,\omega}(k'_x,k'_y) \cdot e^{i[(k'_x-k_x)x_A+(k'_y-k_y)y_A]}dk'_x dk'_y, z < z_G. \quad (2.11)$$

where $\overline{\mathbf{S}}_{A0,\omega}$ is the scattering dyadic of the antenna. Equation (2.11) expresses that each upward-propagating plane wave with the spatial frequencies k'_x and k'_y gives rise to a spectrum of scattered plane waves with the spatial frequencies k_x and k_y. The spectrum of the scattered wave is written in terms of an integral over the dot-product between the scattering dyadic, and the electric spectrum of the upward-propagating wave with respect to the spatial frequencies k'_x and k'_y.

The reflection coefficient $\Gamma_{A0,\omega}$ of the antenna is defined as

$$\Gamma_{A0,\omega} = \left.\frac{V^{-}_{A,\omega}}{V^{+}_{A,\omega}}\right|_{\mathbf{E}^{+}_{0,\omega}(\mathbf{r})=\mathbf{0}}, \quad (2.12)$$

so that the voltage $V^{-}_{A,\omega}$ of the outgoing wave due to the reflection of the incoming wave in the coaxial cable by the antenna is written as the product $V^{+}_{A,\omega}(\mathbf{r}_A)\Gamma_{A0,\omega}$. The plane-wave receiving spectrum $\mathbf{R}_{A0,\omega} = R_{A0x,\omega}\hat{\mathbf{x}} + R_{A0y,\omega}\hat{\mathbf{y}} + R_{A0z,\omega}\hat{\mathbf{z}}$ (PWRS) is used for description of the received electromagnetic field. The contribution from each upward-propagating plane wave to the voltage $V^{-}_{A,\omega}$ can be expressed in terms of the dot-product $\mathbf{R}_{A0,\omega}\cdot\widetilde{\mathbf{E}}^{+}_{0,\omega}$. Herein, the voltage $V^{-}_{A,\omega}$ can be written in terms of the PWRS as

$$V^{-}_{A,\omega}(\mathbf{r}_A) = V^{+}_{A,\omega}(\mathbf{r}_A)\Gamma_{A0,\omega} + \frac{1}{(2\pi)^2}\iint_{-\infty}^{\infty}\mathbf{R}_{A0,\omega}(k_x,k_y)\cdot\widetilde{\mathbf{E}}^{+}_{0,\omega}(k_x,k_y)e^{i[k_x x_A + k_y y_A]}dk_x dk_y. \quad (2.13)$$

In the work on wideband sensors written by Yarovoy et al. in [19], the sensitivity of an antenna is defined as PWRS for propagating plane waves.

The vector effective length of an antenna is defined by Balanis in [43, pp. 79-81] using the Thevenin equivalent circuit in Figure 2.2. The open circuit voltage $V_{Aoc,\omega}$ is written in terms of the voltage $V^{-}_{A,\omega}$ of the outgoing wave and the admittance $Y_{A0,\omega}$ of the antenna as

$$V_{Aco,\omega} = \frac{Y_c + Y_{A0,\omega}}{Y_{A0,\omega}}V^{-}_{A,\omega}, \quad (2.14)$$

and the vector effective length can be written in terms of the PWRS as

$$\mathbf{l}_{A0,\omega}(k_x,k_y) = \frac{Y_{A0,\omega}}{Y_c + Y_{A0,\omega}}\mathbf{R}_{A0,\omega}(k_x,k_y), \quad k^2_{0,\omega} > k^2_x + k^2_y. \quad (2.15)$$

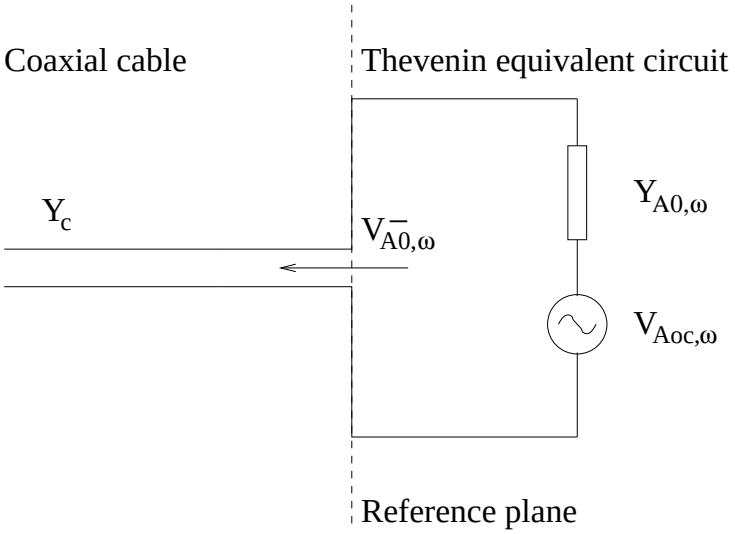

Figure 2.2: Thevenin equivalent circuit for the antenna with the admittance $Y_{A0,\omega}$ and the open circuit voltage $V_{0c,\omega}$.

The definition of the vector effective length of an antenna is therefore very similar to the definition of the plane-wave receiving spectrum.

Kerns shows in [21] that if the antenna consists of linear and isotropic materials, the reciprocity relation between the receiving and transmitting spectrum is given by

$$\mathbf{R}_{A0,\omega}(k_x, k_y) = \frac{\gamma_{0,\omega}(k_x, k_y)}{\omega\mu_0 Y_c}\mathbf{T}_{A0,\omega}(-k_x, -k_y). \tag{2.16}$$

Therefore, if the plane-wave transmitting spectrum is known, then the plane-wave receiving spectrum can be calculated, and vice versa. The reciprocity relation is used during the measurement procedure in Section 4.2 where the PWTS is calculated for the GPR antenna using a measurement configuration where the GPR antenna is receiving electromagnetic waves from loop antennas positioned in the soil.

The plane-wave theory for characterization of antennas in free space can also be used for characterization of antennas radiating an electromagnetic field in a linear, homogeneous and isotropic soil. This characterization is presented for a GPR antenna in the next section.

2.1.2 Plane-Wave Characterization of GPR Antennas close to an Air-Soil Interface

A configuration with a GPR antenna close to an air-soil interface is shown in Figure 2.3. The usual rectangular xyz-coordinate system is defined with the z-axis pointing into the upper half space and an air-soil interface is introduced at $z = 0$. The upper half space consists of air, and the lower half space consists of soil with the free space permeability μ_0 and permittivity $\varepsilon_{1,\omega} = \varepsilon'_{1,\omega} + i\varepsilon''_{1,\omega}$ where $\varepsilon'_{1,\omega}$ and $\varepsilon''_{1,\omega}$ are real quantities. The wavenumber of the soil is $k_{1,\omega} = \omega\sqrt{\mu_0\varepsilon_{1,\omega}}$ and the wavelength is

$$\lambda_{1,\omega} = \frac{2\pi}{\omega\sqrt{\mu_0\varepsilon'_{1,\omega}}}. \tag{2.17}$$

The voltages $V_{A,\omega}$, $V^-_{A,\omega}$, and $V^+_{A,\omega}$ in the reference plane of the coaxial cable are defined as in Section 2.1.1. The total electric field $\mathbf{E}_{0,\omega}$ in the air is written as

$$\mathbf{E}_{0,\omega}(\mathbf{r}) = \mathbf{E}^+_{0,\omega}(\mathbf{r}) + \mathbf{E}^-_{0,\omega}(\mathbf{r}), 0 < z < z_G. \tag{2.18}$$

Similarly, the total electric field in the soil, $\mathbf{E}_{1,\omega} = E_{1x,\omega}\hat{\mathbf{x}} + E_{1y,\omega}\hat{\mathbf{y}} + E_{1z,\omega}\hat{\mathbf{z}}$, is written as a superposition of an upward $\mathbf{E}^+_{1,\omega}$ and downward $\mathbf{E}^-_{1,\omega}$ propagating wave

$$\mathbf{E}_{1,\omega}(\mathbf{r}) = \mathbf{E}^+_{1,\omega}(\mathbf{r}) + \mathbf{E}^-_{1,\omega}(\mathbf{r}), z < 0. \tag{2.19}$$

The field $\mathbf{E}^\pm_{0,\omega}$ in the air is written in terms of a plane-wave expansion as

$$\mathbf{E}^\pm_{0,\omega}(\mathbf{r}) = \frac{1}{(2\pi)^2}\iint_{-\infty}^{\infty} \widetilde{\mathbf{E}}^\pm_{0,\omega}(k_x, k_y) e^{i[\mathbf{k}^\pm_{0,\omega}(k_x,k_y)\cdot\mathbf{r}]} dk_x dk_y, \quad 0 < z < z_G, \tag{2.20}$$

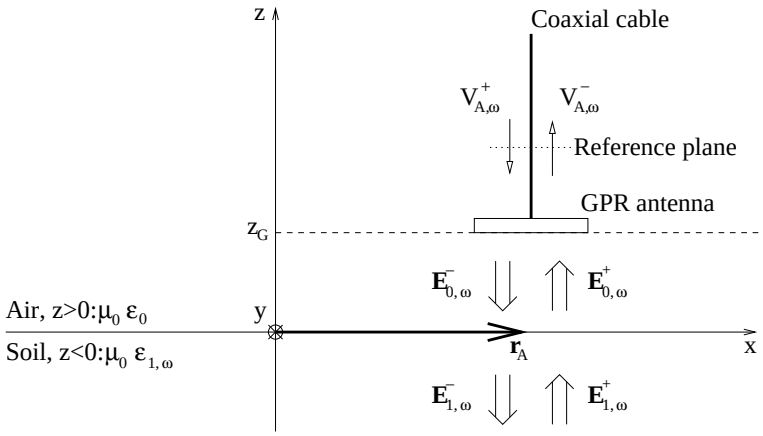

Figure 2.3: Configuration for the definition of the PWTS in soil. The air-soil interface is considered as an integrated part of the GPR antenna.

and the field $\mathbf{E}^{\pm}_{1,\omega}$ in the soil is written in terms of a plane-wave expansion as

$$\mathbf{E}^{\pm}_{1,\omega}(\mathbf{r}) = \frac{1}{(2\pi)^2}\iint_{-\infty}^{\infty} \widetilde{\mathbf{E}}^{\pm}_{1,\omega}(k_x,k_y)e^{i\mathbf{k}^{\pm}_{1,\omega}(k_x,k_y)\cdot\mathbf{r}}dk_xdk_y, z<0. \quad (2.21)$$

Herein, $\widetilde{\mathbf{E}}^{\pm}_{1,\omega} = \widetilde{E}^{\pm}_{1x,\omega}\hat{\mathbf{x}} + \widetilde{E}^{\pm}_{1y,\omega}\hat{\mathbf{y}} + \widetilde{E}^{\pm}_{1z,\omega}\hat{\mathbf{z}}$ is the plane-wave spectrum of the electric field in the soil, and the propagation vector in the soil is defined as

$$\mathbf{k}^{\pm}_{1,\omega}(k_x,k_y) = \hat{\mathbf{x}}k_x + \hat{\mathbf{y}}k_y \pm \hat{\mathbf{z}}\gamma_{1,\omega}(k_x,k_y), \quad (2.22)$$

with the $\hat{\mathbf{z}}$-component defined in terms of the spatial frequencies k_x and k_y as

$$\gamma_{1,\omega}(k_x,k_y) = \begin{cases} \sqrt{k^2_{1,\omega} - k_x^2 - k_y^2} & \omega \geq 0 \\ -(\gamma_{1,-\omega}(k_x,k_y))^* & \omega < 0, \end{cases} \quad (2.23)$$

where the imaginary part of $\gamma_{1,\omega}$ is nonnegative. In Figure 2.4, the unbroken line is the curve for the normalized imaginary part of $\gamma_{1,\omega}$ plotted as a function of the normalized real part of $\gamma_{1,\omega}$ when the loss tangent is $\tan\delta_{1,\omega} = \varepsilon''_{1,\omega}/\varepsilon'_{1,\omega} = 0.1$. The dotted and dashed lines are given by $k_x^2 + k_y^2 = 0$ and $k_x^2 + k_y^2 = \omega^2\mu_0\varepsilon'_{1,\omega}$, respectively. Due to the losses in the soil, the amplitude of the electric field is exponentially decreasing in the direction of propagation for all $k_x^2 + k_y^2$. However, the exponential decrease of the amplitudes of plane waves is strong for $k_x^2 + k_y^2 > \omega^2\mu_0\varepsilon'_{1,\omega}$. Therefore, plane waves

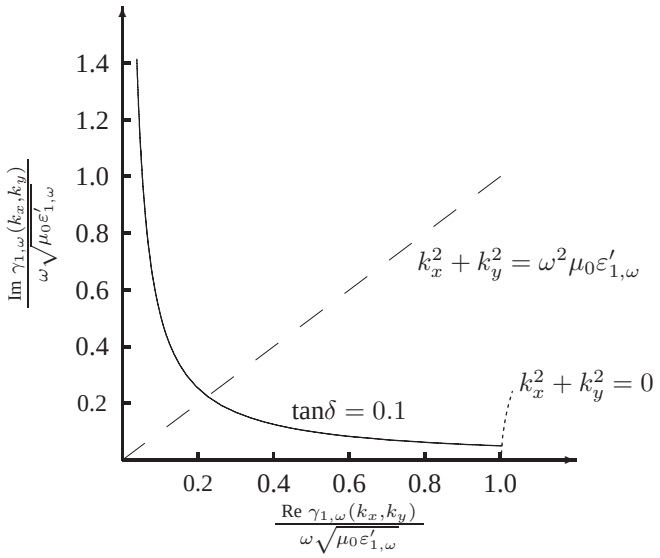

Figure 2.4: The normalized imaginary part of $\gamma_{1,\omega}$ as a function of the normalized real part for a positive angular frequency $\omega > 0$.

with $k_x^2 + k_y^2 > \omega^2 \mu_0 \varepsilon'_{1,\omega}$ are denoted by evanescent waves while plane waves with $k_x^2 + k_y^2 \leq \omega^2 \mu_0 \varepsilon'_{1,\omega}$ are denoted by propagating waves.

The plane-wave spectra fulfill the criteria $\mathbf{k}^{\pm}_{0,\omega}(k_x, k_y) \cdot \widetilde{\mathbf{E}}^{\pm}_{0,\omega}(k_x, k_y) = 0$ and $\mathbf{k}^{\pm}_{1,\omega}(k_x, k_y) \cdot \widetilde{\mathbf{E}}^{\pm}_{1,\omega}(k_x, k_y) = 0$ and they are given by the two-dimensional Fourier transforms

$$\widetilde{\mathbf{E}}^{\pm}_{0,\omega}(k_x, k_y) = \iint_{-\infty}^{\infty} \mathbf{E}^{\pm}_{0,\omega}(\mathbf{r}) e^{-i[\mathbf{k}^{\pm}_{0,\omega}(k_x,k_y)\cdot\mathbf{r}]} dxdy, 0 < z < z_G, \quad (2.24)$$

and

$$\widetilde{\mathbf{E}}^{\pm}_{1,\omega}(k_x, k_y) = \iint_{-\infty}^{\infty} \mathbf{E}^{\pm}_{1,\omega}(\mathbf{r}) e^{-i[\mathbf{k}^{\pm}_{1,\omega}(k_x,k_y)\cdot\mathbf{r}]} dxdy, z < 0. \quad (2.25)$$

The plane-wave spectrum of the radiated electric field in the soil is written in terms of the PWTS as

$$\widetilde{\mathbf{E}}^{-}_{1,\omega}(k_x, k_y) = V^{+}_{A,\omega}(\mathbf{r}_A) \mathbf{T}_{A1,\omega}(k_x, k_y) e^{-i[k_x x_A + k_y y_A]}, z < 0, \quad (2.26)$$

so that the radiated electric field is expressed as

$$\mathbf{E}^{-}_{1,\omega}(\mathbf{r}) = \frac{V^{+}_{A,\omega}(\mathbf{r}_A)}{(2\pi)^2} \iint_{-\infty}^{\infty} \mathbf{T}_{A1,\omega}(k_x, k_y) e^{i[\mathbf{k}^{\pm}_{1,\omega}(k_x,k_y)\cdot(\mathbf{r}-\mathbf{r}_A)]} dk_x dk_y, \quad z < 0. \quad (2.27)$$

The voltage $V^{-}_{A,\omega}$ of the outgoing wave is written as

$$V^{-}_{A,\omega}(\mathbf{r}_A) = V^{+}_{A,\omega}(\mathbf{r}_A)\Gamma_{A1,\omega} + \frac{1}{(2\pi)^2} \iint_{-\infty}^{\infty} \mathbf{R}_{A1,\omega}(k_x, k_y) \cdot \widetilde{\mathbf{E}}^{+}_{1,\omega}(k_x, k_y) e^{i[k_x x_A + k_y y_A]} dk_x dk_y, \quad (2.28)$$

where the reflection coefficient of the GPR antenna is defined as

$$\Gamma_{A1,\omega} = \left. \frac{V^{-}_{A,\omega}}{V^{+}_{A,\omega}} \right|_{\mathbf{E}^{+}_{1,\omega}(\mathbf{r})=\mathbf{0}}. \quad (2.29)$$

Using the boundary conditions at $z = 0$ as suggested by Meincke and Hansen in [22] the reciprocity relation can be derived as

$$\mathbf{R}_{A1,\omega}(k_x, k_y) = \frac{\gamma_{1,\omega}(k_x, k_y)}{\omega \mu_0 Y_c} \mathbf{T}_{A1,\omega}(-k_x, -k_y). \quad (2.30)$$

The air-soil interface is an integrated part of the GPR antenna so that the GPR antenna is considered as an antenna in a homogeneous medium with the complex permittivity $\varepsilon_{1,\omega}$ when fields in the region $z < 0$ are considered. The reciprocity relation for the

GPR antenna in (2.30) follows from the reciprocity relations in free space in (2.16) so that (2.30) appears from (2.16) by replacing the free space permittivity ε_0 with $\varepsilon_{1,\omega}$. If an air gap $z_G > 0$ is present between the radiating parts of the GPR antenna and the air-soil interface the plane waves in air for $k_{0,\omega}^2 < k_x^2 + k_y^2$ are attenuated. This attenuation causes small amplitudes of the PWTS and PWRS for $k_{0,\omega}^2 \ll k_x^2 + k_y^2$.

If multiple interactions between the GPR antenna and the air-soil interface are negligible then the PWTS $\mathbf{T}_{A1,\omega}$ in the presence of an air-soil interface is related to the PWTS $\mathbf{T}_{A0,\omega}$ in free space as

$$\mathbf{T}_{A1,\omega}(k_x, k_y) = \overline{\mathbf{L}}_{10,\omega}(k_x, k_y) \cdot \mathbf{T}_{A0,\omega}(k_x, k_y), \tag{2.31}$$

where $\overline{\mathbf{L}}_{10,\omega}$ is the transmission dyadic which describes the transmission of the plane waves from air to soil.

Similarly, the PWRS $\mathbf{R}_{A1,\omega}$ is related to the PWRS $\mathbf{R}_{A0,\omega}$ in free space as

$$\mathbf{R}_{A1,\omega}(k_x, k_y) = \overline{\mathbf{L}}_{01,\omega}(k_x, k_y) \cdot \mathbf{R}_{A0,\omega}(k_x, k_y), \tag{2.32}$$

where $\overline{\mathbf{L}}_{01,\omega}$ is the transmission dyadic which describes the transmission of the plane waves from soil to air. The transmission dyadics are related through the relation

$$\overline{\mathbf{L}}_{10,\omega}(k_x, k_y) = \frac{\gamma_{0,\omega}(k_x, k_y)}{\gamma_{1,\omega}(k_x, k_y)} \overline{\mathbf{L}}_{01,\omega}(-k_x, -k_y). \tag{2.33}$$

Throughout most of the work we do not assume that the multiple interactions between the GPR antenna and the air-soil interface are negligible. The plane-wave theory for a GPR antenna radiating in soil with the complex permittivity $\varepsilon_{1,\omega}$ is used in Section 2.3 to develop a measurement procedure as suggested by Meincke and Hansen in [22].

2.2 Definition of Antenna Parameters

Antenna parameters, such as gain and directivity, describe the key features of antennas used in communication systems [44]. These parameters are far-field parameters and hence not applicable to GPR systems.

Therefore, near-field parameters as defined by Lenler-Eriksen and Meincke in [27] are more suitable for the characterization of the GPR antennas. These parameters are reviewed in this section and defined on the basis of the fields tangential to the plane $z = 0$. The power $P_{S,\omega}$ transmitted through the air-soil interface is written as

$$P_{S,\omega} = \frac{-\hat{\mathbf{z}}}{2} \cdot \iint_{-\infty}^{\infty} \mathrm{Re}\left[\mathbf{E}_{1,\omega}^{-}(x, y) \times \mathbf{H}_{1,\omega}^{-}{}^{*}(x, y)\right] dxdy. \tag{2.34}$$

This power can also be expressed in terms of the PWTS as

$$P_{S,\omega} = \frac{|V_{A,\omega}^{+}|^2}{8\pi^2 \omega \mu_0} \iint_{-\infty}^{\infty} \mathrm{Re}\left[\gamma_{1,\omega}(k_x, k_y)\right] |\mathbf{T}_{A,\omega}(k_x, k_y)|^2 \, dk_x dk_y. \tag{2.35}$$

The power $P_{A,\omega}$ accepted by the antenna is

$$P_{A,\omega} = \frac{Y_c}{2}(1 - |\Gamma_{A1,\omega}|^2)|V^+_{A,\omega}|^2. \tag{2.36}$$

If a step-frequency system is used, it is reasonable to apply a frequency dependent transmission efficiency $\eta_{A,\omega}$, defined as

$$\eta_{A,\omega} = \frac{P_{S,\omega}}{P_{A,\omega}}. \tag{2.37}$$

In order to describe the electric field tangential to the plane $z = 0$, the transmission efficiency is divided into two partial transmission efficiencies

$$\eta_{Ax,\omega} = P_{Sx,\omega}/P_{A,\omega}, \tag{2.38}$$
$$\eta_{Ay,\omega} = P_{Sy,\omega}/P_{A,\omega}. \tag{2.39}$$

$P_{Sx,\omega}$ and $P_{Sy,\omega}$ are the powers transmitted through the air-soil interface due to the $\hat{\mathbf{x}}$- and $\hat{\mathbf{y}}$-polarized tangential electric fields in the plane $z = 0$, respectively. The power $P_{Sx,\omega}$ is defined as

$$P_{Sx,\omega} = \frac{-1}{2}\iint_{-\infty}^{\infty} \text{Re}\left[\hat{\mathbf{x}} \cdot \mathbf{E}^-_{1,\omega}(x,y)\ \hat{\mathbf{y}} \cdot {\mathbf{H}^-_{1,\omega}}^*(x,y)\right] dxdy, \tag{2.40}$$

and similarly for $P_{Sy,\omega}$. It is observed that

$$\eta_{Ax,\omega} + \eta_{Ay,\omega} = \eta_{A,\omega}. \tag{2.41}$$

The power $P_{Sx,\omega}$ in (2.40) can be written in terms of the PWTS as

$$P_{Sx,\omega} = \frac{|V^+_{A,\omega}|^2}{8\pi^2\omega\mu_0}\iint_{-\infty}^{\infty} \text{Re}\Big[\gamma_{1,\omega}(k_x,k_y)\,|T_{A1x,\omega}(k_x,k_y)|^2 + k_x {T_{A1x,\omega}}^*(k_x,k_y)T_{A1z,\omega}(k_x,k_y)]\,dk_xdk_y. \tag{2.42}$$

The partial transmission efficiency can also be defined with respect to right-hand and left-hand circularly polarized electric fields as

$$\eta_{Arhcp,\omega} = P_{Srhcp,\omega}/P_{A,\omega}, \tag{2.43}$$
$$\eta_{Alhcp,\omega} = P_{Slhcp,\omega}/P_{A,\omega}. \tag{2.44}$$

The power $P_{Srhcp,\omega}$ is defined as

$$P_{Srhcp,\omega} = \frac{1}{2}\iint_{-\infty}^{\infty} \text{Re}\left[\hat{\mathbf{e}}^*_{rhcp} \cdot \mathbf{E}^-_{1,\omega}(x,y)\ (-i\hat{\mathbf{e}}_{rhcp}) \cdot {\mathbf{H}^-_{1,\omega}}^*(x,y)\right] dxdy, \tag{2.45}$$

where

$$\hat{\mathbf{e}}_{rhcp} = (\hat{\mathbf{x}} - i\hat{\mathbf{y}})/\sqrt{2}, \tag{2.46}$$

and similarly for $P_{Slhcp,\omega}$. It is observed that

$$\eta_{Arhcp,\omega} + \eta_{Alhcp,\omega} = \eta_{A,\omega}. \tag{2.47}$$

The power $P_{Srhcp,\omega}$ can be written in terms of the plane-wave transmitting spectrum as

$$\begin{aligned} P_{Srhcp,\omega} = \frac{|V^+_{A,\omega}|^2}{16\pi^2\omega\mu_0} \iint_{-\infty}^{\infty} \mathrm{Re}\Big[\gamma_{1,\omega}(k_x,k_y)\,|\mathbf{T}_{A1,\omega}(k_x,k_y)|^2 \\ + 2\gamma_{1,\omega}(k_x,k_y)\,\mathrm{Im}\left[T_{A1x,\omega}{}^*(k_x,k_y)T_{A1y,\omega}(k_x,k_y)\right] \\ -iT_{A1z,\omega}(k_x,k_y)\left(k_yT_{A1x,\omega}{}^*(k_x,k_y) - k_xT_{A1y,\omega}{}^*(k_x,k_y)\right)\Big]\,dk_xdk_y. \end{aligned} \tag{2.48}$$

If time-domain systems are considered it is more reasonable to consider the ratio between the total power P_A accepted by the GPR antenna to the total transmitted power P_S in the soil. The total transmitted power in the soil is written as

$$\begin{aligned} P_S = -\hat{\mathbf{z}}\cdot \iiint_{-\infty}^{\infty} \mathbf{E}^-_{1,t}(x,y)\times\mathbf{H}^-_{1,t}(x,y)dxdydt \\ = 8\pi\int_0^{\infty} P_{S,\omega}d\omega, \end{aligned} \tag{2.49}$$

where $\mathbf{E}^-_{1,t}$ and $\mathbf{H}^-_{1,t}$ are the electric and magnetic fields of the downward propagating wave in the time domain, respectively. Similarly, the total power P_A accepted by the antenna is given by

$$P_A = \int_{-\infty}^{\infty} V_{A,t}I_{A,t}dt = 8\pi\int_0^{\infty} P_{A,\omega}d\omega, \tag{2.50}$$

where $V_{A,t}$ and $I_{A,t}$ are the total voltage and current at the reference plane in the time domain, respectively. The total transmission efficiency is defined as the ratio

$$\eta_A = \frac{P_S}{P_A}. \tag{2.51}$$

that depends on the transmit waveform of the system. The defined antenna parameters give information about the utility of the GPR antenna, and these parameters are calculated for GPR antennas in Chapter 4.

2.3 Calculation of the Plane-Wave Transmitting Spectrum

As seen in Section 2.1, the plane-wave theory in free space is suitable for description of the field radiated by an antenna. Therefore, techniques for measurement of the PWTS in free space are usable for measurement of the radiated fields from a GPR antenna under test (AUT). A configuration is considered in Figure 2.5 in which the GPR antenna is radiating a field in the soil, and the radiated field is measured by two probes buried in the soil. The usual xyz-coordinate system is used with the z-axis pointing into the upper half space and the air-soil interface is located at $z = 0$. The constitutive parameters are defined as in Section 2.1.2 and the voltages $V_{A,\omega}$, $V^-_{A,\omega}$, and $V^+_{A,\omega}$ are defined as in Section 2.1.1. The reference points for the probes are chosen so that they are coinciding with the origin of the coordinate system. The two probes, referred to as probe 1 and 2, are buried at fixed positions in the soil and they are fed through coaxial cables using a single TEM mode. The characteristic admittance of the cables is denoted by Y_c. The reference plane for probe 1 is chosen in the coaxial cable and the voltages of the incoming and outgoing waves at the reference plane are denoted by $V^+_{1P,\omega}$ and $V^-_{1P,\omega}$, respectively. Similarly, the voltages of the incoming and outgoing waves for probe 2 are denoted by $V^+_{2P,\omega}$ and $V^-_{2P,\omega}$, respectively. The total voltages are denoted by $V_{nP,\omega} = V^+_{nP,\omega} + V^-_{nP,\omega}$ for $n = 1, 2$. If the current distribution $\mathbf{J}_{nP,\omega}$ on the probe is known, the PWRS $\mathbf{R}_{nP,\omega} = R_{nPx,\omega}\hat{\mathbf{x}} + R_{nPy,\omega}\hat{\mathbf{y}} + R_{nPz,\omega}\hat{\mathbf{z}}$ of the probe is calculated as suggested by Lenler-Eriksen and Meincke in [32]

$$\begin{aligned}\mathbf{R}_{nP,\omega}(k_x, k_y) = &-\frac{1}{V^+_{nP,\omega} 2Y_c}\left(\overline{\mathbf{I}} - \frac{\mathbf{k}^-_{1,\omega}(k_x, k_y)\mathbf{k}^-_{1,\omega}(k_x, k_y)}{k^2_{1,\omega}}\right) \\ &\cdot \iiint_{V'} \mathbf{J}_{nP,\omega}(\mathbf{r}') e^{i\mathbf{k}^-_{1,\omega}(k_x,k_y)\cdot\mathbf{r}'} dx'dy'dz', z > z',\end{aligned} \tag{2.52}$$

where the region V' contains all the currents on the probe. The voltage transfer functions between the probes and the GPR AUT are defined as

$$S_{nPA,\omega}(\mathbf{r}_A) = \left.\frac{V^-_{nP,\omega}(\mathbf{r}_A)}{V^+_{A,\omega}(\mathbf{r}_A)}\right|_{V^+_{nP,\omega}(\mathbf{r}_A)=0}, \tag{2.53}$$

$$S_{nAP,\omega}(\mathbf{r}_A) = \left.\frac{V^-_{A,\omega}(\mathbf{r}_A)}{V^+_{nP,\omega}(\mathbf{r}_A)}\right|_{V^+_{A,\omega}(\mathbf{r}_A)=0}. \tag{2.54}$$

The GPR AUT and the probe are assumed to be reciprocal antennas, implying that the relation

$$S_{nPA,\omega}(\mathbf{r}_A) = S_{nAP,\omega}(\mathbf{r}_A), \tag{2.55}$$

can be used [21], [22]. If multiple interactions between the probes and the GPR AUT are negligible, the voltage transfer function can be written as suggested by Lenler-Eriksen and Meincke in [32], [33] as

$$\widetilde{S}_{nPA,\omega}(-k_x,-k_y) = \mathbf{R}_{nP,\omega}(k_x,k_y)\cdot\mathbf{T}_{A,\omega}(k_x,k_y), \tag{2.56}$$

where $\widetilde{S}_{nPA,\omega}$ is the Fourier transform of the measured voltage transfer function given by

$$\widetilde{S}_{nPA,\omega}(k_x,k_y) = \iint_{-\infty}^{\infty} S_{nPA,\omega}(\mathbf{r}_A)e^{-i[k_x x_A + k_y y_A]}dx_A dy_A. \tag{2.57}$$

Using the relation $\mathbf{k}^{-}_{1,\omega}(k_x,k_y)\cdot\mathbf{T}_{A1,\omega}(k_x,k_y) = 0$, the equation for the voltage transfer function (2.56) is rewritten as

$$\frac{\boldsymbol{W}_{nP,\omega}(k_x,k_y)}{\gamma_{1,\omega}(k_x,k_y)}\cdot(\hat{\mathbf{x}}T_{Ax,\omega}(k_x,k_y)+\hat{\mathbf{y}}T_{Ay,\omega}(k_x,k_y)) = \widetilde{S}_{nPA,\omega}(-k_x,-k_y), \tag{2.58}$$

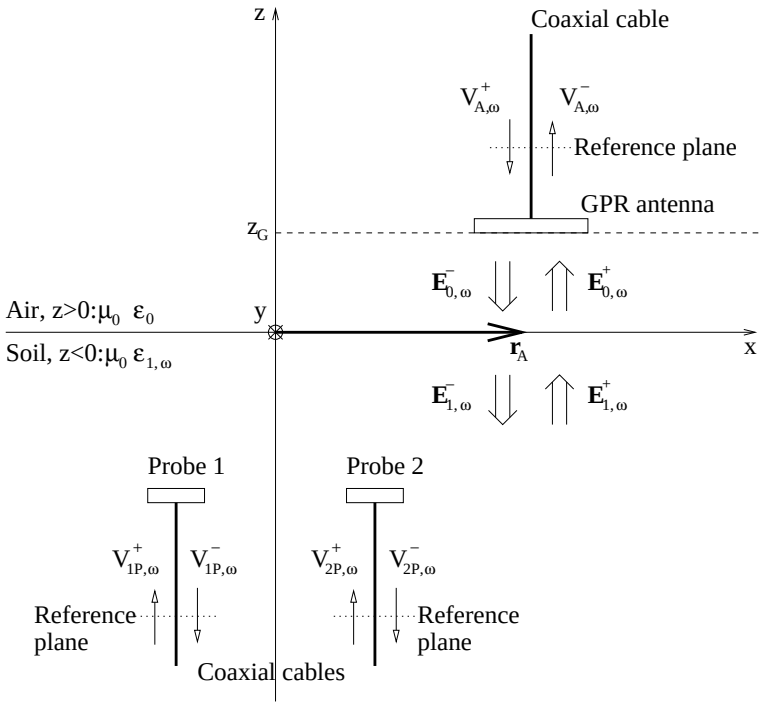

Figure 2.5: Configuration for the measurement of the transmitting spectrum of a GPR antenna. The field radiated by the GPR antenna is measured by the probes in the soil.

where the vector $\boldsymbol{W}_{nP,\omega}$ is given by

$$\begin{aligned}\boldsymbol{W}_{nP,\omega}(k_x,k_y) = &\left(\gamma_\omega(k_x,k_y)R_{nPx,\omega}(k_x,k_y) + k_x R_{nPz,\omega}(k_x,k_y)\right)\hat{\mathbf{x}} \\ &+ \left(\gamma_\omega(k_x,k_y)R_{nPy,\omega}(k_x,k_y) + k_y R_{nPz,\omega}(k_x,k_y)\right)\hat{\mathbf{y}}. \quad (2.59)\end{aligned}$$

The plane-wave transmitting spectrum can now be found by solving the matrix equation

$$\begin{bmatrix}\gamma_{1,\omega}R_{1Px,\omega}(k_x,k_y) + k_x R_{1Pz,\omega}(k_x,k_y) & \gamma_{1,\omega}R_{1Py,\omega}(k_x,k_y) + k_y R_{1Pz,\omega}(k_x,k_y) \\ \gamma_{1,\omega}R_{2Px,\omega}(k_x,k_y) + k_x R_{2Pz,\omega}(k_x,k_y) & \gamma_{1,\omega}R_{2Py,\omega}(k_x,k_y) + k_y R_{2Pz,\omega}(k_x,k_y)\end{bmatrix}$$
$$\cdot \begin{bmatrix}T_{A1x,\omega}(k_x,k_y) \\ T_{A1y,\omega}(k_x,k_y)\end{bmatrix}\frac{1}{\gamma_{1,\omega}} = \begin{bmatrix}\widetilde{S}_{1PA,\omega}(-k_x,-k_y) \\ \widetilde{S}_{2PA,\omega}(-k_x,-k_y)\end{bmatrix}, \quad (2.60)$$

where $\gamma_{1,\omega}$ is written without the arguments k_x and k_y. If the plane-wave receiving spectrum of the two probes is known, and if the two vectors in (2.59) are different from zero and linearly independent, that is

$$\boldsymbol{W}_{1P,\omega}(k_x,k_y) \times \boldsymbol{W}_{2P,\omega}(k_x,k_y) \neq \mathbf{0}, \quad (2.61)$$

then one solution can be found for the plane-wave transmitting spectrum of the GPR AUT by solving (2.60). The criteria in (2.61) can also be rewritten as [26]

$$\mathbf{k}_\omega^+(k_x,k_y) \cdot \left(\mathbf{R}_{1P,\omega}(k_x,k_y) \times \mathbf{R}_{2P,\omega}(k_x,k_y)\right) \neq 0. \quad (2.62)$$

If a near-null is encountered, numerical problems will be encountered when solving (2.60).

This may be caused by a near-null in the amplitude of $\mathbf{R}_{nP,\omega}$ or a small angle Φ_ω between $\boldsymbol{W}_{1,\omega}$ and $\boldsymbol{W}_{2,\omega}$. In the case of a near-null amplitude of $\mathbf{R}_{nP,\omega}$, the voltage transfer function $\widetilde{S}_{nPA,\omega}$ will only contain noise which will be amplified during the calculation of the PWTS of the AUT. The angle Φ_ω between $\boldsymbol{W}_{1,\omega}$ and $\boldsymbol{W}_{2,\omega}$ is defined as

$$\cos(\Phi_\omega(k_x,k_y)) = \frac{(\boldsymbol{W}_{1,\omega}(k_x,k_y))^* \cdot \boldsymbol{W}_{2,\omega}(k_x,k_y)}{|\boldsymbol{W}_{1,\omega}(k_x,k_y)|\,|\boldsymbol{W}_{2,\omega}(k_x,k_y)|}. \quad (2.63)$$

The amplitude of $\cos(\Phi_\omega)$ must be as low as possible for the measurement procedure to be sufficiently insensitive to model errors and noise. From the Cauchy-Schwarz inequality

$$|(\boldsymbol{W}_{1,\omega}(k_x,k_y))^* \cdot \boldsymbol{W}_{2,\omega}(k_x,k_y)| \leq |\boldsymbol{W}_{1,\omega}(k_x,k_y)|\,|\boldsymbol{W}_{2,\omega}(k_x,k_y)| \quad (2.64)$$

it is seen that $|\cos(\Phi_\omega)| \leq 1$. In practice, a maximum value ξ for $|\cos(\Phi_\omega)|$ is chosen in the interval $0 < \xi < 1$. Two probes are only considered to be usable in the region $|\cos(\Phi_\omega)| < \xi$. A similar procedure is suggested by Kerns in [21], in which the parameter $1 - \cos^2(\Phi_\omega)$ is considered.

The suggested method for measurements of GPR antennas is used in Chapter 4. The measured PWTS is used for imaging in Chapter 5.

2.4 Summary

The radiation of an electromagnetic field by a GPR antenna is characterized using the PWTS. If multiple interactions between the GPR antenna and the air-soil interface are non-negligible then the air-soil interface is considered as an integrated part of the GPR antenna. Therefore, the PWTS is a description of the combined system of the GPR antenna and the air-soil interface. The PWTS gives an exact description of the radiated electromagnetic field at any distance from the interface in the soil. Antenna parameters based on the measured fields tangential to the air-soil interface have been defined.

Finally, a procedure for measurement of the PWTS using two buried probes is suggested. In this procedure, multiple interactions between the probe and the air-soil interface are neglected, and the PWRS of the probe is calculated using knowledge about the current distribution at the probes. The parameter $\cos(\Phi_\omega)$ for the solvability of the set of equations for calculation of the PWTS has been defined like the parameter suggested by Kerns in [21].

Chapter 3

Characterization of the Loop Antenna for GPR Radiation Measurements

Development of probes for measurement of the electromagnetic radiation in the soil by GPR antennas is a new topic that has arisen within the last decade. The first measurement facilities for GPR antennas were built in 1998 at TU Delft in the Netherlands [41], [20], [42]. In these facilities a loop antenna with a circumference of 107 mm is used for measurements of the electromagnetic field in homogeneous sand. The loop antenna is reported in [19] as being an ultra-wideband sensor usable for time-domain measurements. In [19] the sensitivity in free space is measured for one set of spatial frequencies using the three-antenna method. The measured sensitivity is compared with a theoretical sensitivity that is calculated using a feeding line model and a model based on the thin wire approximation as suggested by Wu [45]. For the considered set of frequencies, the measured sensitivity agrees with the theoretical sensitivity. It is concluded that the loop antenna has a high sensitivity in the frequency range from 180 MHz to 3880 MHz. In this frequency range the loop antenna performs like an electromagnetic sensor that qualitatively replicates the wave form of the incident field.

So far, the model of the loop antenna has been based on the thin wire approximation for a loop antenna in free space. It is desirable to develop a model for the loop antenna that can be used for an arbitrary wire thickness since the broad band properties improve as the wire thickness increases [43, pp. 224-228] since the stored reactive energy is minimized [12, pp. 174-175]. Furthermore, as seen in Appendix B, the fields and current distributions for the loop antenna in free space are only usable for media with a loss tangent equal to zero. As, the loss tangent for soil is significantly different from zero, it is desirable to develop a model that can be used in a medium with an arbitrary loss tangent. The effect of increased dielectric losses in the soil is believed

to be similar to the effect of increased losses in narrow band resonant circuits [12, pp. 180-190]. Increased losses decrease the Q-value of the system and consequently, the bandwidth is increased. However, the sensitivity of the loop antenna will be decreased due to the loss in the transmission between the air-soil interface and the loop antenna. Furthermore, the loop antenna is used for measurements of GPR antennas in the near-field region, so it desirable to consider reception and transmission of a spectrum of plane waves. To this end, the plane-wave receiving spectrum of the loop should be considered instead of the reception of a single plane wave.

The best choice for the orientation of the loop antenna in the soil is not obvious for two reasons. First, the electric field is measured in the near-field region of the GPR antenna so that the electric field is a sum of plane waves instead of a single plane wave. The near-field pattern for a dipole close to the air-soil interface is calculated and compared with the far-field pattern by Kruk et al. in [46]. It is concluded that the near-field pattern does not necessarily resemble the far-field pattern. Therefore, one should be careful to perform conclusions about the usability of the loop antenna based on the far-field pattern. However, an investigation of the far-field patterns of the loop antenna can be instructive. Far-field considerations are performed for the loop antenna in this chapter. Second, the loop antenna can not be considered to be the classical small loop antenna as described in standard text books [43, pp. 204-217]. The far-field pattern of a small loop antenna is similar to the pattern of a small dipole so that the loop antenna has a null along its axis of symmetry. As the circumference of the loop antenna increases the radiation along its axis increases and reaches a maximum at about one wavelength [47]. For a loop in free space with a circumference of 107 mm the maximum is reached at the frequency 2.8 GHz. One should therefore keep in mind that the radiation pattern from the considered loop antenna is very different from the radiation pattern of a small loop antenna.

In this thesis the outer surface of the loop antenna is described as a perfectly electrically conductive structure. The current distribution at the outer surface of the loop antenna is calculated using the Method of Moment (MoM) procedure developed by Jørgensen et al. [28]. The current distribution can be calculated for a loop antenna with an arbitrary thickness in a medium with an arbitrary loss tangent. Following the procedure of Yarovoy et al. [19] feeding line models are developed for the loop antenna, which subsequently make it posible to calculate the plane-wave receiving spectrum. Methods for estimation of model parameters are developed, and the models are used for probe correction during measurement of GPR antennas.

In Section 3.1 a model of the loop antenna is suggested. A method for estimation of model parameters is suggested in Section 3.2. The model is verified in Section 3.3 by comparison of measured results with simulated results. Moreover, uncertainty calculations are performed.

3.1 The Model of the Loop Antenna

The considered loop antenna with a circumference of 107 mm, as shown in Figure 3.1 was suggested by Goedbloed as a handy H-field probe in the frequency-range from 20 MHz to 1 GHz for measurements of electromagnetic radiation within the framework of electromagnetic compatibility (EMC) [48]. The loop antenna is constructed in a three-step procedure. First, two SMA connectors are attached to the ends of a semi-rigid cable of type UT-141A. One SMA connector will be used for termination in a load with the characteristic admittance $Y_c = 20$ mS and the other SMA connector will be used as the feed for the loop antenna. Then, subsequently the loop antenna is formed by bending the cable. Finally, a cut with a width of 0.5 mm in the outer conductor of the semi-rigid cable is made. This cut is used for excitation of the loop and it is denoted by the excitation cut. The loop antenna is modelled using the following two submodels:

- The submodel of the semi-rigid cable between the reference plane at the feed connector and the reference plane at the excitation cut. This submodel is described in Section 3.1.1.
- The submodel of the excitation cut, the outer surface of the loop antenna, and the termination in the load. This submodel is described in Section 3.1.2.

In the following, two types of loop antennas denoted by loop A and B are considered. Loop A is made of 65 cm long semi-rigid cable as shown in Figure 3.2. Loop B is similar to loop A apart from two facts. First, loop B is made of a 5 m long semi-rigid cable UT-141A. The loop is constructed so that the excitation cut is 30 cm from the SMA connector with the admittance 20 mS. The distance from the feed to the excitation cut is 4.7 m. The larger distance between the feed and the excitation cut makes it more difficult to model the semi-rigid cable between the reference plane at the feed and the reference plane at the excitation cut. Then, the semi-rigid cable is

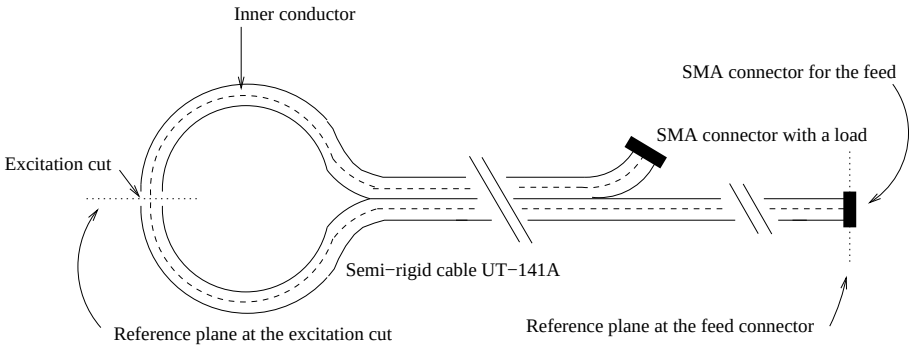

Figure 3.1: The construction and modelling of the loop antenna.

Figure 3.2: Loop antenna A. This loop antenna is made of a 65 cm long semi-rigid cable UT-141A.

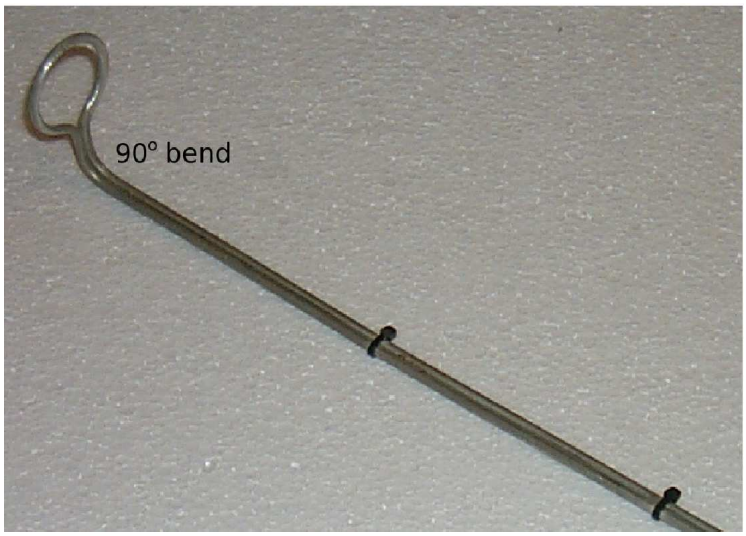

Figure 3.3: Loop antenna B. This loop antenna is made of a 5 m long semi-rigid cable UT-141A.

bent 90^o near the loop as shown in Figure 3.3. This bend is included in the model of the surface of the loop in Section 3.1.2.

3.1.1 Model of the Coaxial Cable from the Feed to the Excitation Cut of the Loop Antenna

Accurate modelling of the semi-rigid cable UT-141A is a key issue in the model of the loop antenna, so an investigation of the properties of this cable is performed in the following section.

As listed in Table 3.1 the semi-rigid cable UT-141A is a coaxial cable with a center conductor of a diameter $2a = 0.91$ mm and a dielectric diameter $2b = 2.98$ mm. The center conductor is made of a silver plated cobber wire (SPCW), and the outer conductor is made of cobber (Cu), as shown in Figure 3.4. The conductivity of silver and cobber is $\sigma_{Ag} = 61.73$ MS/m and $\sigma_{Cu} = 58.13$ MS/m, respectively, so that the center conductor and the outer conductor are good conductors [12, pp. 704]. The dielectric is made of polytetrafluoroethylene (PTFE) also denoted as teflon with the relative permittivity $\varepsilon'_{d,\omega}/\varepsilon_0 = 2.0$. The loss tangent is specified as $\tan\delta_{d,\omega} = 0.0004$ at the frequency 10 GHz at the temperature 25^o C [12, pp. 705].

The coaxial cable is considered as a low-loss line and the characteristic admittance is calculated as suggested in [49, pp. 56-98]

$$Y_c = \frac{2\pi}{\ln\left(\frac{b}{a}\right)}\sqrt{\frac{\varepsilon'_{d,\omega}}{\mu_0}}, \tag{3.1}$$

and the characteristic admittance is $Y_c = 20$ mS. In Figure 3.5 the coaxial cable between the feed and the excitation cut is considered and the voltages of the incoming and outgoing wave in the reference plane at the feed connector are denoted by $V^+_{P,\omega}$ and $V^-_{P,\omega}$, respectively. The voltages of the incoming and outgoing waves in the reference plane at the excitation cut are denoted by $V^+_{E,\omega}$ and $V^-_{E,\omega}$, respectively. The measured reflection coefficient $S_{PP,\omega}$ at the reference plane of the feed connector is defined as

$$S_{PP,\omega} = \frac{V^-_{P,\omega}}{V^+_{P,\omega}}, \tag{3.2}$$

Outer conductor diameter (mm)	3.58 ± 0.7 %
Dielectric diameter (mm)	2.98 ± 0.9 %
Center conductor diameter (mm)	0.91 ± 2.8 %
Minimum inside bending radius (mm)	1.91
Relative permittivity of dielectric	2.0
Characteristic admittance, Y_c (mS)	20

Table 3.1: Data for the semi-rigid cable UT-141A.

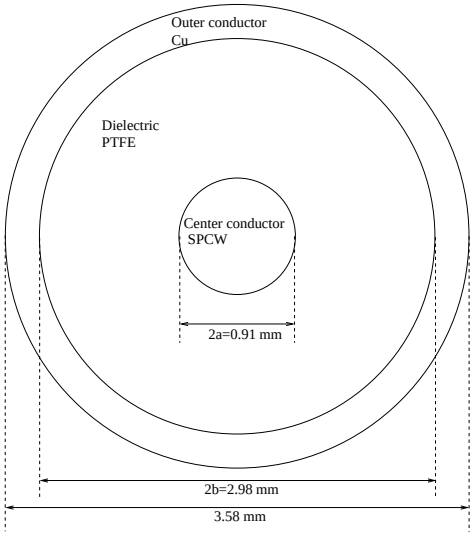

Figure 3.4: Cross section of the semi-rigid cable UT-141A.

and the reflection coefficient at the excitation cut is defined as

$$S_{EE,\omega} = \frac{V^-_{E,\omega}}{V^+_{E,\omega}}. \tag{3.3}$$

The reflection coefficient $S_{PP,\omega}$ is used for calculation of the reflection coefficient $S_{EE,\omega}$ at the reference plane of the excitation cut. The relation between these two reflection coefficients is given by

$$S_{EE,\omega} = S_{PP,\omega} e^{i2l_c\gamma_{c,\omega}} \tag{3.4}$$

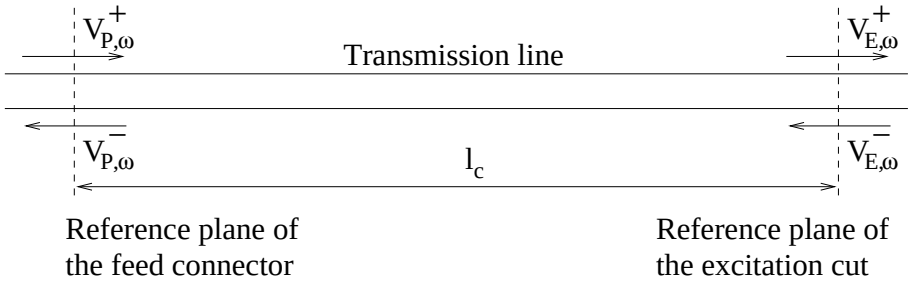

Figure 3.5: The coaxial cable between the feed connector and the excitation gap.

where l_c is the distance between the reference planes and the propagation constant $\gamma_{c,\omega}$ is given by

$$\gamma_{c,\omega} = \omega\sqrt{\mu_0\varepsilon'_{d,\omega}} + i\frac{\ln(10)\alpha_\omega}{20}, \tag{3.5}$$

where the loss constant in dB/m is denoted by α_ω. The loss constant depends on dielectric losses and conductive losses in the conductors. The typical loss constant for the semi-rigid cable UT-141A is given by [12, pp. 708]

$$\alpha_\omega = 0.40\frac{\text{dB}}{\text{m}}\left(\frac{f}{1GHz}\right)^{0.583}. \tag{3.6}$$

If it is assumed that the transmission is non-dispersive, so that the delay can be described by at frequency independent two-way travel time Δt, then (3.4) can be expressed as

$$S_{EE,\omega} = S_{PP,\omega}e^{-i\omega\Delta t}e^{\frac{\Delta t\ln(10)\alpha_\omega}{20\sqrt{\mu_0\varepsilon'_{d,\omega}}}}. \tag{3.7}$$

The relation (3.7), as derived above for loop A, is not sufficiently accurate for loop B. To overcome this problem, the semi-rigid cable for loop B is measured before the loop is formed. Figure 3.6 shows the configuration for the measurement of the semi-rigid cable. The transmission coefficients $S_{12,\omega}$ and $S_{21,\omega}$ are defined as

$$S_{12,\omega} = \left.\frac{V^-_{1,\omega}}{V^+_{2,\omega}}\right|_{V^+_{1,\omega}=0}, \tag{3.8}$$

$$S_{21,\omega} = \left.\frac{V^-_{2,\omega}}{V^+_{1,\omega}}\right|_{V^+_{2,\omega}=0}. \tag{3.9}$$

These transmission coefficients are measured using the network analyzer HP 8753A and the S-parameter test set HP 85046A. Since the coaxial cable is reciprocal the

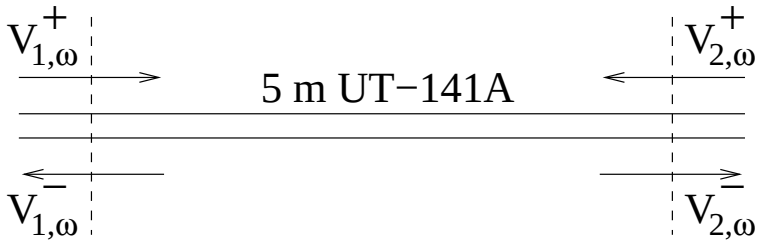

Figure 3.6: Configuration for measurement of the semi-rigid cable UT141-A having a length of 5 m.

transmission coefficients are identical, i.e. $S_{12,\omega} = S_{21,\omega}$. The relation between the reflection coefficients $S_{PP,\omega}$ and $S_{EE,\omega}$ is given by

$$S_{EE,\omega} = S_{PP,\omega}(q_P S_{12,\omega})^2, \tag{3.10}$$

where q_P is a real quantity. This equation is based on a measurement instead of typical values for the coaxial cable as in (3.7). The unknown quantities Δt and q_P in the models of the coaxial cables are estimated in Section 3.2.

3.1.2 Model of the Excitation Cut and the Outer Surface of the Loop Antenna

The model of the coaxial cable is used for the calculation of the reflection coefficient $S_{EE,\omega}$ at the reference plane of the excitation cut. As illustrated in Figure 3.7 the excitation cut, the outer surface of the loop antenna, and the termination in the load are modelled as the coaxial cable connected to a lumped circuit. The semi-rigid cable connected to the load is included using the admittance $Y_c = 20$ mS, and the excitation cut is represented as the admittance $Y_{Cut,\omega}$ with voltage $V_{Cut,\omega}$. The relation between the reflection coefficient $S_{EE,\omega}$ and the admittance $Y_{Cut,\omega}$ is given by the relation

$$Y_{Cut,\omega} = \frac{1 - S_{EE,\omega}}{2S_{EE,\omega}} Y_c. \tag{3.11}$$

The outer conductor of the loop antenna is a perfectly electrically conducting structure. In Figure 3.8 the geometry of the loop antenna is shown. The semi-rigid cable forms an arch with a radius of 17.8 mm in an angle of 310.6^o. The two ends of the semi-rigid cable are connected via two small arches with an inner radius of 7.9 mm, and they are soldered together in such a way that an electrical connection is obtained. The outer conductor is similar for the two loop antennas A and B, except for the fact that the 90^o bending is included in the model of loop B. To calculate the PWRS of the loop antenna, it is desirable to calculate the current distribution.

The current distribution at the loop antenna is calculated for a loop antenna surrounded by a homogeneous medium with free space permeability μ_0 and the complex permittivity $\varepsilon_{ST,\omega_{ST}} = \varepsilon'_{ST,\omega_{ST}} + i\varepsilon''_{ST,\omega_{ST}}$ where $\varepsilon'_{ST,\omega_{ST}}$ and $\varepsilon''_{ST,\omega_{ST}}$ are real quantities. The usual loss tangent $\tan\delta_{ST,\omega_{ST}} = \varepsilon''_{ST,\omega_{ST}}/\varepsilon'_{ST,\omega_{ST}}$ is used. A medium with the relative permittivity $\varepsilon'_{ST}/\varepsilon_0 = 8$ is considered and denoted as a standard (ST) medium. All calculated quantities for the loop antenna surrounded by the standard medium are labelled with the subscribt ST. As shown in Figure 3.9 the excitation cut is modelled as two surfaces that are connected via a wire. A voltage $V_{ST,\omega_{ST}}$ is impressed across the excitation cut by the used of a voltage generator. The current distribution $\mathbf{J}_{ST,\omega_{ST}}$ is calculated using the program Hopes for frequencies in the range from $f_{ST} = 10$ MHz to 4 GHz and loss tangents in the range $\tan\delta_{ST,\omega_{ST}} = 0$ to 1.9. The program Hopes is based on MoM and it is written and designed by Jørgensen [28], [50].

The MoM model is defined as the perfectly electrically conducting surface of the loop antenna with the excitation cut in Figure 3.9 surrounded by a medium with the

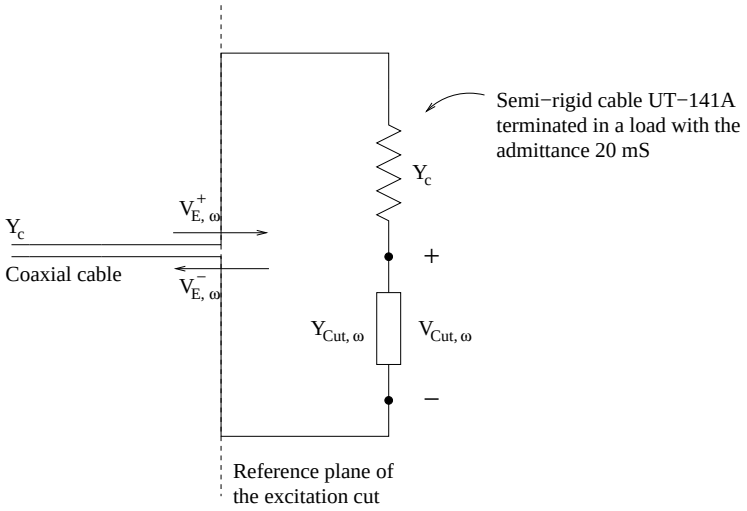

Figure 3.7: The loop antenna modelled as a coaxial cable connected to a lumped circuit. The admittance $Y_{Cut,\omega}$ of the loop antenna is determined from the reflection coefficient $S_{EE,\omega}$. The coaxial cable is also shown in Figure 3.5.

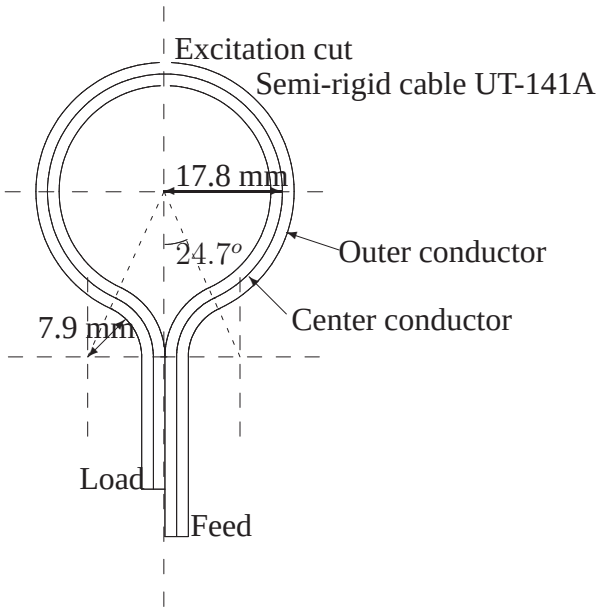

Figure 3.8: Dimensions of the constructed loop antenna.

true constitutive parameters of the soil. The true constitutive parameters are given by the free space permeability μ_0 and the complex permittivity $\varepsilon_{1,\omega} = \varepsilon'_{1,\omega} + i\varepsilon''_{1,\omega}$ where $\varepsilon'_{1,\omega}$ and $\varepsilon''_{1,\omega}$ are real quantities. The usual loss tangent $\tan\delta_{1,\omega} = \varepsilon''_{1,\omega}/\varepsilon'_{1,\omega}$ is used. It follows from Appendix B that if the loss tangents are identical, that is $\tan\delta_{1,\omega} = \tan\delta_{ST,\omega_{ST}}$, then the current distribution $\mathbf{J}_{MoM,\omega}$ of the MoM model is given by

$$\mathbf{J}_{MoM,\omega} = \sqrt{\sqrt{\frac{\varepsilon'_{1,\omega}}{\varepsilon'_{ST,\omega_{ST}}}}}\mathbf{J}_{ST,\omega_{ST}}, \tag{3.12}$$

where the angular frequencies ω and ω_{ST} are related through the scaling

$$\omega_{ST} = \sqrt{\frac{\varepsilon'_{\omega}}{\varepsilon'_{ST,\omega_{ST}}}}\omega. \tag{3.13}$$

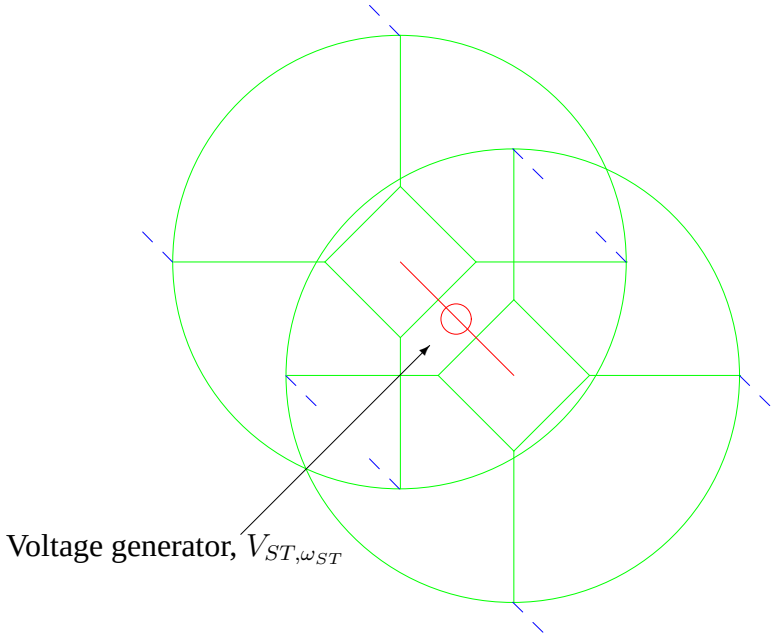

Figure 3.9: The excitation is described using a voltage generator at wire (red). The wire is connected to two perfectly conducting surfaces (green) that form the excitation cut (blue).

Similarly, the voltage $V_{ST,\omega_{ST}}$ of the generator at the wire in Figure 3.9 is related to the voltage $V_{MoM,\omega}$ by the relation

$$V_{MoM,\omega} = \sqrt{\sqrt{\frac{\varepsilon'_{ST,\omega_{ST}}}{\varepsilon'_{\omega}}}} V_{ST,\omega_{ST}}, \tag{3.14}$$

and the relation between the admittances $Y_{MoM,\omega}$ and $Y_{ST,\omega_{ST}}$ is given by

$$Y_{MoM,\omega} = \sqrt{\frac{\varepsilon'_{\omega}}{\varepsilon'_{ST,\omega_{ST}}}} Y_{ST,\omega_{ST}}. \tag{3.15}$$

From the equations (3.13) and (3.15) it is seen that an increased permittivity increases the admittance at the corresponding lower frequencies.

The modelling of the excitation cut is complicated by the random electromagnetic properties of the soil particles close to the excitation cut. To overcome this problem, it is assumed that the electromagnetic field can be considered as quasi-static in a local neighborhood of the excitation cut. This assumption is usable if the dimensions of the excitation cut is much smaller than the wavelength. Herein, the stochastic environment of the excitation cut can be modelled using a shunt capacitance ΔC and a shunt conductance ΔG as shown in Figure 3.10. The admittance $Y_{Cut,\omega}$ of the cut from (3.11) is therefore calculated as

$$Y_{Cut,\omega} = Y_{MoM,\omega} + \Delta G - i\omega\Delta C, \tag{3.16}$$

where is assumed that the shunt capacitance ΔC and shunt conductance ΔG are frequency independent real quantities.

The admittance $Y_{Cut,\omega}$ is now determined in two different ways. The first method is based on a calculation of $S_{EE,\omega}$ using the model of the coaxial cable from the feed to the excitation cut. The reflection coefficient $S_{EE,\omega}$ is then used for the calculation of $Y_{Cut,\omega}$ using (3.11). This admittance is denoted by $Y^I_{Cut,\omega}$. The second method is based on a calculation of the admittance $Y_{MoM,\omega}$ using the MoM method. The

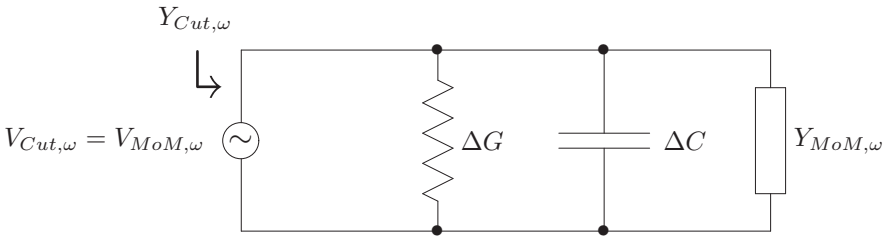

Figure 3.10: Equivalent diagram of the excitation cut. The excitation cut is represented as an admittance $Y_{Cut,\omega}$ in Figure 3.7.

admittance $Y_{Cut,\omega}$ is then calculated using (3.16) above. This admittance is denoted by $Y^{II}_{Cut,\omega}$. An agreement between the calculated admittances $Y^{I}_{Cut,\omega}$ and $Y^{II}_{Cut,\omega}$ indicates that the models are correct.

Using the coordinate system in Figure 2.5 the plane-wave receiving spectrum $\mathbf{R}_{P,\omega}$ for loop A is given by

$$\mathbf{R}_{P,\omega}(k_x,k_y) = -e^{-i\omega\Delta t/2} e^{\frac{1}{2}\frac{\Delta t \alpha_\omega}{\sqrt{\mu_0 \varepsilon'_{d,\omega}}}} \frac{S_{PP,\omega}}{Y_c V_{MoMA,\omega}} \cdot \left(\overline{\mathbf{I}} - \frac{\mathbf{k}^-_{1,\omega}\mathbf{k}^-_{1,\omega}}{k^2_{1,\omega}}\right) \cdot \int\limits_{z'<0} \mathbf{J}_{MoMA,\omega}(\mathbf{r}') e^{-i\mathbf{k}^-_{1,\omega}\cdot\mathbf{r}'} dV', \quad (3.17)$$

where the position of the reference plane is chosen at the feed connector. Similarly, the plane-wave receiving spectrum for loop B is given by

$$\mathbf{R}_{P,\omega}(k_x,k_y) = -\frac{q_P S_{12,\omega} S_{PP,\omega}}{Y_c V_{MoMB,\omega}} \cdot \left(\overline{\mathbf{I}} - \frac{\mathbf{k}^-_{1,\omega}\mathbf{k}^-_{1,\omega}}{k^2_{1,\omega}}\right) \cdot \int\limits_{z'<0} \mathbf{J}_{MoMB,\omega}(\mathbf{r}') e^{-i\mathbf{k}^-_{1,\omega}\cdot\mathbf{r}'} dV'. \quad (3.18)$$

The developed loop antenna models involve various unknown parameters in (3.7), (3.10), (3.17), and (3.18). The unknown parameters are estimated in the following section.

3.2 Methods for Estimation of Model Parameters

The model parameters of the loop antenna are estimated in a two-step procedure. First, a measurement is performed with the loop antenna surrounded by air. In this measurement the parameters of the coaxial cable model are estimated as suggested in Section 3.2.1. Second, the loop antenna is buried in the soil and the constitutive parameter of the soil are estimated using the estimated parameters of the coaxial cable, as explained in Section 3.2.2.

3.2.1 Method Based on Measurements with the Loop Antenna in Air

The parameters Δt and q_P in the model of the coaxial cable are independent of the medium surrounding the loop antenna. It should be recalled from Section 3.1.1 that Δt and q_P are model parameters for loop A and B, respectively. These model parameters are estimated by minimizing the amplitude of the difference between admittances $Y^{I}_{Cut,\omega}$ and $Y^{II}_{Cut,\omega}$. Measurements for a loop antenna surrounded by air are considered so that the constitutive parameters for the surroundings are known to be the

free space parameters μ_0 and ε_0. Herein, the admittance $Y_{MoM,\omega}$ can be calculated and only the shunt admittance ΔG and shunt capacitance ΔC are unknown in (3.16). These parameters must be estimated together with the parameters in the cable model. However, ΔG and ΔC can not be used when the loop antenna is buried in the soil due to the dependence of the constitive parameters of the soil. The error function for estimation of the parameters in the cable model is given by

$$\varsigma = \int_{\omega_{min}}^{\omega_{max}} \frac{|\,\mathrm{Re}(Y^I_{Cut,\omega} - Y^{II}_{Cut,\omega})|}{\mathrm{Re}Y^I_{Cut,\omega}} d\omega, \tag{3.19}$$

where a frequency range from $f = 0.45$ GHz to $f = 3$ GHz is used. The upper frequency is limited by the network analyzer and the S-parameter test set and the lower frequency is limited by inaccuracies of the model of the loop antenna. Only the real part of the admittances $Y^I_{Cut,\omega}$ and $Y^{II}_{Cut,\omega}$ are considered in this error function. The imaginary parts of $Y^I_{Cut,\omega}$ and $Y^{II}_{Cut,\omega}$ must agree over the considered range of frequencies if the cable model is correct and the right values for the model parameter are estimated. The model parameter for the coaxial cable will be used for estimation of the complex permittivity in Section 3.2.2.

3.2.2 Method Based on Measurements with the Loop Antenna in Soil

The complex permittivity of the soil is considered as a model parameter that is used in the calculation of the plane-wave receiving spectrum in (3.17) and (3.18) for loop A and B, respectively.

The complex permittivity of the soil depends on the moisture content. Hence, changes of the soil moisture content in time and space will change the measurement facility for GPR antenna. In this thesis it is assumed that the soil can be considered as homogeneous in a local neighbourhood of the loop antenna. Furthermore, it is assumed that the soil moisture is constant over the time interval where the measurements are performed. Methods for estimation of the complex permittivity of the soil close to the loop antenna during the are suggested. These methods are valid only if it is assumed that multiple interactions between the loop antenna and the air-soil interface can be neglected.

A tutorial to methods for measurements of the complex permittivity is given by Afsar et al. in [51] and some of these methods have appeared to be useful for measurements of the complex permittivity for soil. A classical method for measurement of the complex permittivity is the transmission line methods as suggested by Scott in [52], in which reflection measurements of a coaxial transmission line with one open end are measured. Heimovaara suggested a similar method in [53] where the coaxial transmission line is emulated using seven wires and the complex permittivity is measured for frequencies up to 1.5 GHz. The plate capacitor, as suggested by Fano and Trainotti in [54], is also a classical method. Knowledge of the soil moisture is used for critical crop decisions in agriculture. Since the complex permittivity is very

sensitive to the soil moisture several measurement techniques are based on an estimation of the complex permittivity. As an example Herrick in [55] suggests a method for measurement of the soil moisture by measuring the self and mutual admittances of a buried vertical slotted cylinder array.

In [11] and [10] non-invasive methods are suggested and experimentally verified. Wakita et al. [11] found that the permittivity can be estimated by use of the measured admittance of a dipole antenna at the air-soil interface. Wakita suggests that the resonant frequency and resonant resistance of a dipole antenna is used. In [10] an array of Vivaldi antennas is used for the acquisition of common-midpoint data. The common-midpoint (CMP) data are used for construction of a velocity spectrum, and the velocity of the medium is estimated.

The method using loop A buried in the soil is based on measurements of the reflection coefficient $S_{PP,\omega}$. In Figure 3.11 the measurement configuration with a type A loop buried in the soil is shown. The distance between the excitation cut and the air-soil interface is denoted by d_P. The reference plane for the loop antenna is chosen in the coaxial cable, and the voltages of the incoming and outgoing waves at the reference plane are denoted by $V^+_{P,\omega}$ and $V^-_{P,\omega}$, respectively. The complex permittivity $\varepsilon_{1,\omega}$ of the soil close to the loop antenna is estimated from the measured reflection coefficient $S_{PP,\omega}$ using the error function from (3.19). The estimation is performed by calculating the admittance $Y_{Cut,\omega}$ of the loop antenna from the reflection coefficient $S_{PP,\omega}$. To obtain one well-defined global minimum for the error function it is assumed that the real part of the complex permittivity is independent of the frequency

$$\varepsilon'_1 = \text{Re}(\varepsilon_{1,\omega}) \tag{3.20}$$

and the imaginary part can be written in terms of the frequency independent conductivity σ_1 as

$$\varepsilon''_{1,\omega} = \frac{\sigma_1}{\omega}. \tag{3.21}$$

The shunt admittance ΔG, the permittivity ε'_1, and the conductivity σ_1 are estimated on the basis of (3.19). The used range of frequency range is given by the inequality

$$0.7 < \frac{1}{C_P\sqrt{\mu_0\varepsilon'_s}f} < 8, \tag{3.22}$$

where $C_P = 107$ mm is the circumference of the loop antenna. Another method for estimation of the complex permittivity is based on a measurement of the voltage transfer function between a loop antenna B buried in the soil and a loop antenna A above the air-soil interface. Besides from the fact that one of the probes is buried in the medium for which the complex permittivity is unknown, this procedure is very similar to the free-space methods described by Afsar [51]. In Figure 3.12 the loop antenna of type B is buried in the soil and the incoming and outgoing waves at the reference plane are denoted by $V^+_{P,\omega}$ and $V^-_{P,\omega}$, respectively. A loop antenna of type A is positioned above the air-soil interface, and the incoming and outgoing waves at

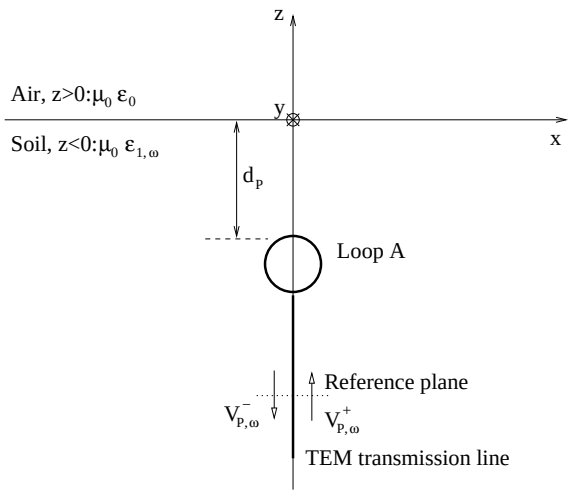

Figure 3.11: Measurement configuration for estimation of the constitutive parameters using the reflection coefficient of the type A loop antenna in the soil.

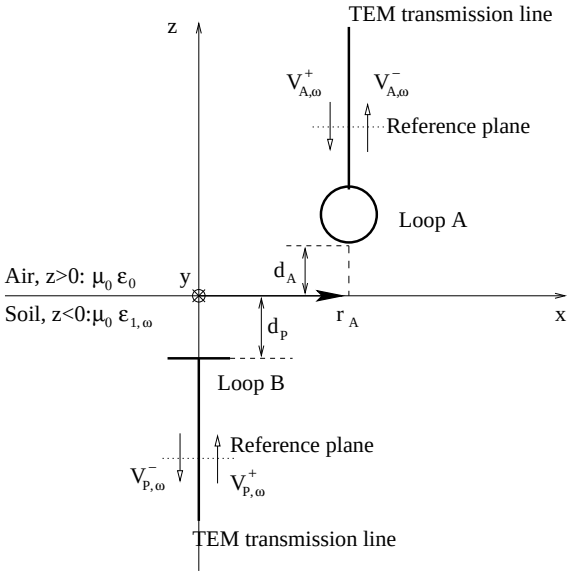

Figure 3.12: Measurement configuration for measurement of constitutive parameters using the voltage transfer function between the type B loop antenna in the soil and the type A loop antenna in the air.

the reference plane are denoted by $V^{+}_{A,\omega}$ and $V^{-}_{A,\omega}$, respectively. The excitation cut of loop A is positioned at the distance d_A from the air-soil interface and the reference point of the loop antenna is denoted by $\mathbf{r}_A$. The complex permittivity is estimated by using the voltage transfer function

$$S_{PA,\omega}(\mathbf{r}_A) = \left.\frac{V^{-}_{P,\omega}(\mathbf{r}_A)}{V^{+}_{A,\omega}(\mathbf{r}_A)}\right|_{V^{+}_{P,\omega}(\mathbf{r}_A)=0}. \tag{3.23}$$

This is done by measuring the voltage transfer function and comparing the measured voltage transfer function with a calculated voltage transfer function. The voltage transfer function can be calculated from the plane-wave receiving spectrum of the loop antenna in the soil and the plane-wave transmitting spectrum of the loop antenna in the air above the interface. The plane-wave receiving spectrum of the loop antenna in the soil is written as in (3.18) and the plane-wave transmitting spectrum of the the loop in the air is given by [22]

$$\begin{aligned}\mathbf{T}_{A,\omega}(k_x,k_y) = -e^{-i\omega\Delta t/2}e^{\frac{1}{2}\frac{\Delta t\alpha_\omega}{\sqrt{\mu_0\varepsilon'_{d,\omega}}}}\frac{\omega\mu_0 S_{PP,\omega}}{V_{MoMA,\omega}} \\ \cdot\,\overline{\mathbf{F}}_\omega(k_x,k_y)\cdot\int\limits_{z'<0}\mathbf{J}_{MoMA,\omega}(\mathbf{r}')e^{-i\mathbf{k}^{-}_{0,\omega}\cdot\mathbf{r}'}dV',\end{aligned} \tag{3.24}$$

where the dyad $\overline{\mathbf{F}}_\omega$ is defined as

$$\begin{aligned}\overline{\mathbf{F}}_\omega(k_x,k_y) = \frac{2}{(\gamma_{0,\omega}+\gamma_{1,\omega})(k_x^2+k_y^2+\gamma_{0,\omega}\gamma_{1,\omega})} \\ \cdot\left[\hat{\mathbf{x}}((k_y^2+\gamma_{0,\omega}\gamma_{1,\omega})\hat{\mathbf{x}}-k_xk_y\hat{\mathbf{y}}+k_x\gamma_{1,\omega}\hat{\mathbf{z}})\right. \\ +\hat{\mathbf{y}}(-k_xk_y\hat{\mathbf{x}}+(k_x^2+\gamma_{0,\omega}\gamma_{1,\omega})\hat{\mathbf{y}}+k_y\gamma_{1,\omega}\hat{\mathbf{z}}) \\ \left.+\hat{\mathbf{z}}(k_x\gamma_{0,\omega}\hat{\mathbf{x}}+k_y\gamma_0\hat{\mathbf{y}}+(k_x^2+k_y^2)\hat{\mathbf{z}})\right].\end{aligned} \tag{3.25}$$

The voltage transfer function $S_{PA,\omega}$ between the antennas is found from the expression

$$S_{PA,calc,\omega} = \frac{1}{2\pi}\iint_{-\infty}^{\infty}\mathbf{R}_{P,\omega}(k_x,k_y)\cdot\mathbf{T}_{A,\omega}(k_x,k_y)dk_xdk_y, \tag{3.26}$$

where the position of the loop antenna in the air is assumed to be $\mathbf{r}_A = \mathbf{0}$. The complex permittivity of the soil is determined using an iterative algorithm. The algorithm is started by setting the imaginary part $\varepsilon''_{1,\omega}$ of the complex permittivity at zero and the real part $\varepsilon'_{1,\omega}$ is estimated by minimizing the error function given by

$$\varsigma_{phase} = \left|\angle\left(\frac{S_{PA,\omega}}{S_{PA,calc,\omega}}\right)\right|, \tag{3.27}$$

over a frequency range from the minimum frequency 0.2 GHz to the maximum frequency 3 GHz. Several minima can occur for each frequency. To select the right

minimum, the error function must be calculated from low frequencies to high frequencies. At low frequencies only one minimum will appear for a reasonable range of permittivity $\varepsilon'_{1,\omega}$. This minimum is used for the determination of the permittivity at higher frequencies in such a way that the error function is minimized over the considered range of frequencies.

The imaginary part $\varepsilon''_{1,\omega}$ of the complex permittivity is expressed in terms of a frequency dependent conductivity given by $\sigma_{1,\omega} = \varepsilon''_{1,\omega}\omega$. It is assumed that the difference in the amplitudes $S_{PA,\omega}$ and $S_{PA,calc,\omega}$ are due to conductivity $\sigma_{1,\omega}$ in the soil which can be expressed using the approximately equation

$$|S_{PA,\omega}| = |S_{PA,calc,\omega}|\, e^{-\frac{\sigma_{1,\omega}}{2}\sqrt{\frac{\mu_0}{\varepsilon'_{1,\omega}}}d_P}. \tag{3.28}$$

Subsequently, this conductivity $\sigma_{1,\omega}$ is calculated as

$$\sigma_{1,\omega} = -\frac{1}{10 d_P \log_{10}(e)}\sqrt{\frac{\varepsilon'_{1,\omega}}{\mu_0}}\, 20\log_{10}\left|\frac{S_{PA,\omega}}{S_{PA,calc,\omega}}\right|. \tag{3.29}$$

Using the calculated conductivities $\sigma_{1,\omega}$ the error function for the phase in (3.19) can be recalculated and a new set of permittivities can be calculated. This procedure is continued until a perfect match between $S_{PA,\omega}$ and $S_{PA,calc,\omega}$ is obtained with respect to phase and amplitude. The advantage of the method using loop B is that knowledge about the frequency dependence of the complex permittivity is not necessary in order to perform an estimation.

3.3 Use and Verification of the Models

In the previous sections models for the probes and the surrounding soil have been developed, and methods for estimation of the model parameters have been suggested. However, the following two questions remain to be answered. First, do the models constitute an accurate description of the physics they are meant to describe? Second, what is the uncertainty of the estimated model parameters? In order to answer these questions, the measurement results are discussed in the following two sections.

3.3.1 Estimated Parameters using Measurements with the Loop Antenna in Air

The admittances of the loop antennas surrounded by air are used for estimation of the model parameters of the coaxial cable and for verification.

Considering loop A the two-way travel time $\Delta t = 2.895$ ns is estimated by comparing the real part of the admittances $\mathrm{Re}Y^{I}_{Cut,\omega}$ and $\mathrm{Re}Y^{II}_{Cut,\omega}$ where the shunt admittance is estimated to $\Delta G = 0.3$ mS. In the right plot of Figure 3.13 the real part of the admittances are plotted as a function of the frequency. The figure shows perfect agreement between the real part of the admittances $\mathrm{Re}Y^{I}_{Cut,\omega}$ and $\mathrm{Re}Y^{II}_{Cut,\omega}$ over the

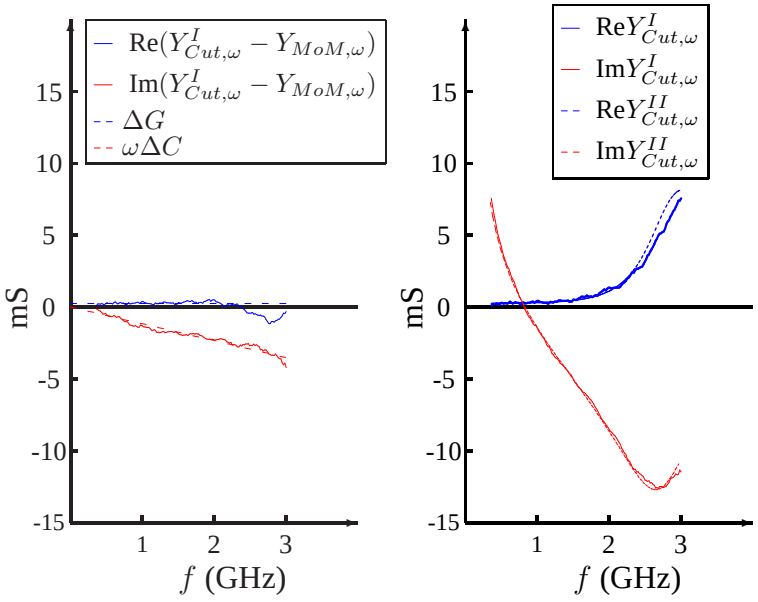

Figure 3.13: Admittances for loop A in air. The admittance $Y^I_{Cut,\omega}$ is calculated using the measured reflection coefficient $S_{PP,\omega}$ and the two-way travel time Δt. The admittance $Y_{MoM,\omega}$ is calculated using MoM.

considered frequency range. The left plot shows the difference $\text{Im}(Y^I_{Cut,\omega} - Y_{MoM,\omega})$ as a function of the frequency, and the expected linear dependence is observed. The shunt capacitance is estimated to $\Delta C = 0.19$ pF using the slope of the line. Hence, the model of the loop antenna is verified for the measurement where the loop antenna is surrounded by air. Furthermore, the two-way travel time is estimated.

The model parameter q_P for loop B is estimated using the same procedure. In Figure 3.14 the admittances $Y^I_{Cut,\omega}$ and $Y^{II}_{Cut,\omega}$ are plotted as a function of the frequency and it is seen that agreement between the admittances is obtained.

3.3.2 Estimated Parameters using Measurements with the Loop Antenna in Soil

The complex permittivity of the soil surrounding the loop antenna is considered as a the model parameter, and in this section it is estimated using the methods developed in Section 3.2.2.

A loop antenna of type A is buried at a distance of 12.5 cm from the air-soil interface in dry loam. It is assumed that for dry loam the real parts of the permittivity $\varepsilon'_{1,\omega}/\varepsilon_0$ is independent of the frequency and that the imaginary part is given by $\varepsilon''_{1,\omega} = \sigma_1/\omega$ where σ_1 is independent of the frequency. The method for estimation of the complex permittivity is based on the error function defined in (3.19) where the real parts of the admittances $Y^I_{Cut,\omega}$ and $Y_{MoM,\omega}$ are compared. The admittance

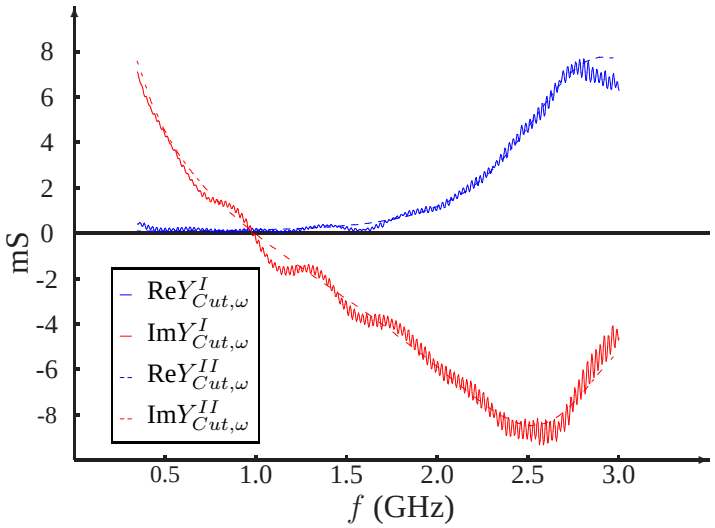

Figure 3.14: Admittances for loop B in air. The admittance $Y^I_{Cut,\omega}$ is calculated using the measured reflection coefficient $S_{PP,\omega}$ and the parameter q_P. The admittance $Y_{MoM,\omega}$ is calculated using MoM.

is calculated using the estimated two-way travel time Δt from Section 3.3.1 and the measured reflection coefficient $S_{PP,\omega}$. The admittance $Y_{MoM,\omega}$ is calculated using the real part of the complex permittivity $\varepsilon'_1/\varepsilon_0 = 3.5$ and the conductivity $\sigma_1 = 24$ mS/m using MoM. In Figure 3.15 the admittances $Y^I_{Cut,\omega}$ and $Y^{II}_{Cut,\omega}$ are plotted as a function of the frequency and perfect agreement is observed. The agreement in both the real and imaginary part of the admittances constitutes a verification of the model in this particular case where dry loam is measured.

Measurements of media with known constitutive parameters are performed by Lenler-Eriksen in [30]. In this paper the complex permittivity of water with a solution of sodiumchloride is estimated at the temperature $T = 25^o$C in the frequency range from $f = 0.05$ GHz to 0.45 GHz. Low frequencies are used, as dictated in (3.22), due to the high permittivity of water, $\varepsilon'_1/\varepsilon_0 = 78.54$. The Debye effect causes frequency dependent fluctuations in the real part of the complex permittivity $\varepsilon'_{1,\omega}$ and the conductivity $\sigma_{1,\omega}$, as described in [56]. Due to the low frequencies these fluctuations are negligible and the method is therefore usable. The estimated permittivity and conductivity are compared to the expected values found in [57, pp. D-105 and E-43]. The errors are less than 7% for the permittivity and less than 5% for the conductivity.

The method involving loop antenna B is used for measurement of moist loam from Zealand that is believed to have a more complicated frequency dependence of the complex permittivity. In Figure 3.16 the error function ς_{phase} from (3.27) is plotted as function of frequency and the relative permittivity $\varepsilon'_{1,\omega}/\varepsilon_0$. Below the relative permittivity $\varepsilon'_{1,\omega}/\varepsilon_0 = 7.5$ the curves have a positive slope and above $\varepsilon'_{1,\omega}/\varepsilon_0 = 7.5$ the curve has a negative slope. Seven local minima appear at the frequency 3 GHz and

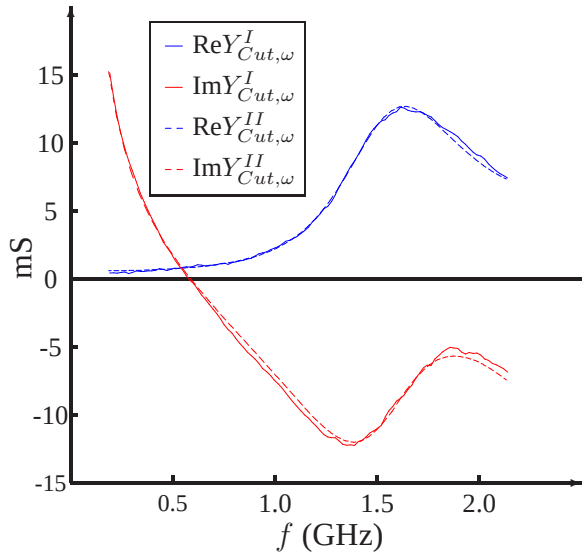

Figure 3.15: Admittances for loop A in dry soil. The admittance $Y^I_{Cut,\omega}$ is calculated using the measured reflection coefficient $S_{PP,\omega}$ and the two-way travel time Δt. The admittance $Y_{MoM,\omega}$ is calculated using the real part of the complex permittivity $\varepsilon'_1/\varepsilon_0 = 3.5$ and the conductivity $\sigma = 24$ mS/m using MoM.

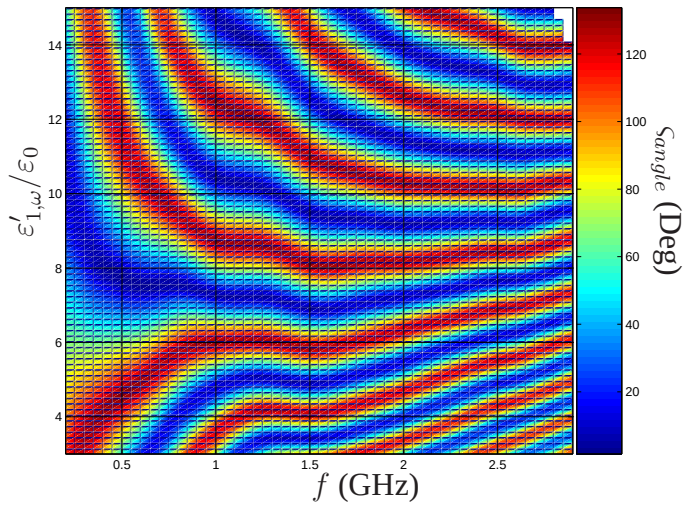

Figure 3.16: The error function ς_{phase} as defined in (3.27).

only one local minimum appears at the frequency 0.3 GHz for relative permittivities in the range from $\varepsilon'_{1,\omega}/\varepsilon_0 = 3$ to 15. Since it is expected that the relative permittivity of the moist loam is in the range from $\varepsilon'_{1,\omega}/\varepsilon_0 = 3$ to 15 at 0.3 GHz only the curve intersecting this range is reasonable. Subsequently, the conductivity is calculated using (3.29) and the procedure is repeated until agreement between the measured transfer function $S_{PA,\omega}$ and the calculated transfer function $S_{PA,calc,\omega}$ is obtained. These transfer functions are plotted as a function of the frequency in Figure 3.17, and an excellent agreement between the two transfer functions is obtained in the frequency band from 0.3 GHz to 3 GHz.

In Figure 3.18 the estimated relative permittivity $\varepsilon'_{1,\omega}/\varepsilon_0$ and the conductivity $\sigma_{1,\omega}$ are plotted as a function of frequency. In the left plot the black dots are the estimated relative permittivities. It is seen that the permittivity can be considered as constant above 0.5 GHz. Below 0.5 GHz, the permittivity fluctuates randomly and the interpretations should be done with caution. During the measurements of the plane-wave transmitting spectra the relative permittivity is considered as being equal to the average value $\varepsilon'_{1,\omega}/\varepsilon_0 = 7.80$ that is plotted as a blue dashed line in Figure 3.18.

In the right plot the black dots represent the estimated conductivity $\sigma_{1,\omega}$. It is seen that the conductivity can be considered as proportional to the frequency, $\sigma_{1,\omega} = a_c f$. Using the method of least squares, the slope is estimated to $a_c = 51$ mS/m/GHz. The line $\sigma_{1,\omega} = a_c f$ is plotted as a blue dashed line. This result is used to assume that the conductivity is proportional to the frequency with proportionality constant $a_c = 51$ mS/m/GHz.

The estimated complex permittivity is compared with calculated values using a model of the soil. Several models of the complex permittivity of soil have been suggested over the last decades [58]- [66]. Dobson et al. suggest a volumetric mixing model in [64] in which the complex permittivity is written as

$$(\varepsilon_{1,\omega})^{\alpha} = \sum_n W_n \, (\varepsilon_{n,\omega})^{\alpha} \tag{3.30}$$

where W_n is the volumetric fraction of the soil component n with the complex permittivity $\varepsilon_{n,\omega}$, and α is a constant. Mironov et al. have suggested a four-component model of the soil in [58], [7], and [59], where the constant in (3.30) is set to $\alpha = 0.5$. The four associated soil components n are given by

- Air, $n = a$.
- Soil particle, $n = p$.
- Bounded water, $n = b$.
- Unbounded water, $n = u$.

The volume of the soil is denoted by V_{total} and the volumes of the air, soil particles, bounded water, and unbounded water are called V_a, V_p, V_b, and V_u, respectively. The soil volume then equals

$$V_{total} = V_a + V_p + V_b + V_u. \tag{3.31}$$

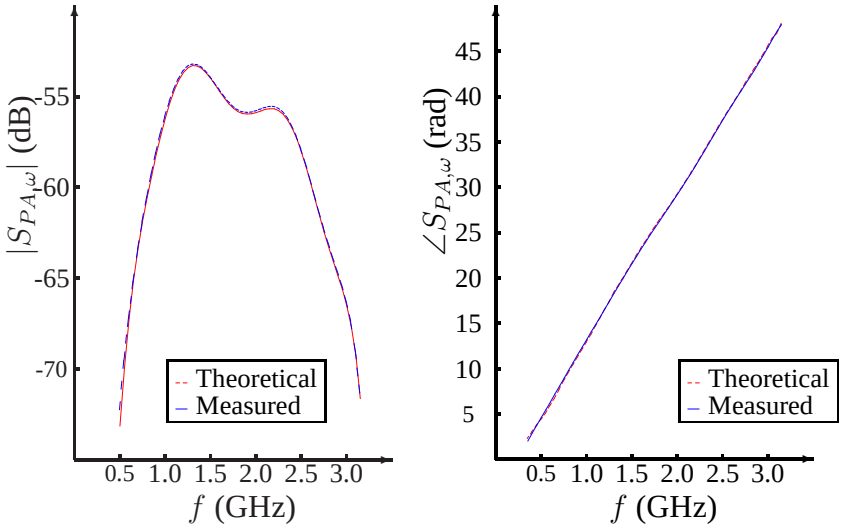

Figure 3.17: Comparison of the measured and theoretical voltage transfer function $S_{PA,\omega}$.

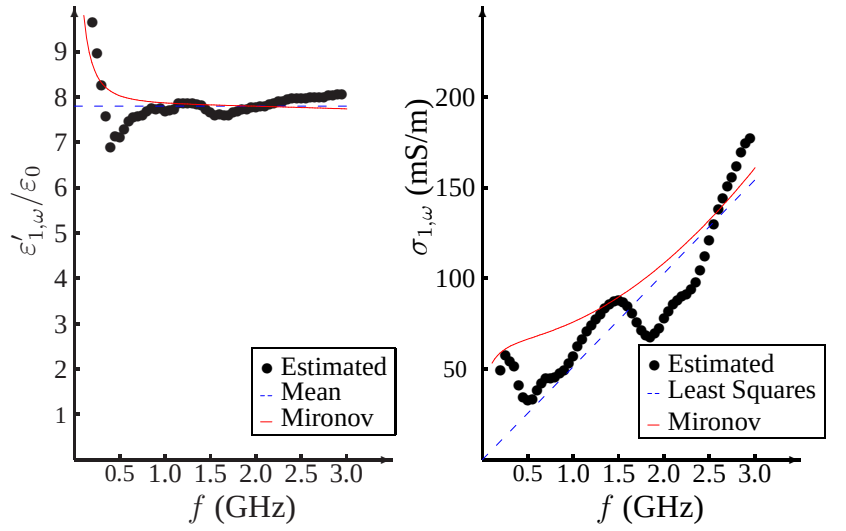

Figure 3.18: Estimated complex permittivity and calculated complex permittivity using the Mironov model.

The volumetric fractions are given by

$$W_a = \frac{V_a}{V_{total}}, \tag{3.32}$$

$$W_p = \frac{V_p}{V_{total}}, \tag{3.33}$$

$$W_b = \frac{V_b}{V_{total}}, \tag{3.34}$$

$$W_u = \frac{V_u}{V_{total}}, \tag{3.35}$$

and the volumetric fraction of water is denoted by W and expressed as

$$W = \frac{V_b + V_u}{V_{total}}. \tag{3.36}$$

The maximum volumetric fraction of bounded water is denoted by W_t and the volume of the bounded water V_b is given by

$$V_b = \begin{cases} WV_{total} & ,W \leq W_t, \\ W_t V_{total} & ,W > W_t, \end{cases} \tag{3.37}$$

and the volume of the unbounded water is given by

$$V_u = \begin{cases} 0 & ,W \leq W_t, \\ (W - W_t)V_{total} & ,W > W_t. \end{cases} \tag{3.38}$$

The expression for the complex permittivity of the soil in (3.30) can be rewritten as

$$\sqrt{\varepsilon_{1,\omega}} = W_a + W_p\sqrt{\varepsilon_{p,\omega}} + W_b\sqrt{\varepsilon_{b,\omega}} + W_u\sqrt{\varepsilon_{u,\omega}}. \tag{3.39}$$

If the complex permittivity $\varepsilon_{ds,\omega}$ for dry soil is introduced and if the expression for the total volume in (3.31) is used, then (3.39) can be rewritten as

$$\sqrt{\varepsilon_{1,\omega}} = \sqrt{\varepsilon_{ds,\omega}} + \left(\sqrt{\varepsilon_{b,\omega}} - \sqrt{\varepsilon_0}\right) W_b + \left(\sqrt{\varepsilon_{u,\omega}} - \sqrt{\varepsilon_0}\right) W_u \tag{3.40}$$

where the complex permittivity for dry soil is expressed as

$$\sqrt{\varepsilon_{ds,\omega}} = \sqrt{\varepsilon_0} + \left(\sqrt{\varepsilon_{p,\omega}} - \sqrt{\varepsilon_0}\right) W_p. \tag{3.41}$$

The complex permittivity of water is described using the Debye model as [59]

$$\varepsilon'_{b,\omega} = \varepsilon_{b,\infty} + \frac{\varepsilon_{b,0} - \varepsilon_{b,\infty}}{1 + \omega^2\tau_b^2}, \tag{3.42}$$

$$\varepsilon''_{b,\omega} = \frac{\omega\tau_b(\varepsilon_{b,0} - \varepsilon_{b,\infty})}{1 + \omega^2\tau_b^2} + \frac{\sigma_b}{\varepsilon_0\omega}, \tag{3.43}$$

$$\varepsilon'_{u,\omega} = \varepsilon_{u,\infty} + \frac{\varepsilon_{u,0} - \varepsilon_{u,\infty}}{1 + \omega^2\tau_u^2}, \tag{3.44}$$

$$\varepsilon''_{u,\omega} = \frac{\omega\tau_u(\varepsilon_{u,0} - \varepsilon_{u,\infty})}{1 + \omega^2\tau_u^2} + \frac{\sigma_u}{\varepsilon_0\omega}, \tag{3.45}$$

	Used parameters for loam from Zealand in Denmark	Estimated parameter for silty clay in [7]
$\varepsilon'_{d,\omega}/\varepsilon_0$	3	3.12
$\varepsilon''_{d,\omega}/\varepsilon_0$	0	0.000
$\varepsilon_{b,\infty}/\varepsilon_0$	5	4.9
$\varepsilon_{b,0}/\varepsilon_0$	50	41.42
σ_b (S/m)	1	1.16
τ_b (ps)	10	12.09
$\varepsilon_{u,\infty}/\varepsilon_0$	5	4.9
$\varepsilon_{u,0}/\varepsilon_0$	100	96.80
σ_u (S/m)	1	1.59
τ_u (ps)	10	9.77
W_t	0.16	0.157
W	0.17	-

Table 3.2: Parameters in the dielectric mixing model for soil. The left column contains the chosen parameters for calculation of the complex permittivity in Figure 3.18. The right column contains parameters for silty clay from [7].

The parameters τ_b and τ_u are denoted as the relaxation times for bounded and free water, respectively. The parameters $\varepsilon_{b,0}$ and $\varepsilon_{u,0}$ are the permittivities at zero frequency and the parameters $\varepsilon_{b,\infty}$ and $\varepsilon_{u,\infty}$ are the relative permittivities at an infinitely high frequency as well. The permittivities at zero frequency and the relaxation times depend on the temperature, so that the complex permittivity depends on the temperature. This temperature dependence is described for pure water in [67].

The complex permittivity is calculated using the dielectric mixing model in (3.40) as suggested by Mironov et al.. The calculated relative permittivity $\varepsilon'_{1,\omega}/\varepsilon_0$ and the conductivity $\sigma_{1,\omega}$ are plotted as the red curves in Figure 3.18 on page 42, and the used parameters in the model are specified in the left column of Table 3.2. The model also predicts a constant real part of the complex permittivity and a conductivity that is approximately proportional to the frequency. The used parameter in the model is similar to parameters used by Mironov et al. in [7] for silty clay so it is concluded that the estimated complex permittivity is typical for loam.

3.3.3 Uncertainties of the Measured Complex Permittivities

The estimation of the complex permittivity of soil is complicated by the fact that the complex permittivity fluctuates in space and time. This is mainly due to the high dependence of the complex permittivity on the moisture content, temperature, and the compression of the soil. However, if the soil is homogeneous there will still be a number of factors that can result in additional uncertainties:

- Convergence problems due to multiple global minima in the error functions. This problem is discussed on page 34 for the method using loop A and the error

function in (3.19). It appeared that it is possible to overcome this problem for dry soil as suggested by Lenler-Eriksen et al. in [29].

- Errors due to the modelling of the loop as a perfectly electrically conducting structure. During the measurement of water using the method for loop A, as suggested by Lenler-Eriksen and Meincke in [30], it appeared that a layer of paint could change the admittance of the loop significantly and give erroneous results.

- Errors in the geometrical model of the loop antenna and convergence problems using the MoM can give erroneous results.

- Errors in the model of the feeding network of the loop. Reflections at the SMA connectors can give ripples in the estimated admittances of the loop antennas.

- Errors in the measurements using the network analyzer HP 8753A and the S-parameter test set HP 85046A. These errors will be discussed in the following section.

Equations, as suggested in the HP manual in [68] for calculation of the uncertainties of the measured S-parameters, are given in Appendix C. The following calculations are based on typical values for the measurement configuration of the network analyzer HP 8753A and the S-parameter test set HP 85046A, as written in Table C.3. These typical values in [68] are specified for a measurement configuration where an IF bandwidth of 10 Hz is applied. All the measurements in this thesis are performed using an IF bandwidth of 30 kHz so the following calculations are only intended as a guide. In [68] and Appendix C the total reflection phase uncertainty and total transmission phase uncertainty are denoted by E_{rp} and E_{tp}, respectively. The total relative amplitude reflection uncertainty and the total relative amplitude transmission uncertainty are denoted by E_{rm} and E_{tm}, respectively.

These uncertainties depend on the measured reflection and transmission coefficients. As a typical configuration, loop antenna A surrounded by a medium with the permittivity $\varepsilon'_{1,\omega}/\varepsilon_0 = 8$ and a conductivity $\sigma_{1,\omega} = 50$ mS/m is considered. The reflection coefficient $S_{PP,\omega}$ and the uncertainties E_{rp} and E_{rm} are calculated. In Figure 3.19 the uncertainty of the amplitude E_{rm} is plotted as a function of frequency. The uncertainty of the amplitude varies between 2.5% and 4.0% over the frequency range from 0.4 GHz to 3 GHz. In Figure 3.20 the uncertainty of the phase E_{rp} is plotted as a function of frequency. The uncertainty of the phase is increasing linearly from 3^o at 0.4 GHz to 11^o at 3 GHz. These uncertainties are considered as acceptable.

The measured transmission coefficients, as plotted in 3.17 are now used for calculation of the uncertainties of the measured transmission coefficient. If it is assumed that the estimated conductivity is approximately given by the relation

$$e^{-\frac{\sigma_{1,\omega} d_P}{2}\sqrt{\frac{\mu_0}{\varepsilon_{1,\omega}}}} = q|S_{PA,\omega}|, \tag{3.46}$$

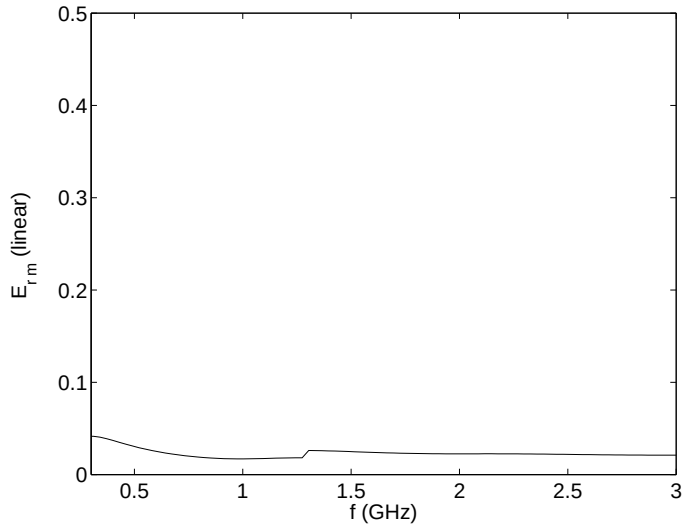

Figure 3.19: Uncertainty of the measured amplitude of S_{11}. Reflection coefficients of a loop antenna surrounded by a medium with the permittivity $\varepsilon'_{1,\omega}/\varepsilon_0 = 8$ and a conductivity $\sigma_{1,\omega} = 50$ mS/m are considered.

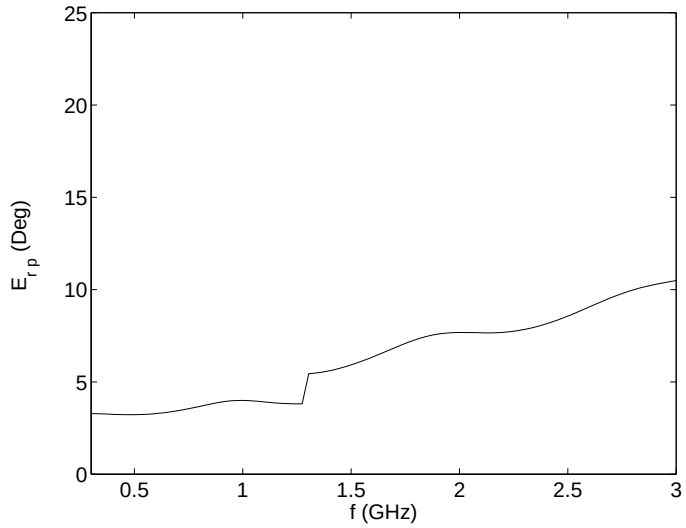

Figure 3.20: Uncertainty of the measured phase of S_{11}. Reflection coefficients of a loop antenna surrounded by a medium with the permittivity $\varepsilon'_{1,\omega}/\varepsilon_0 = 8$ and a conductivity $\sigma_{1,\omega} = 50$ mS/m are considered.

where q is a constant, then the uncertainty of the amplitude of the transmission coefficient $S_{PA,\omega}$ can be used for a calculation of the uncertainty of the conductivity $\sigma_{1,\omega}$ by use of the equation

$$\Delta\sigma_{1,\omega} = -\frac{2}{d_P}\sqrt{\frac{\varepsilon'_{1,\omega}}{\mu_0}}\frac{E_{tm}}{20\log_{10}(e)} \tag{3.47}$$

where the uncertainty E_{tm} is in dB. Similarly, if it is assumed that the estimated permittivity $\varepsilon'_{1,\omega}$ is approximately given by the relation

$$e^{i\omega\sqrt{\mu_0\varepsilon'_{1,\omega}}d_P} = e^{i(\phi_0+\angle S_{PA,\omega})}, \tag{3.48}$$

where ϕ_0 is a constant phase, then the uncertainty of the phase of the transmission coefficient $S_{PA,\omega}$ can be used for a calculation of the uncertainty of the permittivity $\varepsilon_{1,\omega}$ by use of the equation

$$\Delta\varepsilon_{1,\omega} = \frac{2E_{tp}}{\omega d_P}\sqrt{\frac{\varepsilon_{1,\omega}}{\mu_0}}, \tag{3.49}$$

where E_{tp} is the uncertainty of the phase. The uncertainties $\Delta\sigma_{1,\omega}$ and $\Delta\varepsilon_{1,\omega}$ are plotted as a function of frequency in Figures 3.21 and 3.22, respectively. In Figure 3.21 it is seen that $\Delta\sigma_{1,\omega}$ is less than 40 mS/m over the frequency range from 0.4 GHz to 3 GHz, and between 1 GHz and 2 GHz the uncertainty is less than 10 mS/m. From Figure 3.22 it is seen that $\Delta\varepsilon_{1,\omega}$ is less than 0.5 above 0.5 GHz. The uncertainties due to the network analyzer HP 8753A are therefore considered as acceptable for measurements of moist loam.

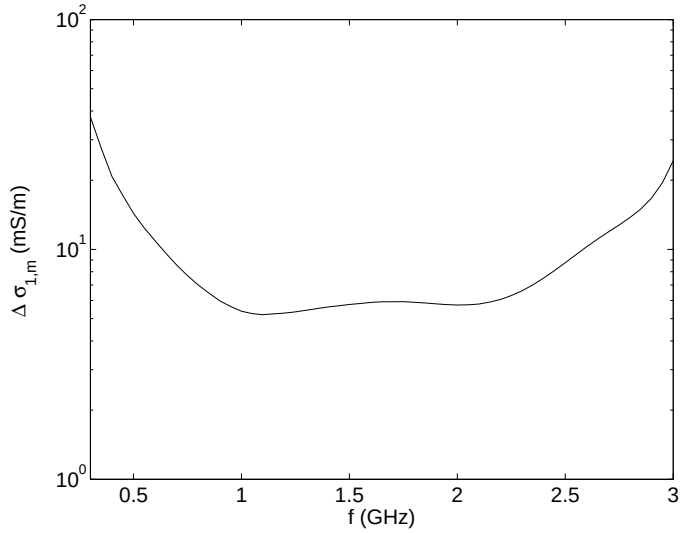

Figure 3.21: Uncertainty in the estimated conductivity of the soil due the uncertainties in the measurements using the network analyzer HP 8753A and the S-parameter test set HP 85046A.

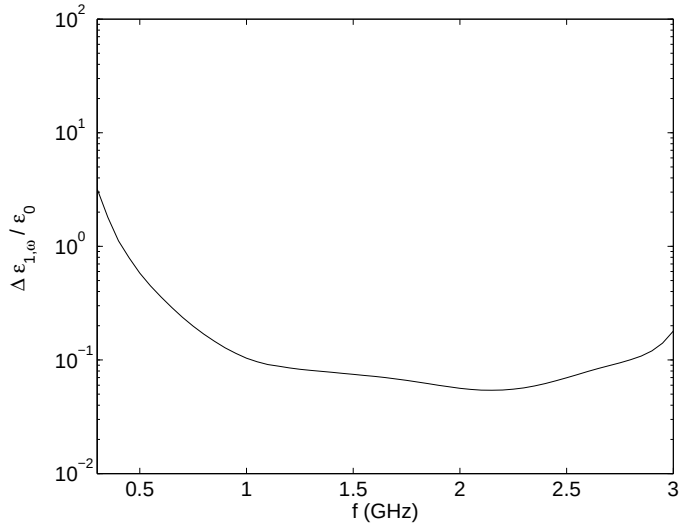

Figure 3.22: Uncertainty in the estimated permittivity of the soil due the uncertainties in the measurements using the network analyzer HP 8753A and the S-parameter test set HP 85046A.

3.4 Summary

Loop antennas are chosen as probes for measurements of GPR antennas and models for probe correction are developed. The models are divided into two submodels. The first submodel describes the coaxial cable from the feed connector to the excitation cut of the loop antenna, and the second submodel describes the excitation cut and the outer surface of the loop antenna. The outer surface of the loop antenna is modelled as a perfectly electrically conducting structure, and the current distribution on the conductor is calculated using MoM. Methods for estimation of model parameters are developed. The soil surrounding the loop antenna is considered as an integrated part of the antenna, and the complex permittivity of the soil is estimated as a model parameter. The estimated complex permittivity is compared with typical values using the dielectric mixing model for soil as suggested by Mironov. Uncertainties of the estimated constitutive parameters are calculated and the uncertainties are considered as acceptable. The models for the loop antennas are used in the next Chapter 4 for calculation of the plane-wave transmitting spectra for GPR antennas.

Chapter 4

Measured Plane-Wave Transmitting Spectra of GPR Antennas

The plane-wave transmitting spectrum (PWTS), as defined in Chapter 2, is used for an accurate description of the electromagnetic field at any distance below the air-soil interface. Consequently, the PWTS contains valuable information that can be used in advanced methods for imaging of objects in the soil. The PWTS depends on the interactions between the GPR antenna and the air-soil interface, which in turn depends on the distance from the GPR antenna to the air-soil interface and the constitutive parameters of the soil. One purpose of the measurement facilities for GPR antennas is to improve the design procedure for GPR antennas. The desirable properties of the GPR antenna depend on the design of the GPR system and the working environment. The design of GPR antennas for a handheld GPR system using short-pulse time-domain signals has been discussed by Jongth et al. in [41]. For this GPR system it is desirable to design broadband GPR antennas, so that pulses with a wide frequency spectrum can be transmitted and received. Furthermore, the antenna should have a linear phase characteristic, and far-field parameters such as the polarization and the phase center should be constant. All these properties can be quantitatively evaluated if the PWTS is known.

Measurement procedures for GPR antennas have been developed during recent years. As suggested by Yarovoy et al. in [42] the GPR antennas above dry sand can be characterized by measurement of footprints using a time-domain system. Footprints are defined as the peak values of the transformed waveform between the GPR antenna under test (AUT) and the probe for the GPR AUT in a set of positions in a horizontal plane above the air-soil interface as suggested by Lestari et al. [15]. Facilities for comparative tests of GPR antennas above moist soil using a step frequency system have been suggested by Lenler-Eriksen et al. in [31]. In this method, a number of GPR

antennas are measured over a short time interval so that the measurement environment is unchanged between each measurement of a GPR antenna. For each frequency the voltage transfer function between the GPR AUT and the probe is measured for the GPR AUT in a set of positions in a horizontal plane above the air-soil interface. The amplitudes of the measured voltage transfer functions are used without any further data processing.

None of the proposed measurement procedures in [42] and [31] are based on a plane-wave expansion of the radiated electric field in the soil and a measurement of a PWTS such as described in Chapter 2. This procedure is suggested by Meincke and Hansen in [22] where an analysis of a simulated measurement of a GPR antenna is performed. The considered GPR antenna is a wire antenna close to the air-soil interface and the radiated electromagnetic field by the wire antenna is calculated in the soil using Hertzian dipoles. Various aspects of the measurement procedure have been discussed, including the effect of the finite scan plane. The effect of the finite scan plane size is also discussed by Yaghjian in [40] for planar near-field measurements in free space. It is concluded that only directive antennas can be measured using a planar scanner and that the measurement error due to the limited scan plane depends on the directivity of the GPR AUT. However, it has appeared that the error due to the finite scan plane is negligible for directive antennas. Similarly, it is believed that the error due to the limited scan plane for measurements of GPR antennas depends on the size of the foot print.

The stability of the matrix equation for calculation of the PWTS is evaluated, as suggested by Kerns in [21], for planar near-field measurements in free space. This method has also been described in Chapter 2. If Hertzian dipoles could be used as probes for the measurement of the GPR antenna, then the instability problem of the matrix equation is no problem, as it will be shown in Section 4.3. However, if feasible broadband probes are used, then the matrix equation can be unstable for certain spatial frequencies. Therefore, the method for evaluation of the stability is important during practical measurements of GPR antennas.

In this thesis practical measurements of the PWTS of GPR antennas is performed by measuring the radiated electromagnetic field in the soil using loop antennas. The plane-wave receiving spectra (PWRS) of the loop antennas are calculated using the models in Chapter 3. In Section 4.1, the usability of the loop antennas as probes is discussed. The loop antennas are used in a measurement facility as it will be described in Section 4.2. In Section 4.3, the procedure is used for measurement of GPR antennas. Furthermore, evaluation of the stability of the matrix equation for calculation of the PWTS is considered. Finally, in Section 4.4 the measurements procedure is verified by the measurement of a known GPR antenna above dry soil.

4.1 The Sensitivity of the Loop Antenna

In this section the sensitivity of the loop antenna is used to decide the usability of this probe for measurements of radiated electromagnetic field by GPR antennas. The usual coordinate system shown in the upper right corner of Figure 4.1 is used. The z-axis pointing into the upper half space and the air-soil interface is located in the plane $z = 0$. Perfectly electrically conducting (PEC) loops with a torus shape and radius of 17 mm are considered in a lossless medium with the relative permittivity $\varepsilon_{1,\omega}/\varepsilon_0 = 9$. The Fourier-transformed current distribution of a loop antenna is closely related to the plane-wave transmitting spectrum of the loop antenna, as shown by Meincke and Hansen in [22]. Therefore, the amplitude of the Fourier-transformed current distribution will give a hint about the far-field pattern and the sensitivity of the loop antenna. In Figure 4.1 two loops are considered in the xz- and xy-plane, respectively. The amplitude of the Fourier-transformed current distribution has been plotted as a function of the frequency for the angular spatial frequencies $(k_x, k_y) = (0\ \mathrm{m}^{-1}, 0\ \mathrm{m}^{-1})$. Hence, the sensitivity in the direction of the air-soil interface is considered. The red and blue curves represent the loop in the xz- and xy-plane, respectively.

For the loop antenna in the xz-plane a null is seen at the frequency 1.5 GHz. If the loop antenna is considered in free space, the null will occur at the frequency 4.5 GHz, which is in agreement with the sensitivity curve calculated for a loop antenna in free space by Yarovoy and Lighthart in [17]. Besides the null at 1.5 GHz, a near-null also occurs at the frequency 2.5 GHz. These nulls are very infavorable during measurements of plane waves with the spatial frequencies $(k_x, k_y) = (0\ \mathrm{m}^{-1}, 0\ \mathrm{m}^{-1})$.

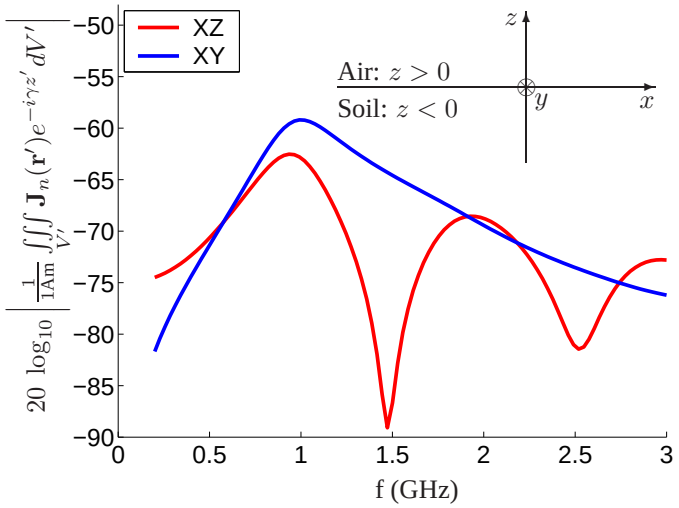

Figure 4.1: The Fourier-transformed current distribution for torus shaped loop antennas. The considered spatial frequencies are $(k_x, k_y) = (0\ \mathrm{m}^{-1}, 0\ \mathrm{m}^{-1})$.

Measurements using a loop antenna in the xz-plane should therefore be limited to frequencies below 1.5 GHz.

Loop antenna A, as described in Chapter 3, is used in the xz-plane in dry loam with the relative permittivity $\varepsilon_1'/\varepsilon_0 = 3.5$. The null at the frequency 1.5 GHz in Figure 4.1 for a soil with the permittivity $\varepsilon_{1,\omega}/\varepsilon_0 = 9$ will occur at the frequency 2.4 GHz when the permittivity of the soil is $\varepsilon_1'/\varepsilon_0 = 3.5$. It is therefore expected that the loop A only is usable for frequencies below 2.4 GHz in dry loam.

As seen in Figure 4.1 no null occurs in the frequency range from 0.2 GHz to 3 GHz for the loop antenna in the xy-plane. However, the amplitude of the Fourier-transformed current is lower than the amplitude for the loop antenna in the xz-plane for frequencies below 0.5 GHz. As expected a maximum in the amplitude occurs at the frequency 0.94 GHz when the circumference of the loop antenna is equal to the wavelength [43].

Loop antenna B from Chapter 3 is used in the xy-plane. This orientation was chosen so that the measurement facility could be used during a measurement campaign which was done in co-operation with Antenna Centre of Excellence (ACE) in the EU framework program. Loop antenna B is designed in such a way that measurement of the electromagnetic field in the soil is possible in the frequency range from 0.3 GHz to 3 GHz for a soil with the relative permittivity of $\varepsilon_1'/\varepsilon_0 = 8$. During this measurement campaign loop antenna B was used for a comparative test of GPR antennas using moist loam [31]. Loop B has also been used for measurement of the PWTS in dry loam, as will be described in Section 4.3 below.

Typical sensitivities for loop A and B are plotted as a function of the frequency in Figure 4.2 for the spatial frequencies $(k_x, k_y) = (0\ \mathrm{m}^{-1}, 0\ \mathrm{m}^{-1})$. The excitation cuts of the loop antennas are located 20 cm below the air-soil interface and the soil has the relative permittivity $\varepsilon_1'/\varepsilon_0 = 3.5$ and the conductivity $\sigma_1 = 0$ mS/m. Loop A has a null at the frequency 2.4 GHz and the sensitivity for loop B is higher for frequencies above 0.7 GHz. In the frequency range from 1 GHz to 2 GHz the sensitivity is between -40 dB and -35 dB where the sensitivity is measured relative to 1 m. Loop B has also been used for measurements in moist loam. In Figure 4.3 the sensitivity for loop B is soil with the relative permittivity $\varepsilon_1'/\varepsilon_0 = 8$ and the conductivity $\sigma_1 = 50$ mS/m are plotted as a function of the frequency at the spatial frequencies $(k_x, k_y) = (0\ \mathrm{m}^{-1}, 0\ \mathrm{m}^{-1})$. Since the excitation cut is 20 cm below the air-soil interface, the sensitivity is reduced by losses in the soil and the maximum sensitivity is -45 dB. The absence of nulls in the sensitivity for the spatial angular frequencies $(k_x, k_y) = (0\ \mathrm{m}^{-1}, 0\ \mathrm{m}^{-1})$ indicates that loop B is useful for measurements of GPR antennas. Other considerations such as the stability of the matrix equation for calculation of the PWTS of the GPR antenna are discussed in Section 4.3.

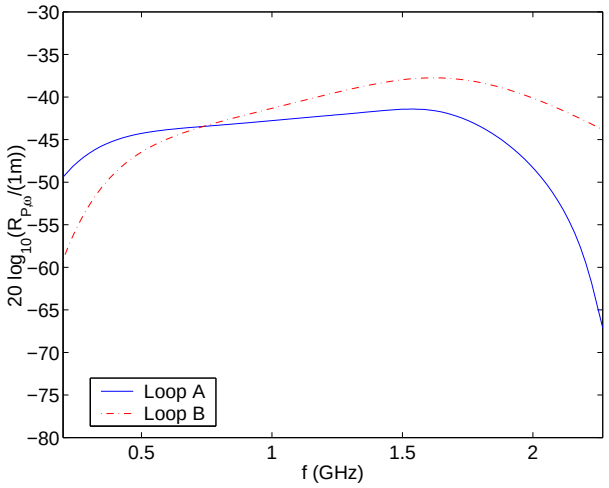

Figure 4.2: Typical sensitivities for loop A and B in soil with the relative permittivity $\varepsilon_1'/\varepsilon_0 = 3.5$ and the conductivity $\sigma_1 = 0$ mS/m. The excitation cuts of the loop antennas are 20 cm below the air-soil interface. The considered spatial frequencies are $(k_x, k_y) = (0\ \mathrm{m}^{-1}, 0\ \mathrm{m}^{-1})$.

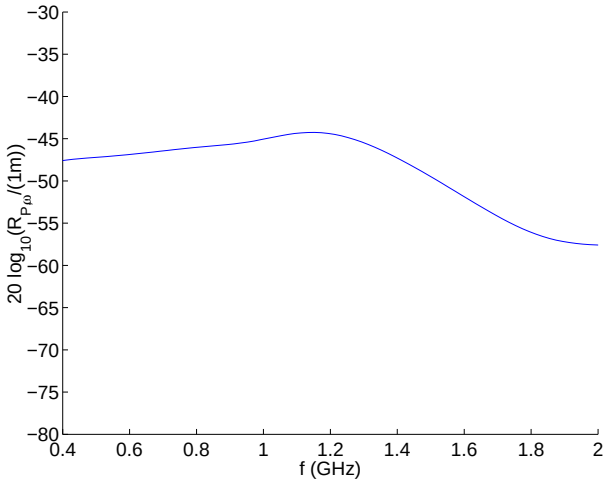

Figure 4.3: Typical sensitivity for loop B in soil with the relative permittivity $\varepsilon_1'/\varepsilon_0 = 8$ and the conductivity $\sigma_1 = 50$ mS/m. The excitation cuts of the loop antennas are 20 cm below the air-soil interface. The considered spatial frequencies are $(k_x, k_y) = (0\ \mathrm{m}^{-1}, 0\ \mathrm{m}^{-1})$.

4.2 The Measurement Procedure of the Plane-Wave Transmitting Spectrum

In this section, a practical method for measurement of the PWTS of a GPR antenna is suggested. The GPR antenna is assumed to be close to the air-soil interface, which is considered to be an integrated part of the GPR antenna. The measured PWTS depends on the distance between the GPR antenna and the air-soil interface. It is expected that the GPR antenna is well-shielded so that radiation of electromagnetic waves into the air is reduced to a minimum. Typically, GPR antennas are well-shielded to avoid reception of disturbing signals from the air and to obtain a good electromagnetic compatibility. Many different types of working environments can be considered for GPR antennas. In this thesis, a working environment with homogeneous soil and a planar air-soil interface is considered. In the following two different measurement configurations are considered for loop antenna A and B, respectively.

The facility using loop A for measurements of the electromagnetic field in the soil with the dimension $3.8\,\mathrm{m} \times 3.3\,\mathrm{m} \times 1.0\,\mathrm{m}$ is shown in Figure 4.4. The measurement coordinate system (x_m, y_m, z_m) is chosen so that the z_m-axis is pointing into the upper half-space. The facility consists of a wooden box with soil with an air-soil interface in the plane $z_m = 0$. Loop A is positioned in the soil and the GPR AUT is scanned above the air-soil interface. The PWTS is calculated using the measured voltage transfer functions $S_{nPA,\omega}$ between the loop antenna and the GPR AUT, as defined in Section 2.3. This measurement is performed using the network analyzer HP 8753A and the S-parameter test set HP 85046A. Loop A is connected to port 2 through a 7 m long armoured cable Sucoflex 104A. Similarly, the GPR AUT is connected to port 1 through a 9 m long armoured cable Sucoflex 104A. The cable is bendt around a wheel with a diameter of 20 cm so that a bending radius less than the minimum bending radius for the cable Sucoflex 104A is prevented. Before each measurement a full two-port calibration is made through the cables and the reference planes are fixed. This procedure demands that the loop antenna A is dug up and disconnected from the cable Sucoflex 104A before each measurement. The network analyzer HP 8753A is controlled using a Matlab graphical user interface (GUI) and communication via GPIB cables. Two motor-controllers are used for positioning of the GPR AUT in x_m and y_m. The motor-controllers are controlled via the Matlab GUI at the PC. The communication to the motor-controllers is performed through the RS232 interface using a positioning mode as defined in [69]. The position of the GPR AUT is controlled using a positioning system with belt drive ELZ 60 produced by BAHR and a high-precision planetary gear reducer BGT 530 produced by Tecnoingranaggi Riduttori. The GPR AUT is mounted on a carriage at the aluminum bar, and the y_m-position is controlled by moving the carriage along the aluminum bar as shown in Figure 4.5. The aluminum bar is mounted on carriage at an aluminum frame, and the x_m-position is controlled by moving the aluminum bar in the x_m-direction. The repeatability of the position for belt drive ELZ 60 has been specified to ± 0.1 mm in [70]. The circumference of the wheel in the ELZ 60 belt drive is 130 mm and the backlash in the gear reducer

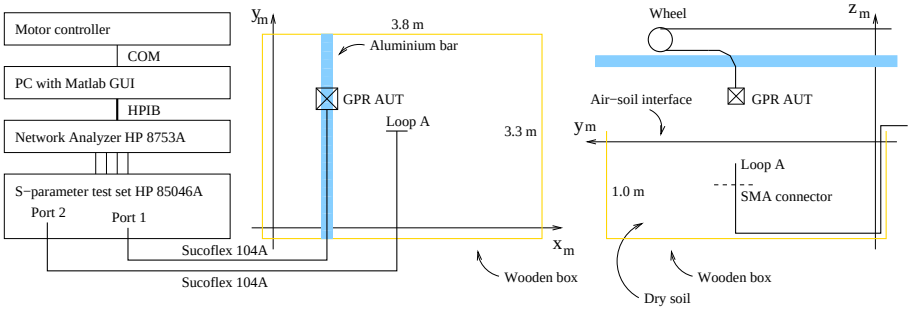

Figure 4.4: Measurement configuration using loop A for measurement of the electromagnetic field in the soil radiated by the GPR AUT.

BGT 530 is less than 0.25^o in [71] so that an additional uncertainty due to backlash is given by $(0.25^o \cdot \pi \cdot 130 \text{ mm})/180^o = 0.09$ mm. The repeatability of the position is therefore believed to be 0.2 mm. The voltage transfer function $S_{nPA,\omega}$ is measured for 64×64 positions of the GPR AUT using a step length of 30 mm. The air-soil interface is smoothed so that the distance between the GPR AUT and the air-soil interface is kept at a precision within ± 0.4 cm.

The GPR AUT is mounted on the carriage using a metallic cylindrical rod with a diameter of 22 mm, as shown in Figure 4.6. The distance between the air-soil interface and

Figure 4.5: The planar scanner for measurements of GPR antennas.

the mounting platform is 60.7 cm. Holes with a diameter of 6 mm for a pawl has been made in the cylindrical rod. The pawl is resting on the mounting platform so that the distance between the GPR AUT and the interface is fixed. The pawl can be in two positions I and II. In Figure 4.6 the pawl is in position I. The pawl is moved to position II by turning the GPR AUT 90^o around the axis of the cylindrical rod.

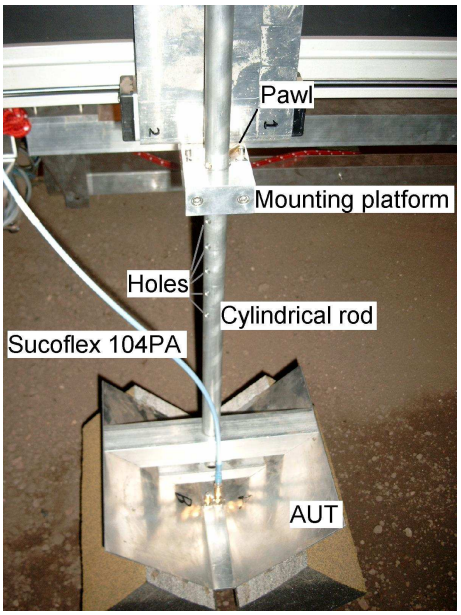

Figure 4.6: Mount for the GPR AUT.

The center of the cylindrical rod has been used as a reference point of the GPR AUT. The loop antenna A is positioned in such a way that the center of cylindrical rod is above the excitation cut when the mounting platform is moved to the position $(x_m, y_m) = (1100\,\text{mm}, 1100\,\text{mm})$. Only one loop antenna is used in the considered configuration. To obtain two equations for calculation of the PWTS, as required in Section 2.3, two scans are performed with the GPR antenna in position I and II. The scan with the GPR AUT in position I is denoted as scan I and similarly, the scan with the GPR AUT in position II is denoted as scan II. As shown in Figure 4.7 the measurement coordinate system for scan I is rotated 90^o so that a common coordinate system for scan I and II is obtained. In the common coordinate system (x_c, y_c) the orientation of the GPR AUT is the same for scan I and II but the loop antenna is used in a co- and cross-polarized orientation. The model for loop antenna A from Chapter 3 is the used for calculation of the PWRS, and the PWTS of the GPR AUT is calculated as described in Section 2.3.

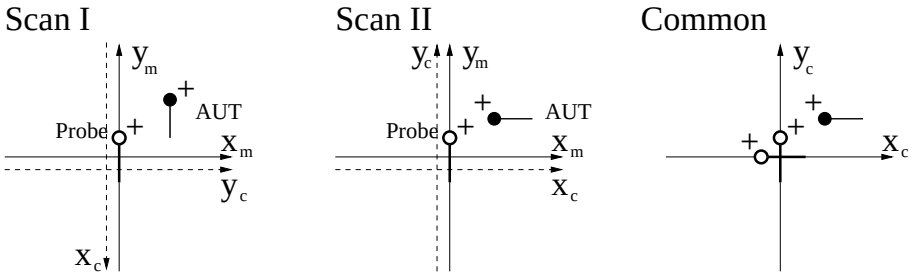

Figure 4.7: Orientation of the measurement coordinate system (x_m, y_m) and the common measurement system (x_c, y_c).

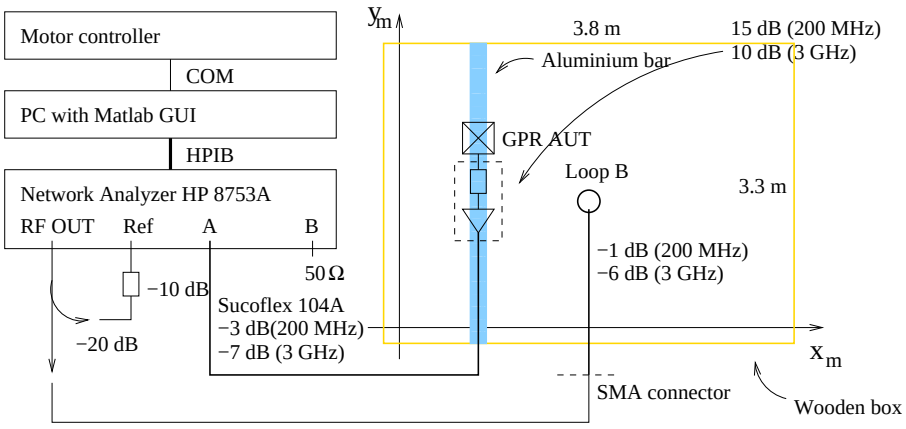

Figure 4.8: Measurement configuration using loop B for measurement of the electromagnetic field in the soil radiated by the GPR AUT.

The configuration using loop B for measurement of the electromagnetic field in the soil is shown in Figure 4.8. In this configuration the SMA connector at the semi-rigid cable is outside the wooden box so that the loop antenna can be disconnected from the cable to the network analyzer without changing the position of the loop antenna in the soil. The network analyzer has four ports, the RF out port, the reference port (R), port A (A), and port B (B) as described in [68]. In the considered configuration the four ports have been disconnected from the S-parameter test set for three reasons. First, it is desirable to avoid use of the mechanical switches in the S-parameter test set since the switches can only be used for a finite number of times. Second, the use of the switches in the S-parameters test set is time-consuming. Third, losses in the S-parameters test set can be avoided by a direct connection to the ports RF out, R, A, and B. In the considered configuration, the loop antenna is transmitting and the GPR AUT is receiving.

The port RF out is connected directly to the loop antenna through a directional coupler, and the output power of the network analyzer is set to 10 dBm. A fraction of -20 dB of the signal is directed to the reference channel through a 10 dB attenuator. The losses in the semi-rigid cable to the excitation cut of loop B increases from 1 dB at the frequency 200 MHz to 6 dB at 3 GHz. The attenuation between the loop antenna and the GPR AUT depends on the considered GPR AUT and it must be considered as an unknown parameter in the system. To improve the signal-to-noise ratio the signal is amplified after

Figure 4.9: Mount for the loop for loop antenna B.

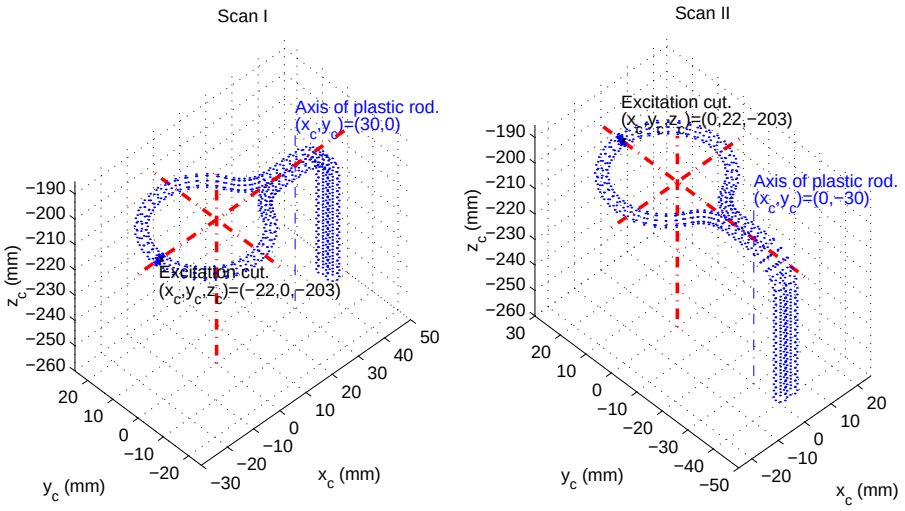

Figure 4.10: The geometry of the probe in the common coordinate system.

the GPR AUT. The amplification is decreasing from 15 dB at 200 MHz to 10 dB at 3 GHz. Finally, the attenuation from the amplifier to port A is increasing from 3 dB at 200 MHz to 7 dB at 3 GHz. Port B is terminated in a load with a resistance of $50\ \Omega$. The network analyzer is used for measurements of the ratio A/R. To calculate the voltage transfer function $S_{nAP,\omega}$ the response of the network analyzer must be known. This response is measured by a reference measurement through a well-known 20 dB attenuator. The calculated voltage transfer function $S_{nAP,\omega}$ has been compared with the measured voltage transfer function using the S-parameter test set and an agreement have been found in both amplitude and phase. Loop B is mounted at a fixed position on a plastic rod as shown in Figure 4.9. The positions of the axis of the plastic rod and the metallic rod are identical when the carriage with the GPR AUT is moved to the position $(x_m, y_m) = (1100\text{ mm}\ , 1100\text{ mm})$ in the measurement coordinate system. The reference point for the loop is chosen to $(x_m, y_m) = (1100\text{ mm}, 1130\text{ mm})$. Only one loop antenna is used in the measurement configuration. As described for loop antenna A, two scans denoted by I and II are performed. Scan I is rotated 90^o so that a common coordinate system is achieved. The orientation of loop antenna B is shown in Figure 4.10. Using the current distribution in (3.18) the PWRS of the loop antenna is achieved, and the PWTS of the GPR AUT is calculated as described in Section 2.3.

4.3 Measurements of GPR Antennas

Measurements of the PWTS of GPR antennas are used for an accurate characterization of the radiated electromagnetic field. The final purpose in this thesis is to include the PWTS in methods for imaging as suggested by Meincke in [25]. This technique for imaging provides the possibility to extend the types of antennas usable for GPR imaging to include dispersive broadband antennas which are denoted as antennas of little use in time-domain GPR systems by Jongth et al. in [20]. In this section, a bowtie antenna designed by Eide in [23] and an equiangular spiral antenna are measured. It is expected that the bowtie antenna can be used for GPR imaging without explicit knowledge about the PWTS. The radiation pattern from a bowtie antenna close to an air-soil interface is comparable with the radiation pattern from a Hertzian dipole close to an air-soil interface. Therefore, the method as suggested by Meincke and Hansen in [24] is usable for the bowtie antenna. As opposed to the bowtie antenna, knowledge about the PWTS of the equiangular spiral antenna is necessary for GPR imaging. The PWTS for a single spiral antenna as transmitter and receiver is successfully used for imaging by Meincke et al. in [34]. Therefore, it is expected from a theoretical point of view that the spiral antenna is usable for GPR imaging.

The measured bowtie antennas and equiangular spiral antenna are described in Section 4.3.1. The measurement results are presented in Section 4.3.2 using the antenna parameters as defined in Section 2.2. Finally, in Section 4.3.3 the stability of the calculation of the PWTS is considered.

4.3.1 Description of the Measured GPR Antennas

Two antennas, the bowtie antenna and the spiral antenna are measured. The construction of the bowtie antenna in Figure 4.11 is similar to that of the switch-bowtie antenna arrays in [23], [13], and [14]. The constructed antenna is a monopole made of a triangular piece of copper. The side length of the equilateral triangle is 12 cm. The bowtie monopole is positioned below a V-shaped ground plane and it is resistively loaded using an absorber as seen in the right picture in Figure 4.11. The feeding cable is connected to a SMA connector at the V-shaped ground plane. The corner of the bowtie triangle close to the bottom of the V-shaped ground plane is soldered to the center conductor of a SMA connector through a hole. The two other corners of the triangle are connected through $121\ \Omega$ resistors to a piece of metal that is connected to the ground plane. The bowtie antenna is therefore partly resistively loaded by use of absorbers and by use of SMA resistors. During the measurements the distance between the lower part of the V-shaped ground plane and the air-soil surface is 11.0 cm. As estimated in Section 3.3.2 on page 41, the permittivity is estimated to $\varepsilon'_{1,\omega}/\varepsilon_0 = 7.80$ and the conductivity is $\sigma_{1,\omega} = a_c f$ with the proportionality constant $a_c = 51$ mS/m/GHz.

Two equiangular spiral antennas as shown in Figure 4.12 are designed as described in [43, pp. 545-549]. The spiral antennas are denoted by spiral antenna 1 and 2, respectively. Each arm is an equiangular metallic surface described by outer and inner

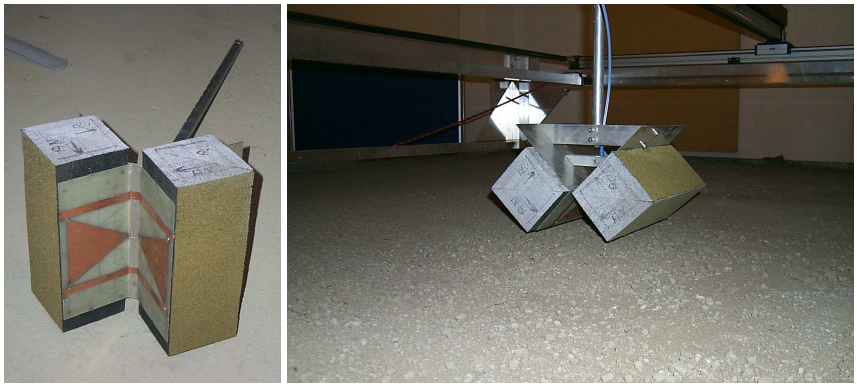

Figure 4.11: The measured monopole bowtie antenna. **Left:** Bottom view. **Right:** Mounted in the measurement facility for GPR antennas.

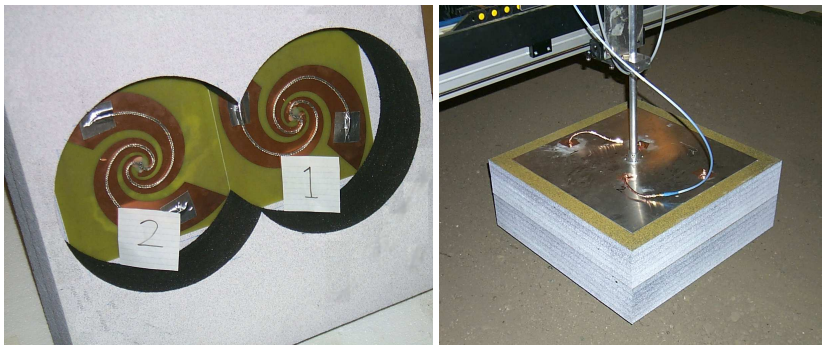

Figure 4.12: The measured equiangular planar spiral antennas. **Left:** Bottom view. **Right:** Mounted in the measurement facility for GPR antennas.

radii ρ_1 and ρ_2, respectively. The outer radius ρ_1 is given by

$$\rho_1 = \rho_0 e^{a\Theta}, \tag{4.1}$$

where ρ_0 is denoted by the initial outer radius, a_0 is denoted by the growth rate, and Θ is the angular position. For the spiral antennas in Figure 4.12 the growth rate is $a_0 = 0.30$ rad^{-1} and the the initial outer radius is $\rho_0 = 15$ mm. The inner radius is given by

$$\rho_2 = K_0 \rho_1, \tag{4.2}$$

where the constant is $K_0 = 0.5$ for the the two spiral antennas in Figure 4.12. The constant K_0 is selected in such a manner that the arm length necessary to produce a circularly polarized field in the far-field region is minimized using results described by Dyson in [72]. The results are considered as normative for the spiral close to an air-soil interface. The spiral antennas are designed with a turn of 1.22 and the radiated electromagnetic field should be circularly polarized from 0.65 GHz in free space. Spiral antenna 1 is left-hand circularly polarized and spiral antenna 2 is right-hand circularly polarized. The excitation of the spiral antennas is balanced by embedding the coaxial feed cable in the metallic surface of the arms as suggested by Dyson in [72]. An absorber with a hole is placed in front of the spiral antennas which are mounted on an absorber ECCOSORB AN-79 with the size 61 cm $\times$ 61 cm $\times$ 11.4 cm. The absorber and the spiral antennas are placed below a metal plate as shown in the right picture of Figure 4.12. The distance between the air-soil interface and the absorber in front of the spiral antennas is 5.0 cm. The relative permittivity is estimated to $\varepsilon'_{1,\omega}/\varepsilon_0 = 3.60$ and the conductivity is $\sigma_{1,\omega} = 25$ mS/m.

4.3.2 Characterization of the GPR Antennas

The plane-wave transmitting spectra are measured using the method as described in Section 2.3. Due to the limited size of the scan area the measured voltage transfer function $S_{nPA,\omega}$ is multiplied with a Hamming window function before the Fourier transform is applied, as suggested by Meincke and Hansen in [22].

The monopole bowtie antenna is pointing in the direction of the unit vector $\hat{\mathbf{x}}_c$ in the common coordinate system defined in Figure 4.7. Therefore, it is expected that the bowtie antenna is $\hat{\mathbf{x}}_c$-polarized. In Figure 4.13 the amplitudes of the measured PWTS for the bowtie antenna are plotted as a function of the spatial frequencies (k_x, k_y) at the frequency 1.06 GHz. Two circles mark the boundary between propagating and evanescent plane waves. Inside the inner circle the plane waves are propagating in air, and inside the outer circle plane waves are propagating in soil. Outside the outer circle plane waves are evanescent in the soil. These plane waves are not measurable using the considered facility, and as a consequence the calculated PWTS has erroneous large amplitudes. In the region between the inner and outer circle the plane waves are evanescent in air but propagating in the soil, and in large parts of this region

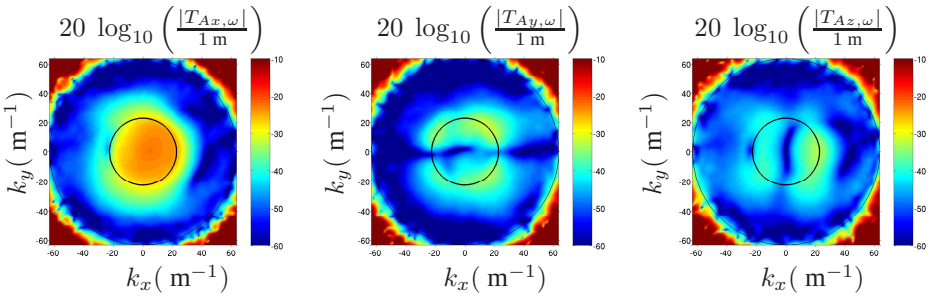

Figure 4.13: The amplitude of the PWTS for the bowtie antenna.

the measurements are dominated by noise. Inside the inner circle plane waves are both propagating in air and soil. In this region, the procedure gives reasonable measurements of the PTWS that can be used for GPR imaging. The PWTS of the bowtie antenna is seen to be rather limited to the propagating modes for the $\hat{\mathbf{x}}_c$-polarized electric field.

Since the evanescent plane waves in the soil are negligible, cf. Figure 4.13, accurate calculations of the electric field can be performed at $z_c = 0$. In Figure 4.14 the electric field in the soil at $z_c = 0$ is plotted as a function of the position (x_c, y_c) at the frequency 1.06 GHz. The electric field is calculated using the measured PWTS multiplied with the window-function

$$W_F(k_{xy}) = \begin{cases} 1 & ,k_{xy} \leq k_{0,\omega} \\ \frac{1}{2} + \frac{1}{2}\cos\left(\frac{(k_{xy}-k_0)\pi}{k^r_{1,\omega}-k_0}\right) & ,k_0 < k_{xy} < k^r_{1,\omega} \\ 0 & ,k^r_{1,\omega} \leq k_{xy}. \end{cases} \tag{4.3}$$

where $k_{xy} = \sqrt{k_x^2 + k_y^2}$, $k_0 = \omega\sqrt{\mu_0\varepsilon_0}$, and $k^r_{1,\omega} = \omega\sqrt{\mu_0\varepsilon'_{1,\omega}}$. The propagating modes in air are very important in the calculation of the electric field. Therefore, the plane-wave transmitting spectrum is multiplied with $W_F(k_{xy}) = 1$ in the re-

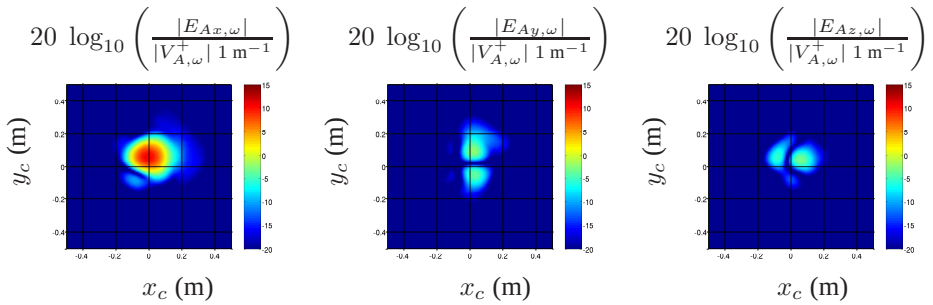

Figure 4.14: The amplitude of the electric field below the air-soil interface for the bowtie antenna.

gion $k_{xy} \leq k_0$. Outside the region $k_{xy} \leq k_0$ the measured plane-wave transmitting spectrum is gradually more dominated by noise. The window function has therefore been chosen so it decreases from $W_F(k_{xy}) = 1$ at $k_{xy} = k_0$ to $W_F(k_{xy}) = 0$ at $k_{xy} = k^r_{1,\omega}$. The amplitude of the electric field components $E_{Ax,\omega}$, $E_{Ay,\omega}$, and $E_{Az,\omega}$ are calculated for the bowtie antenna at $z_c = 0$ and they are plotted in Figure 4.14. It is seen that radiated electric field mainly consists of the x_c-component $E_{Ax,\omega}$ at the frequency 1.06 GHz.

The PWTS is measured in the frequency range from 0.5 GHz to 1.6 GHz. In this frequency range the transmission efficiency $\eta_{A,\omega}$ is almost constant and equal to -12 dB. The partial transmission efficiencies $\eta_{Ax,\omega}$ and $\eta_{Arhcp,\omega}$ are plotted as function of the frequency in Figure 4.15. The partial transmission efficiency $\eta_{Ax,\omega}$ is 0.90 and $\eta_{Arhcp,\omega}$ is 0.50. Therefore, the electric field consists mainly of the x_c-component $E_{Ax,\omega}$ over the considered range of frequencies. The measured reflection coefficient $S_{AA,\omega}$ of the bowtie antenna varies between -6 dB and -12 dB in the frequency range from 0.5 GHz to 2.0 GHz. The reflection coefficient appeared to be very sensitive to the position of the absorbers close to the feed and the soldering to the feed SMA connector.

The PWTS of the equiangular spiral antenna is measured in the frequency range from 0.6 GHz to 2.0 GHz. The transmission coefficient $\eta_{A,\omega}$ varies between -12 dB and -7 dB in this range of frequencies. The partial transmission efficiencies $\eta_{Ax,\omega}$ and $\eta_{Arhcp,\omega}$ are plotted as a function of the frequency in Figure 4.16. For spiral antenna 1, $\eta_{Arhcp,\omega}$ is 0.10 and $\eta_{Ax,\omega}$ varies between 0.35 and 0.60. Hence, spiral antenna 1 in Figure 4.12 is a left-hand circularly polarized antenna. Spiral antenna 2 is the mirror image of spiral antenna 2 and it is right-hand circularly polarized. The reflection coefficient $S_{AA,\omega}$ for the spiral antennas varies between -12 dB and -6 dB.

4.3.3 Stability of the Matrix Equation for Characterization of the GPR Antennas

The stability of the matrix equation for the calculation of the PWTS of the GPR AUT depends on the chosen set of probes. Hertzian dipoles were chosen as probes in the theoretical investigation as performed by Meincke and Hansen in [22]. To evaluate the stability of a measurement system using two Hertzian dipoles, the stability parameter $\cos(\Phi_\omega(k_x, k_y))$, as defined in Section 2.3, is calculated for two orthogonal Hertzian dipoles. The relation between the voltage of the incoming wave $V^+_{A,\omega}$ and the current distribution for a $\hat{\mathbf{x}}$- and $\hat{\mathbf{y}}$-polarized Hertzian dipole of length Δl is written as

$$\mathbf{J}_{1A} = -2Y_c V^+_{A,\omega} \Delta l \hat{\mathbf{x}} \delta(x)\delta(y)\delta(z), \tag{4.4}$$

$$\mathbf{J}_{2A} = -2Y_c V^+_{A,\omega} \Delta l \hat{\mathbf{y}} \delta(x)\delta(y)\delta(z), \tag{4.5}$$

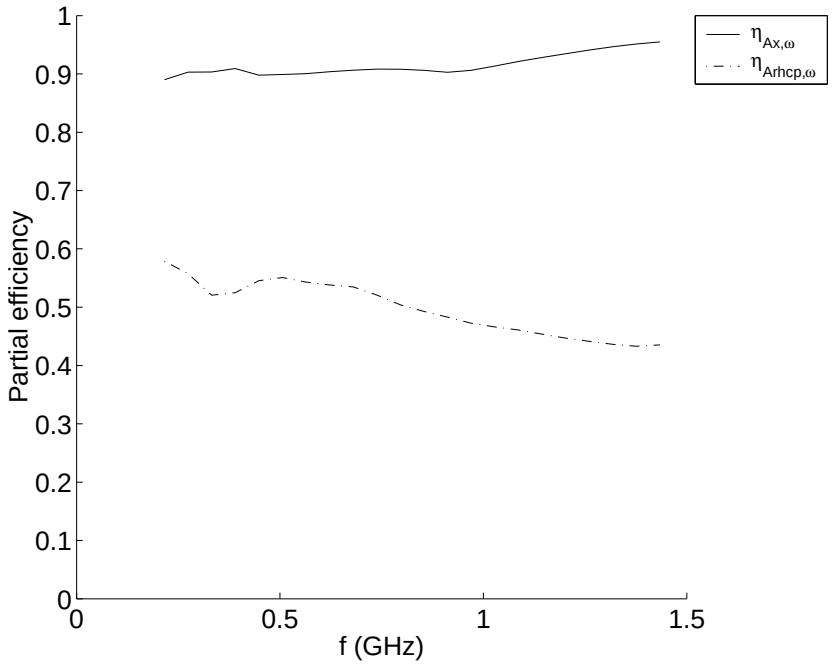

Figure 4.15: Partial transmission efficiencies for the bowtie antenna. The partial fraction $\eta_{Ax,\omega}$ of the transmitted power due to the $\hat{\mathbf{x}}_c$-polarized tangential electric field and the partial fraction $\eta_{Arhcp,\omega}$ of the transmitted power due to the $\hat{\mathbf{e}}_{rhcp}$-polarized tangential electric field.

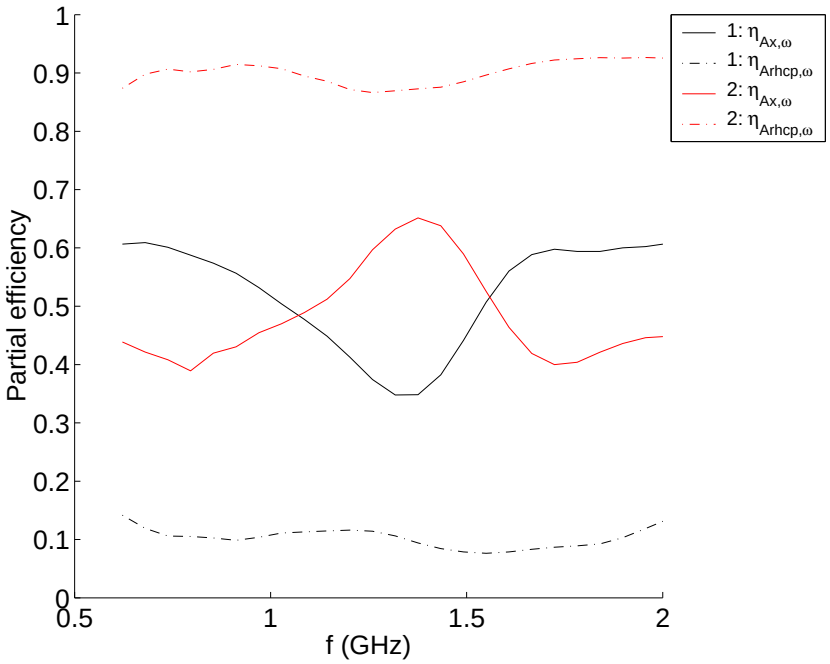

Figure 4.16: Partial transmission coefficients for the equiangular spiral antennas 1 and 2. The partial fraction $\eta_{Ax,\omega}$ of the transmitted power due to the $\hat{\mathbf{x}}_c$-polarized tangential electric field and the partial fraction $\eta_{Arhcp,\omega}$ of the transmitted power due to the $\hat{\mathbf{e}}_{rhcp}$-polarized tangential electric field.

respectively. Given the current distribution in (4.4) and (4.5) the PWRS is given by [22]

$$\mathbf{R}_{1P,\omega}(k_x,k_y) = \Delta l\left(\hat{\mathbf{x}}\left(1-\frac{k_x^2}{k_{1,\omega}^2}\right) - \hat{\mathbf{y}}\frac{k_xk_y}{k_{1,\omega}^2} + \hat{\mathbf{z}}\frac{k_x\gamma_{1,\omega}(k_x,k_y)}{k_{1,\omega}^2}\right), \tag{4.6}$$

$$\mathbf{R}_{2P,\omega}(k_x,k_y) = \Delta l\left(-\hat{\mathbf{x}}\frac{k_xk_y}{k_{1,\omega}^2} + \hat{\mathbf{y}}\left(1-\frac{k_x^2}{k_{1,\omega}^2}\right) + \hat{\mathbf{z}}\frac{k_x\gamma_{1,\omega}(k_x,k_y)}{k_{1,\omega}^2}\right). \tag{4.7}$$

The vectors $\boldsymbol{W}_{nP,\omega}$ as defined in (2.59) are given by

$$\boldsymbol{W}_{1P,\omega} = \gamma_{1,\omega}(k_x,k_y)\hat{\mathbf{x}}, \tag{4.8}$$

$$\boldsymbol{W}_{2P,\omega} = \gamma_{1,\omega}(k_x,k_y)\hat{\mathbf{y}}, \tag{4.9}$$

so that the stability parameter as defined in (2.63) is given by $\cos(\Phi_\omega(k_x,k_y)) = 0$. Herein, Hertzian dipoles are the optimum choice with the respect to the stability of the matrix equations. However, the Hertzian dipole is a purely theoretical antenna and other parameters such as the sensitivity and wideband properties of the antenna are also important. In Figure 4.17, the amplitude $|\cos(\Phi_\omega)|$ is plotted as a function of the spatial angular frequencies (k_x,k_y) at the frequencies 1.09 GHz and 1.78 GHz. At the frequency 1.09 GHz the amplitudes $|\cos(\Phi_\omega)|$ are near null in almost the entire region for propagating plane waves in the soil. Therefore, loop antenna B is very usable at this frequency. It is more difficult to use loop antenna B at the frequency 1.78 GHz since the amplitude $|\cos(\Phi_\omega)|$ is near one in the region between $(-50\ \mathrm{m}^{-1}, 0\ \mathrm{m}^{-1})$ and $(0\ \mathrm{m}^{-1}, -50\ \mathrm{m}^{-1})$. In this region erroneous results are expected due to a poor stability.

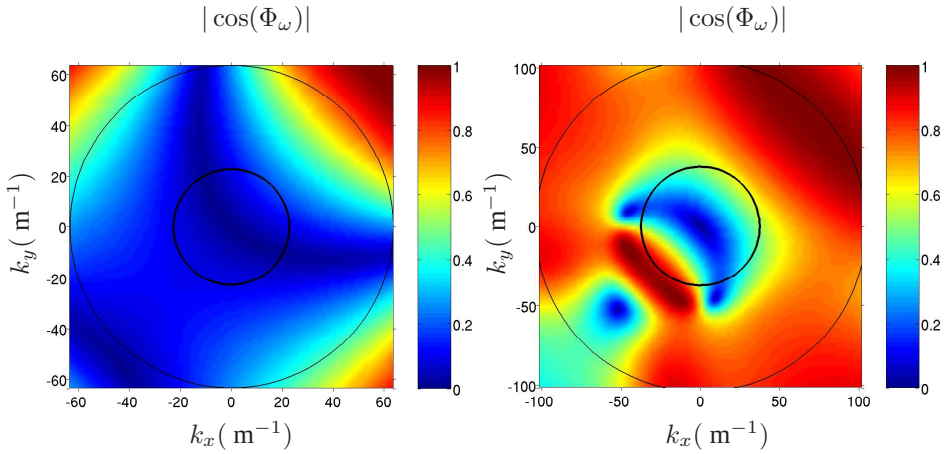

Figure 4.17: Amplitude $|\cos(\Phi_\omega)|$ for the pair of loops. **Left:** 1.09 GHz. **Right:** 1.78 GHz.

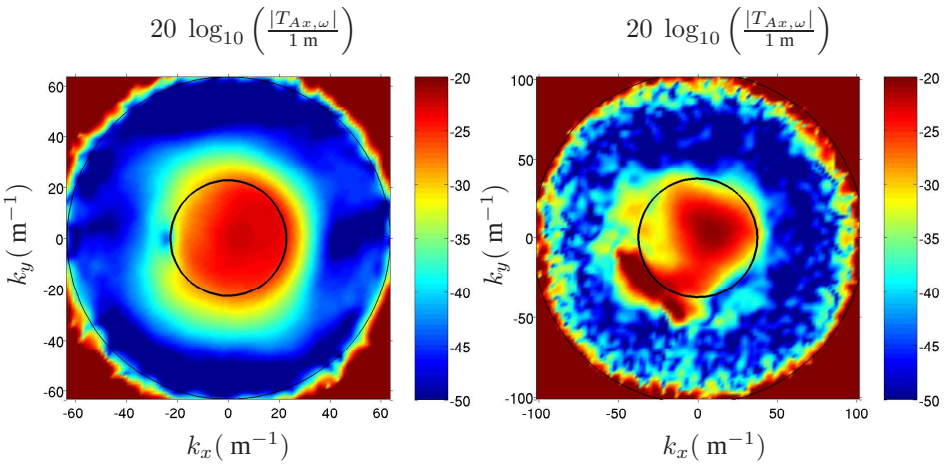

Figure 4.18: Amplitude $|T_{Ax,\omega}|$ of the measured plane-wave transmitting spectrum of the bowtie antenna. **Left:** 1.09 GHz. **Right:** 1.78 GHz.

In Figure 4.18 the amplitude of $|T_{Ax,\omega}|$ for the bowtie antenna is plotted as a function of the spatial angular frequencies at the frequencies 1.09 GHz and 1.78 GHz. As expected, the x_c component of the electric field is mainly composed of plane waves that are propagating in the air at the frequency 1.09 GHz. At the frequency 1.78 GHz erroneously large amplitudes appear in the region between $(-50\ \mathrm{m}^{-1}, 0\ \mathrm{m}^{-1})$ and $(0\ \mathrm{m}^{-1}, -50\ \mathrm{m}^{-1})$ due to the poor stability as shown in Figure 4.17. Furthermore, the calculated amplitudes at the frequency 1.78 GHz is more dominated by noise than at the frequency 1.09 GHz. The noise is more dominating at the frequency 1.78 GHz due to the losses in the soil. As discussed in Section 3.3.2 the conductivity of the soil is proportional to the frequency. Therefore, the sensitivity $|\mathbf{R}_{A,\omega}|$ of the loop antenna decreases as the frequency increases.

Reliable calculation of the PWTS for a GPR AUT is only expected if $|\cos(\Phi_\omega)|$ is sufficiently low and the amplitude of the sensitivity $|\mathbf{R}_{A,\omega}|$ is sufficiently high. In this thesis the usual region is defined as $20\log_{10}(|\mathbf{R}_{A,\omega}|/(1\ \mathrm{m})) > -55$ dB and $|\cos(\Phi_\omega)| < 0.8$.

4.4 Verification of the Measurement Procedure

The measurement of the plane-wave transmitting spectrum is complicated by stochastic fluctuation in the complex permittivity of the soil. These fluctuations can influence in particular the properties of the loop antenna in the soil which may vary between different measurements due to fluctuations of the complex permittivity of the soil surrounding the loop. To verify the measurement procedure a loop antenna with a known PWTS is measured above dry and homogeneous soil.

The PWTS is measured for loop antenna A in the air as described by Lenler-Eriksen and Meincke in [32] and [33]. The loop antennas are shielded by an absorber

Figure 4.19: Loop antenna A below an absorber ECCOSORB AN-79 with the size 61 cm x 61 cm x 11.4 cm.

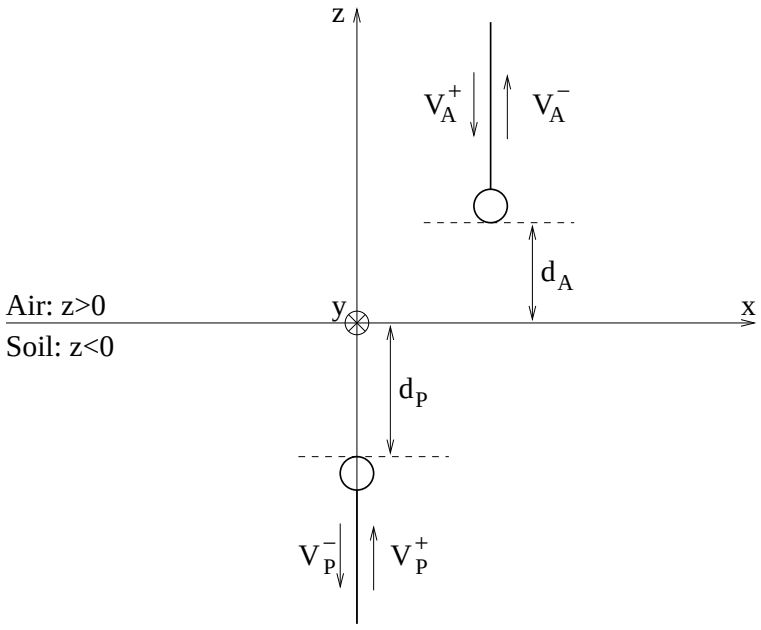

Figure 4.20: Configuration for measurement of a known loop antenna of type A above the air-soil interface.

ECCOSORB AN-79 above the antenna as shown in Figure 4.19. The distance d_A between the excitation cut and the air-soil interface is 10.0 cm as shown in Figure 4.20. The reference plane is located at the excitation cut, and the voltages of the incoming and outgoing wave in the reference plane are denoted by $V^+_{A,\omega}$ and $V^-_{A,\omega}$, respectively. It is assumed that multiple interactions between the loop antenna and the interface can be neglected.

The loop antenna of type A is used for the measurement of the radiated electromagnetic field in the soil, and the reference plane is located at the SMA connector located at the SMA connector as described in Section 3.1.1. The voltages of the incoming and outgoing wave in the reference plane are denoted by $V^+_{A,\omega}$ and $V^-_{A,\omega}$. The distance d_P between the excitation cut and the air-soil interface is 12.5 cm. The complex permittivity of the soil is estimated using the procedure described for loop A in Section 3.2.2. The permittivity of the soil is estimated to $\varepsilon_1'/\varepsilon_0 = 3.5$ and the conductivity is estimated to $\sigma_1 = 21$ mS/m. The PWRS of the loop A in the soil is calculated as described in Section 3.1.2, and the measured voltage transfer function $S_{nPA,\omega}$ is used for calculation of the PWTS of the loop antenna in air as described in Section 2.3. The known loop antenna is in the xz-plane so that is $\hat{\mathbf{x}}$-polarized. In Figure 4.21 the amplitude of $T_{Ax,\omega}/\lambda_0$ is plotted as a function of the frequency for $(k_x, k_y) = (0\ \mathrm{m}^{-1}, 0\ \mathrm{m}^{-1})$. The theoretical PWTS is calculated using the knowledge about the current distribution at the loop antenna and the measured PWTS is calculated using the measured voltage transfer function $S_{nPA,\omega}$. The difference between the measured and theoretical amplitude of $T_{Ax,\omega}/\lambda_0$ is less than 1 dB over a frequency range from 1.08 GHz to 1.92 GHz. In Figure 4.22 the amplitude of $T_{Ax,\omega}/\lambda_0$ is plotted as a function of the normalized angular spatial frequency k_x/k_0 at 1.6 GHz. The difference between the measured and theoretical amplitude of $T_{Ax,\omega}/\lambda_0$ is less than 4 dB for propagating plane waves. The attenuation of evanescent plane waves is measurable for spatial frequencies below $k_x/k_0 < 1.5$. However, the uncertainty of the spectrum of evanescent plane waves in air is huge. For spatial frequencies above $k_x/k_0 > 1.5$ only noise is detectable. An excellent agreement between the theoretical and measured PWTS is obtained. Therefore, it is expected that the measurement procedure can give valuable information about GPR antennas.

4.5 Summary

A measurement procedure for GPR antennas is developed where the radiated electromagnetic field by the GPR antenna is measured in the soil using loop antennas. Probe correction is performed using knowledge about the PWRS of the loop antennas, and the PWTS for the GPR antennas is calculated as suggested by Meincke and Hansen in [22]. The usable range of frequencies for the measurement facility is limited by the stability of the matrix equation for the calculation of the PWTS of the GPR antennas as described by Kerns in [21]. The usable range is also limited by the small amplitudes of the PWRS of the loop antennas. The measured PWTS has been measured for a loop antenna in the air above the air-soil interface. The PWTS for this loop an-

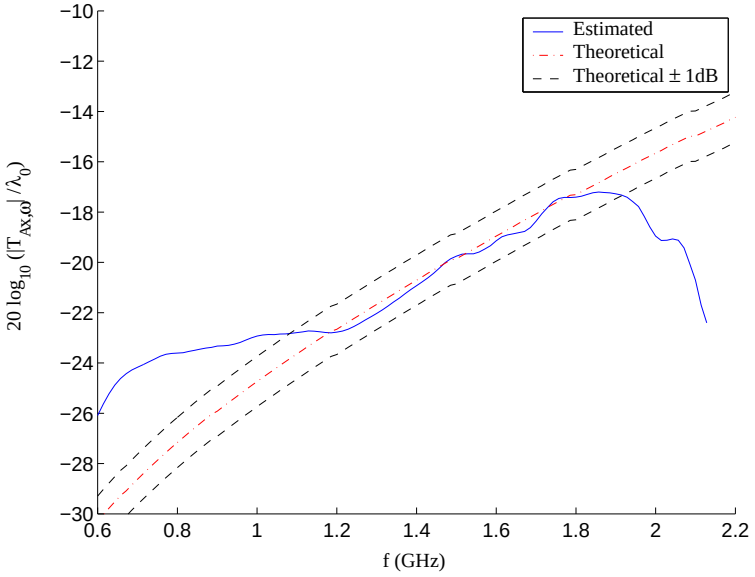

Figure 4.21: Amplitude of $T_{Ax,\omega}/\lambda_0$ for the spatial frequencies $(k_x, k_y) = (0\ \mathrm{m}^{-1}, 0\ \mathrm{m}^{-1})$.

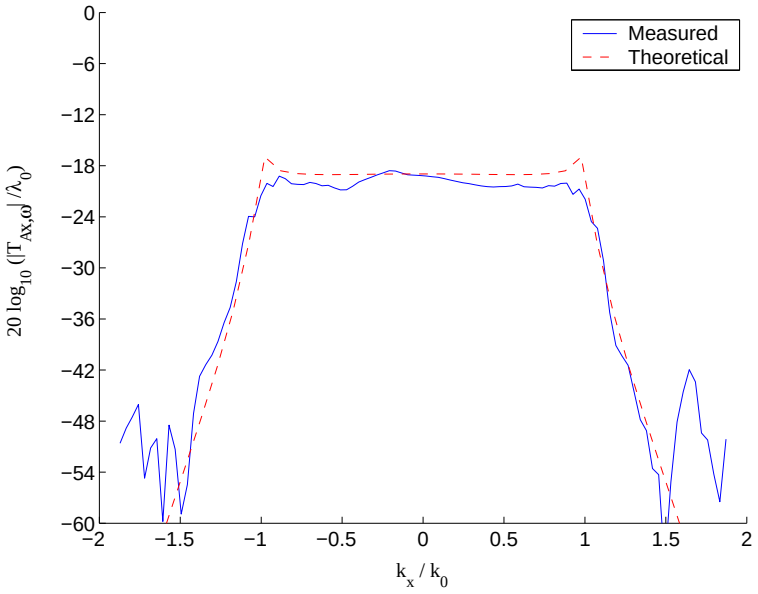

Figure 4.22: Amplitude of $T_{Ax,\omega}/\lambda_0$ for the frequency 1.6 GHz and the spatial frequency $k_y = 0\ \mathrm{m}^{-1}$.

tenna is calculated and compared with the measured PWTS. An excellent agreement between the measured PWTS and the calculated PWTS were achieved for propagating plane waves. This result indicates that the measured PWTS of propagating plane waves in air is usable for imaging as suggested by Meincke in [25]. A non-dispersive and linearly polarized bowtie antenna as designed by Eide in [23] is measured, and dispersive circularly polarized equiangular spiral antennas are measured. The PWTS for these antennas is used in the following Chapter 5 for GPR imaging.

Chapter 5

Imaging using GPR Systems

A number of the methods for GPR imaging are based on the experience from seismics. In seismic methods the data processing of scattering data for the vectorial electromagnetic waves are similar to the data processing for scalar acoustic waves. Furthermore, the antennas are modeled as point sources without taking into account the different transmitting and receiving characteristics of the GPR antennas. A tutorial on some of these methods is given by Eide in [23] and by Daniels in [1, pp. 247-293]. Many GPR systems produce an echogram in which point scatterers in the soil appear as hyperbolas. If the GPR system is a time-domain system then very little or no data processing is necessary. Often average subtraction is performed to remove the response of the GPR antennas and the air-soil interface. Migration methods are used for back propagation of the detected scattered field. Several different migration methods have been developed. The Kirchhoff migration is a popular method and this method is reported to give better images than plotting of the raw data in an echogram [1], [73].

Inversion techniques give complete knowledge of the constitutive parameters. To perform an inversion the data processing is based on knowledge about wave propagation of the electromagnetic waves in the soil and the radiation characteristics of the GPR antennas. Using the Born approximation a linear Fredholm integral equation of the first kind can be obtained. The inversion can be implemented using a numerical approach or an analytical approach. In the numerical approach, the linear Fredholm integral equation is brought to a matrix equation of the form $\overline{\mathbf{A}} \cdot \mathbf{x} = \mathbf{b}$ using basis and weighting functions [74], [75]. A numerical approach is suggested by Deming and Devaney in [74]. In this approach, the GPR antennas are characterized using the receiving and transmitting characteristics as suggested by Kerns in [21]. So far, analytical inversion schemes require a lossless background medium whereas the numerical inversion scheme allows attenuation in the background medium. Similarly, a numerical inversion scheme is suggested by Meincke in [75]. In this approach, the GPR antennas are characterized by the current distribution close to a planar air-soil interface. The linear inversion is performed using Tikhonov or other regulation methods [76]. Several analytical approaches for imaging in a lossless background medium

have been developed during the last decades [24], [25], [77], and [78]. An inversion scheme based on Huygen principle is suggested by Van Dongen et al. in [77]. The considered stepped-frequency GPR system consists of two spiral antennas which are characterized by footprints. It is reported that the method developed is suitable for fast and robust imaging of targets in the soil. Another method based on a plane-wave expansion of the electromagnetic waves is suggested by Hansen and Meincke in [24]. In this paper a fixed-offset system of Hertzian-dipoles is considered, and a quantitative estimation of the constitutive parameters of a weak scatterer is calculated. This method is extended to involve arbitrary antennas with a known current distribution in [78]. However, knowledge of the current distribution at the GPR antenna is not mandatory. Knowledge of the plane-wave transmitting spectrum can also be used in inversion schemes as suggested by Meincke in [25].

So far, no practical results using the method in [25] have been published. To this end the plane-wave transmitting spectrum of the GPR antennas in question must first be measured. In this thesis, the plane-wave transmitting spectra for a linearly polarized bowtie antenna and a circularly polarized equiangular planar spiral antenna are used for imaging of a buried plastic pipe. In order to investigate the importance of taking into account the plane-wave transmitting spectrum in the imaging procedure, these images are compared with images constructed using a simple Hertzian-dipole model of the GPR antennas.

In Section 5.1 the inversion scheme of [25] is explained. A method for preprocessing of the measured scattering data is suggested in Section 5.2. In Section 5.3 the inversion scheme in [25] is used for construction of images of the plastic pipe. These images are compared with constructed images using a Hertzian-dipole model of the GPR antennas.

5.1 Inversion Scheme for Weak Scatterers

This section is an introduction to the inversion scheme suggested by Meincke in [25]. A fixed-offset GPR system consisting of two GPR antennas, referred to as 1 and 2, is considered in Figure 5.1. The usual rectangular xyz-coordinate system is defined with the z-axis pointing into the upper half space and the air-soil interface is at $z = 0$. The upper half space consists of air and the lower half space consists of soil with real permittivity ε_1 and permeability μ_0. A common reference point is chosen for the GPR system and it is denoted by $\mathbf{r}_A = \hat{\mathbf{x}}x_A + \hat{\mathbf{y}}y_A$. The GPR antennas are fed through a coaxial cable supporting a single TEM mode. The characteristic admittance of the cable is denoted by Y_c. A reference plane is chosen in the coaxial cable and the voltages of the incoming and outgoing wave in the reference plane of GPR antenna 1 are denoted by $V^+_{A1,\omega}$ and $V^-_{A1,\omega}$, respectively. Similarly, the voltages of GPR antenna 2 are denoted by $V^+_{A2,\omega}$ and $V^-_{A2,\omega}$.

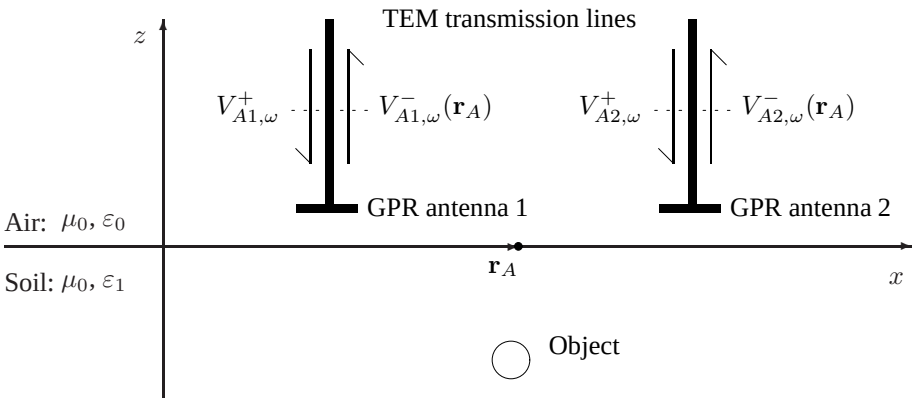

Figure 5.1: Fixed-offset GPR system with two GPR antennas 1 and 2. The position of the common reference point is denoted by $\mathbf{r}_A$.

The scattering parameters of the system in Figure 5.1 are defined as

$$S_{A11,\omega}(\mathbf{r}_A) = \left.\frac{V^-_{A1,\omega}(\mathbf{r}_A)}{V^+_{A1,\omega}}\right|_{V^+_{A2,\omega}=0}, \quad S_{A22,\omega}(\mathbf{r}_A) = \left.\frac{V^-_{A2,\omega}(\mathbf{r}_A)}{V^+_{A2,\omega}}\right|_{V^+_{A1,\omega}=0}, \tag{5.1}$$

$$S_{A21,\omega}(\mathbf{r}_A) = \left.\frac{V^-_{A2,\omega}(\mathbf{r}_A)}{V^+_{A1,\omega}}\right|_{V^+_{A2,\omega}=0}, \quad S_{A12,\omega}(\mathbf{r}_A) = \left.\frac{V^-_{A1,\omega}(\mathbf{r}_A)}{V^+_{A2,\omega}}\right|_{V^+_{A1,\omega}=0},$$

where $S_{A12,\omega} = S_{A21,\omega}$ since the system is reciprocal. The scattering parameters for the configuration without any objects are denoted by

$$\begin{aligned} \Gamma_{A11,\omega} &= S_{A11,\omega}|_{\text{no objects}}, \quad \Gamma_{A22,\omega} = S_{A22,\omega}|_{\text{no objects}}, \\ \Gamma_{A21,\omega} &= S_{A21,\omega}|_{\text{no objects}}, \quad \Gamma_{A12,\omega} = S_{A12,\omega}|_{\text{no objects}}. \end{aligned} \tag{5.2}$$

The response due to the objects in the soil is calculated as

$$S_{F11,\omega}(\mathbf{r}_A) = S_{A11,\omega}(\mathbf{r}_A) - \Gamma_{A11,\omega}, \tag{5.3}$$

$$S_{F21,\omega}(\mathbf{r}_A) = S_{A21,\omega}(\mathbf{r}_A) - \Gamma_{A21,\omega}. \tag{5.4}$$

The scatterer is characterized by the difference $\Delta\varepsilon_\omega$ between permittivity $\varepsilon_{\text{sca},\omega}$ of the scatterer and permittivity of the background medium

$$\Delta\varepsilon_\omega(\mathbf{r}') = \varepsilon_{\text{sca},\omega}(\mathbf{r}') - \varepsilon_1. \tag{5.5}$$

The Fourier-transformed scattering parameters are defined as

$$\widetilde{S}_{F11,\omega}(k_x,k_y)=\iint_{-\infty}^{\infty}S_{F11,\omega}(\mathbf{r}_A)e^{-i[k_x x_a+k_y y_a]}dx_a dy_a, \tag{5.6}$$

$$\widetilde{S}_{F21,\omega}(k_x,k_y)=\iint_{-\infty}^{\infty}S_{F21,\omega}(\mathbf{r}_A)e^{-i[k_x x_a+k_y y_a]}dx_a dy_a. \tag{5.7}$$

Moreover, the Fourier-transformed object function is defined as

$$\widetilde{\Delta\varepsilon}_{\omega}(k_x,k_y,z')=\iint_{-\infty}^{\infty}\Delta\varepsilon_{\omega}(\mathbf{r}')e^{-i[k_x x'+k_y y']}dx'dy'. \tag{5.8}$$

If weak scatterers are considered the Born approximation can be invoked and the relation between the Fourier-transformed scattering parameters and the Fourier-transformed object function can be expressed in terms of a linear Fredholm integral equation of the first kind. If the fixed-offset GPR system is considered, the integral equation becomes

$$\widetilde{S}_{F21,\omega}(k_x,k_y)=\frac{i\omega^2\mu_0}{8\pi^2}\int_{-\infty}^{0}\widetilde{\Delta\varepsilon}_{\omega}(k_x,k_y,z')I_{21,\omega}(k_x,k_y,z')dz', \tag{5.9}$$

where the function $I_{21,\omega}$ is defined as

$$\begin{aligned}I_{21,\omega}(k_x,k_y,z')=\frac{1}{\gamma_{1,\omega}}\iint_{-\infty}^{\infty}\mathbf{R}_{A2,\omega}(k_x+k'_x,k_y+k'_y)\cdot\mathbf{T}_{A1,\omega}(k'_x,k'_y)\\ \cdot e^{-iz'[\gamma_{1,\omega}(k_x+k'_x,k_y+k'_y)+\gamma_{1,\omega}(k'_x,k'_y)]}dk'_x dk'_y.\end{aligned} \tag{5.10}$$

The integral equation in (5.9) is called the forward model. This model can be discretezised and written in the usual form $\overline{\mathbf{A}}\cdot\mathbf{x}=\mathbf{b}$ where the vector $\mathbf{x}$ is a discretization of the object function $\widetilde{\Delta\varepsilon}_{\omega}$ and the vector $\mathbf{b}$ is a discretization of the Fourier-transformed scattering parameter $\widetilde{S}_{F21,\omega}$.

The double integral in the function $I_{21,\omega}$ in (5.10) can be evaluated using the method of stationary phase if it is assumed that the scatterer is deeply buried in a lossless medium and if it is assumed that contributions from evanescent plane waves are negligible. Using these assumptions, $I_{21,\omega}$ is rewritten as

$$I_{21,\omega}(k_x,k_y,z')\sim\frac{I_{A21,\omega}(k_x,k_y)}{z'}e^{-2iz'\gamma_{1,\omega}\left(\frac{k_x}{2},\frac{k_y}{2}\right)}, \tag{5.11}$$

where

$$I_{A21,\omega}(k_x,k_y)=\frac{i\pi\gamma_{1,\omega}\left(\frac{k_x}{2},\frac{k_y}{2}\right)}{\omega z'\sqrt{\mu_0\varepsilon_1}}\mathbf{R}_{A2,\omega}\left(\frac{k_x}{2},\frac{k_y}{2}\right)\cdot\mathbf{T}_{A1,\omega}\left(-\frac{k_x}{2},-\frac{k_y}{2}\right). \tag{5.12}$$

Hence, the forward model in (5.9) takes on the following form

$$\begin{aligned}\widetilde{S}_{F21,\omega}(k_x,k_y) = \frac{i\omega^2\mu_0}{8\pi^2} I_{A21,\omega}(k_x,k_y)\cdot \\ \cdot \int_{-\infty}^{0} \frac{\widetilde{\Delta\varepsilon}_\omega(k_x,k_y,z')}{z'} e^{-2iz'\gamma_{1,\omega}\left(\frac{k_x}{2},\frac{k_y}{2}\right)} dz'.\end{aligned} \tag{5.13}$$

This expression in (5.13) can also be discretezised and written in the usual form $\overline{\mathbf{A}}\cdot\mathbf{x}=\mathbf{b}$. Furthermore, to develop analytical expressions it is assumed that the difference in the complex permittivity $\Delta\varepsilon_\omega$ can be written as the factorization $\Delta\varepsilon_\omega(\mathbf{r}') = a_\Delta(\mathbf{r}')b_{\Delta,\omega}$ where $a_\Delta(\mathbf{r}')$ is an unknown frequency-independent object function and $b_{\Delta,\omega}$ is a known frequency dependent function. From the relation $\Delta\varepsilon_\omega(\mathbf{r}) = (\Delta\varepsilon_{-\omega}(\mathbf{r}'))^*$ it is seen that the unknown frequency-independent function $a_\Delta(\mathbf{r}')$ is a purely real function.

The Fourier-transformed object function $\widetilde{a}_\Delta$ is defined as

$$\widetilde{a}_\Delta(k_x,k_y,k_z) = \iiint\limits_{z'<0} \frac{a_\Delta(\mathbf{r}')}{z'} e^{-i[k_x x'+k_y y'+k_z z']} dx'dy'dz', \tag{5.14}$$

where the spatial angular frequency k_z is a real quantity which can be both positive and negative. The object function a_Δ can be written in terms of $\widetilde{a}_\Delta$ as

$$a_\Delta(\mathbf{r}') = \frac{z'}{(2\pi)^3} \iiint_{-\infty}^{\infty} \widetilde{a}_\Delta(k_x,k_y,k_z) e^{i[k_x x'+k_y y'+k_z z']} dk_x dk_y dk_z. \tag{5.15}$$

Since the quantity $\frac{a_\Delta(\mathbf{r}')}{z'}$ is real then $\widetilde{a}_\Delta(k_x,k_y,k_z) = (\widetilde{a}_\Delta(-k_x,-k_y,-k_z))^*$ and the object function a_Δ can be rewritten as

$$a_\Delta(\mathbf{r}') = \frac{z'}{4\pi^3} \iiint\limits_{k_z>0} \widetilde{a}_\Delta(k_x,k_y,k_z) e^{i[k_x x'+k_y y'+k_z z']} dk_x dk_y dk_z. \tag{5.16}$$

Using the object function $\widetilde{a}_\Delta$ the forward model in (5.13) is expressed as

$$\widetilde{S}_{F21,\omega}(k_x,k_y) = \frac{i\omega^2\mu_0}{8\pi^2} I_{A21,\omega}(k_x,k_y) b_{\Delta,\omega} \widetilde{a}_\Delta\left(k_x,k_y,2\gamma_{1,\omega}\left(\frac{k_x}{2},\frac{k_y}{2}\right)\right). \tag{5.17}$$

The assumption that the object function $a_\Delta(\mathbf{r}')$ is frequency-independent is necessary since the object function $a_\Delta(\mathbf{r}')$ must be independent of the spatial angular frequency k_z to use the Fourier transform pair in (5.14) and (5.15). Using this Fourier transform pair an explicit expression for the object function can be found as

$$\begin{aligned}a_\Delta(\mathbf{r}') = \frac{4\varepsilon_1 z'}{\pi}\ \mathrm{Re}\Bigg[\iiint\limits_{\omega>0,\sqrt{k_x^2+k_y^2}<2\omega\sqrt{\mu_0\varepsilon_1}} \frac{1}{\gamma_{1,\omega}\left(\frac{k_x}{2},\frac{k_y}{2}\right)} \\ \cdot \frac{\widetilde{S}_{F21,\omega}(k_x,k_y)}{\omega I_{A21,\omega}(k_x,k_y) b_{\Delta,\omega}} e^{i[k_x x'+k_y y'+2\gamma_{1,\omega}\left(\frac{k_x}{2},\frac{k_y}{2}\right)z']} dk_x dk_y d\omega \Bigg].\end{aligned} \tag{5.18}$$

The fixed-offset GPR system can also be used in a zero-offset mode if GPR antennas 1 and 2 coincide. Furthermore, the inversion scheme for the zero-offset GPR system is almost identical to the inversion scheme for the fixed-offset GPR system where the explicit expression for the object function is given by

$$a_{\Delta}(\mathbf{r}') = \frac{4\varepsilon_1 z'}{\pi}\ \mathrm{Re}\left[\iiint\limits_{\omega>0,\sqrt{k_x^2+k_y^2}<2\omega\sqrt{\mu_0\varepsilon_1}} \frac{1}{\gamma_{1,\omega}\left(\frac{k_x}{2},\frac{k_y}{2}\right)}\ \frac{\widetilde{S}_{F11,\omega}(k_x,k_y)}{\omega I_{A11,\omega}(k_x,k_y)b_{\Delta,\omega}} e^{i[k_x x'+k_y y'+2\gamma_{1,\omega}\left(\frac{k_x}{2},\frac{k_y}{2}\right)z']}dk_x dk_y d\omega\right], \tag{5.19}$$

where

$$I_{A11,\omega}(k_x,k_y) = \frac{i\pi\gamma_{1,\omega}\left(\frac{k_x}{2},\frac{k_y}{2}\right)}{\omega z'\sqrt{\mu_0\varepsilon_1}}\mathbf{R}_{A1,\omega}\left(\frac{k_x}{2},\frac{k_y}{2}\right)\cdot\mathbf{T}_{A1,\omega}\left(-\frac{k_x}{2},-\frac{k_y}{2}\right). \tag{5.20}$$

The integrations in (5.18) and (5.19) over the Fourier representation of the object function $\widetilde{a}_{\Delta}(k_x,k_y,k_z)$ are limited to a spherical shell given by

$$4\omega_{min}^2\mu_0\varepsilon_1 \le k_x^2+k_y^2+k_z^2 \le 4\omega_{max}^2\mu_0\varepsilon_1, \tag{5.21}$$

and the resolution is determined by

$$\Delta x = \Delta y = \Delta z = \frac{c_1}{4f_{max}} = \frac{c_1}{2B}, \tag{5.22}$$

where $c_1 = 1/\sqrt{\mu_0\varepsilon_1}$ is the velocity of propagation in the soil and $B = 2f_{max}$ is the bandwidth. However, the attenuation of the evanescent plane waves in the air between the GPR antenna and the air-soil interface often make these plane waves useless for imaging. If evanescent plane waves in air are negligible then the integrations in (5.18) and (5.19) reduce to an elliptical shell given by

$$4\omega_{min}^2\mu_0\varepsilon_1 \le (k_x^2+k_y^2)\frac{\varepsilon_1}{\varepsilon_0}+k_z^2 \le 4\omega_{max}^2\mu_0\varepsilon_1, \tag{5.23}$$

and the resolution is given by

$$\Delta x = \Delta y = \frac{c_0}{4f_{max}} = \frac{c_0}{2B}, \tag{5.24}$$

$$\Delta z = \frac{c_1}{4f_{max}} = \frac{c_1}{2B}, \tag{5.25}$$

where $c_0 = 1/\sqrt{\mu_0 \varepsilon_0}$ is the velocity of propagation in free space. This observation agrees with the result obtained by Van der Kruk in [79], [80] and Hansen and Meincke in [81]. In [80] Van der Kruk concludes that the GPR should be as close to the air-soil interface as possible to obtain a high-resolution image since this location optimizes the spatial bandwidth. The drawback of a position of the GPR antennas close to the air-soil interface is higher sensitivity of the plane-wave transmitting and receiving spectra to fluctuations in the properties of the soil.

5.2 Methods for Pre-Processing

Reflections from the air-soil interface are removed in the pre-processing. In this thesis the air-soil interface is considered as an integrated part of the GPR antenna so removal of reflections from the GPR antenna is also ground bound removal [82]. If the reflection coefficient $S_{A11,\omega}$ is Fourier-transformed a peak will appear at $(k_x, k_y) = (0, 0)$. Data for the point $(k_x, k_y) = (0, 0)$ is substituted by an interpolated value using the data in the neighborhood and an inverse Fourier transform is performed. The new set of data is denoted as $S_{F11,\omega}$.

To limit the errors due to the finite scan plane the data $S_{F11,\omega}$ is multiplied with a two-dimensional window function. The two-dimensional window function is written as the product

$$W_{xy}(x_A, y_A) = W_x(x_A) W_y(y_A), \tag{5.26}$$

between the cosine roll-off window functions

$$W_x(x_A) = \begin{cases} 1 & , x_{A,min} + d < x_A < x_{A,max} - d, \\ \frac{1}{2} + \frac{1}{2}\cos\left(\frac{x_A - x_{A,min} - d}{d\pi}\right) & , x_{A,min} < x_A < x_{A,min} + d, \\ \frac{1}{2} + \frac{1}{2}\cos\left(\frac{x_A - x_{A,max} + d}{d\pi}\right) & , x_{A,max} - d < x_A < x_{A,max}, \\ 0 & , \text{ otherwise,} \end{cases} \tag{5.27}$$

$$W_y(y_A) = \begin{cases} 1 & , y_{A,min} + d < y_A < y_{A,max} - d, \\ \frac{1}{2} + \frac{1}{2}\cos\left(\frac{y_A - y_{A,min} - d}{d}\pi\right) & , y_{A,min} < y_A < y_{A,min} + d, \\ \frac{1}{2} + \frac{1}{2}\cos\left(\frac{y_A - y_{A,max} + d}{d}\pi\right) & , y_{A,max} - d < y_A < y_{A,max}, \\ 0 & , \text{ otherwise,} \end{cases} \tag{5.28}$$

where the subscript max and min denotes maximum and minimum, respectively. The parameter d has been chosen to $d = 30$ cm and the size of the scan is $y_{A,max} - y_{A,min} = x_{A,max} - x_{A,min} = 1.890$ m.

5.3 Image Reconstruction of a Plastic Pipe

The measured bowtie antenna and the equiangular planar spiral antenna in Chapter 4 is used for imaging using the results from Section 5.1. The bowtie is used for imaging in moist soil whereas the equiangular planar spiral antenna is used for imaging in dry soil. The constructed images using the plane-wave transmitting spectrum is compared with the imaging procedure as suggested in [24] where the GPR antennas are modelled as simple Hertzian-dipoles.

The bowtie antenna is used for imaging of a plastic pipe filled with water as shown in Figures 5.2 and 5.3. The pipe was buried immediately after the measurements of the plane-wave transmitting spectrum of the bowtie antenna. It is assumed that the properties of the loam are unchanged so the constitutive parameters are still given by the relative permittivity $\varepsilon_1/\varepsilon_0 = 7.80$ and the conductivity $\sigma_\omega = a_c f$ with the slope $a_c = 51$ mS/m/GHz. The plastic pipe has an outer diameter of 40 mm and an inner diameter of 35 mm. The lower and upper parts of the pipe are at the distances 20.3 cm and 16.3 cm from the air-soil interface, respectively. The distance 16.3 cm is equal to 1.5 wavelength at the frequency 1 GHz. The short distance makes the imaging more difficult since the method in [24, 75] is based on an asymptotic expression that is valid for objects buried at a large distance from the air-soil interface. The pipe cannot be considered as a weak scatterer since the relative permittivity of water is approximately 80 and the loam has a relative permittivity of 7.80.

5.3.1 Application of BowTie Antenna

The bowtie antenna is used in a zero-offset configuration and the measured plane-wave transmitting spectrum in Chapter 4 is used for calculation of the object function given by

$$B_{Zero-Offset}(\mathbf{r}') = \frac{4\varepsilon_1|z'|}{\pi} \left| \iiint\limits_{\omega>0,\sqrt{k_x^2+k_y^2}<2\omega\sqrt{\mu_0\varepsilon_1}} \frac{1}{\gamma_{1,\omega}\left(\frac{k_x}{2},\frac{k_y}{2}\right)} \cdot \frac{\widetilde{S}_{F11,\omega}(k_x,k_y)}{\omega I_{A11,\omega}(k_x,k_y) b_\omega} e^{i[k_x x' + k_y y' + 2\gamma_{1,\omega}\left(\frac{k_x}{2},\frac{k_y}{2}\right) z']} dk_x dk_y d\omega \right|, \tag{5.29}$$

which is a modification of the object function in (5.19). Only the measured plane-wave spectrum in the region for propagating plane waves $k_x^2 + k_y^2 < \omega^2\mu_0\varepsilon_0$ is used since no improvement of the image quality is achieved by including the region $\omega^2\mu_0\varepsilon_0 < k_x^2 + k_y^2 < \omega^2\mu_0\varepsilon_1$. Losses in the loam are not included in the imaging procedure so the maximum values of the object function are expected to roll off quite rapidly as a function of depth.

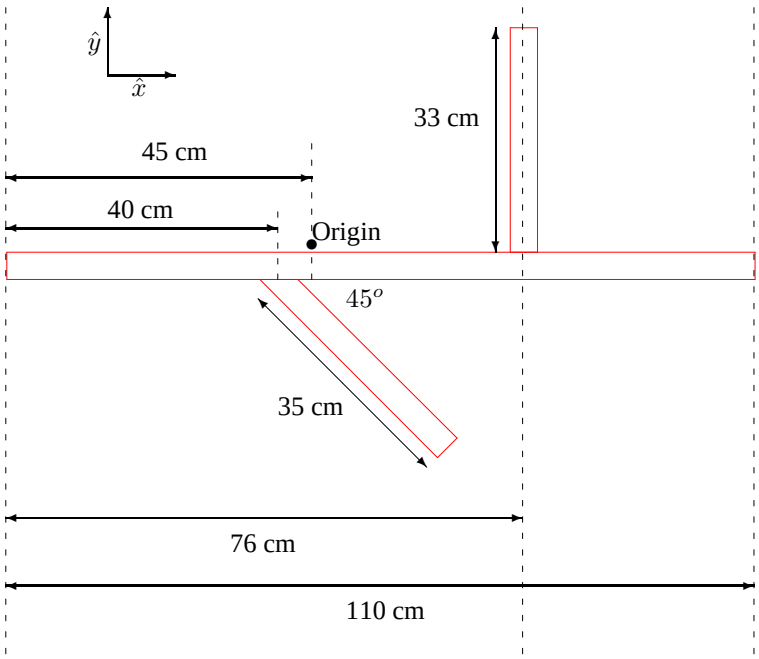

Figure 5.2: The geometry and position of the pipe in the moist loam.

Figure 5.3: Picture of the pipe from Figure 5.2.

Using the object function (5.29) a three-dimensional image in the region 1.8 m $\times$ 1.8 m $\times$ 0.5 m is constructed using frequencies from 0.5 GHz to 1.6 GHz. The time of calculation is measured in seconds on a standard PC. Using the colorbar in Figure 5.4 the value of the object function is plotted as a function of (x, y) in Figure 5.5. The position of the plastic pipe agrees with the position in Figure 5.2. In Figure 5.6 the object function is plotted as a function of (y, z). The center of the object is below $z = -14.5$ cm. The plastic tube with water is not a weak scatterer and the quantitative method in Section 5.1 prescribe. The large values of the object function below $z = -20.3$ cm may be caused by the fact that the plastic with water not is a weak scatterer.

To compare the method in (5.29) with methods, where no information about the PWTS is used, an image reconstruction based on a Hertzian-dipole model of the GPR antenna is performed [24]. The bowtie antenna is approximated as a Hertzian-dipole with a polarization parallel to the unit vector $\hat{\mathbf{x}}$ at the height $z = 10$ cm. In Figures 5.7 and 5.8 the value of the object function is plotted as a function of (x, y) and (y, z), respectively. For this particular case, image reconstruction using the PWTS in (5.29) do not reveal further information about the shape and position of the plastic tube compared to the method in [24] based on a Hertzian-dipole model of the GPR antenna.

An echogram is constructed by a Fourier transform of $S_{F11,\omega}$ from the frequency-domain to the time-domain and plotted as a function of (x, y) and (y, t) in Figures 5.9 and 5.10, respectively. For the bowtie antenna an echogram reveals information about the shape and position of the plastic pipe. Furthermore, a long time-response of the plastic pipe is visible.

Figure 5.4: The colorbar applied in subsequent Figures 5.5-5.16.

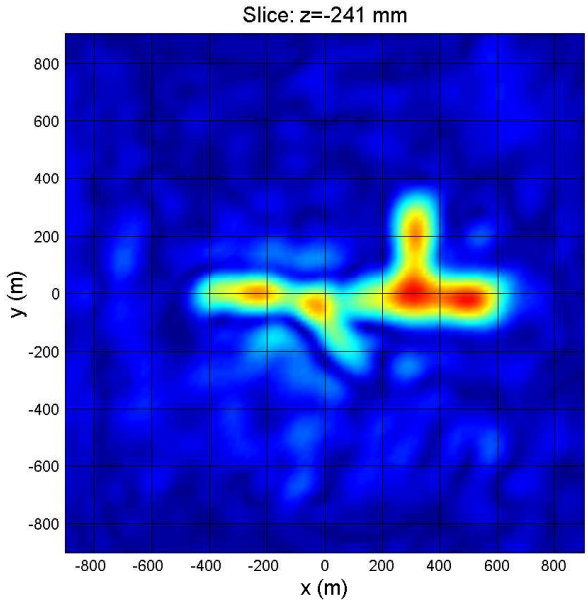

Figure 5.5: Values of the object function in (5.29) using PWTS of the bowtie antenna. The plastic pipe is buried in moist loam as shown in Figure 5.2. Frequencies in the range from 0.5 GHz to 1.6 GHz are used.

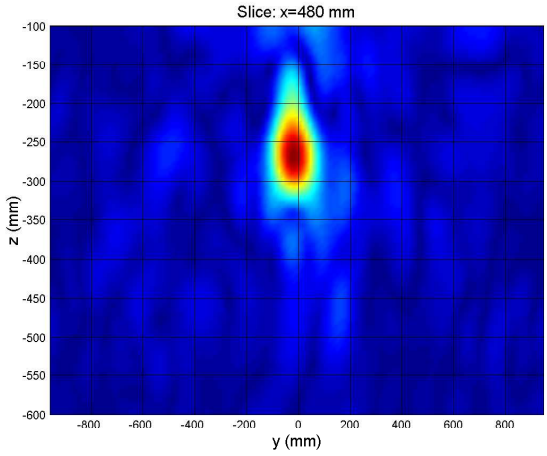

Figure 5.6: Values of the object function in (5.29) using PWTS of the bowtie antenna. The plastic pipe is buried in moist loam as shown in Figure 5.2. Frequencies in the range from 0.5 GHz to 1.6 GHz are used.

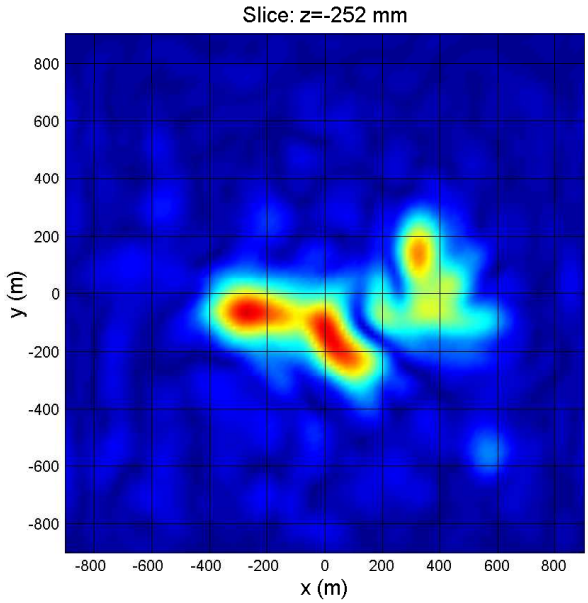

Figure 5.7: Values of the object function using the Hertzian-dipole model of the bowtie antenna as suggested in [24]. Frequencies in the range from 0.5 GHz to 1.6 GHz are used.

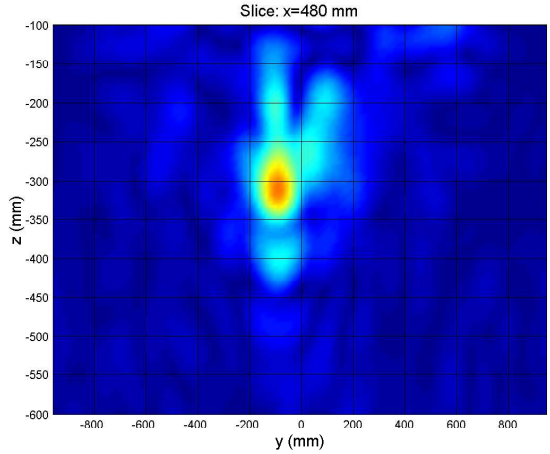

Figure 5.8: Values of the object function using the Hertzian-dipole model of the bowtie antenna as suggested in [24]. Frequencies in the range from 0.5 GHz to 1.6 GHz are used.

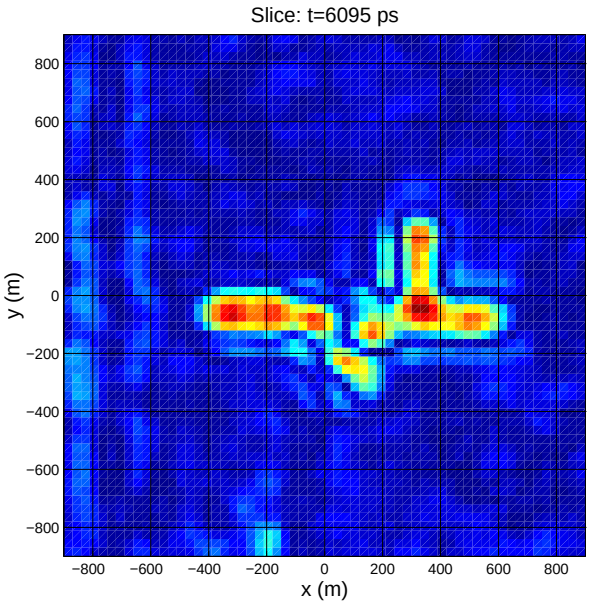

Figure 5.9: Horizontal slice of an echogram for data collected using the bowtie antenna.

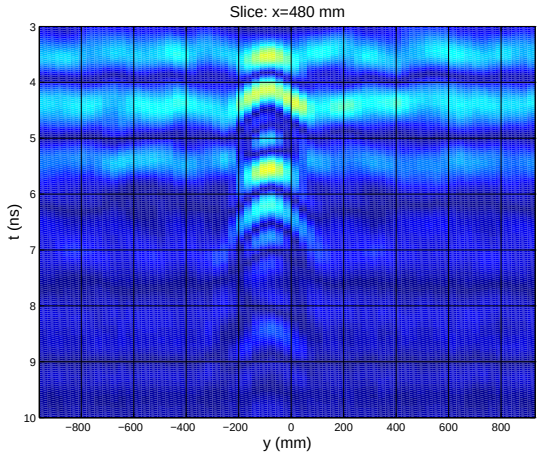

Figure 5.10: Vertical slice of an echogram for data collected using the bowtie antenna.

5.3.2 Application of Equiangular Planar Spiral Antenna

The equiangular planar spiral antenna is used for detection of the plastic pipe in dry loam with the relative permittivity $\varepsilon_1/\varepsilon_0 = 3.6$. The plastic pipe is buried so that the lower part is 30 cm below the air-soil interface. The spiral antenna is used in a fixed-offset configuration and the measured plane-wave transmitting spectrum in Chapter 4 is used for calculation of the object function given by

$$B_{Fixed-offset}(\mathbf{r}') = \frac{4\varepsilon_1|z'|}{\pi}\,\mathrm{Re}\left|\iiint\limits_{\omega>0,\sqrt{k_x^2+k_y^2}<2\omega\sqrt{\mu_0\varepsilon_1}} \frac{1}{\gamma_{1,\omega}\left(\frac{k_x}{2},\frac{k_y}{2}\right)} \cdot\frac{\widetilde{S}_{F21,\omega}(k_x,k_y,z_A)}{\omega I_{A21,\omega}(k_x,k_y)b_\omega} e^{i[k_x x'+k_y y'+2\gamma_{1,\omega}\left(\frac{k_x}{2},\frac{k_y}{2}\right)z']} dk_x dk_y d\omega\right|. \tag{5.30}$$

which is a modification of the object function in (5.18). Only the measured plane-wave spectrum in the region for propagating plane waves is used. A three-dimension image in the region 1.8 m $\times$ 1.8 m $\times$ 0.5 m is calculated using frequencies in the range from 0.6 GHz to 1.5 GHz. Again, the time of calculation is measured in seconds using a standard PC. The value of the object function is plotted as function of (x, y) and (y, z) in Figures 5.11 and 5.12, respectively. A good image is constructed of the plastic pipe and it is concluded that a broadband dispersive GPR antenna as the equiangular planar spiral antenna is just as useful as a traditional non-dispersive linearly polarized GPR antenna when the new imaging method is applied. The image reconstruction using the method in (5.30) is compared with image construction using a simple Hertzian-dipole model. The equiangular spiral antenna is approximated as two Hertzian-dipoles with a polarization parallel to the unit vector $\hat{\mathbf{x}}$ at the height $z = 15$ cm. The value of the object function is plotted as function of (x, y) and (y, t) in Figures 5.13 and 5.14, respectively. The shape of the plastic pipe is badly revealed hence the quality of the reconstructed images is very improved by use of the PWTS.

An echogram is constructed by a Fourier transform of $S_{F21,\omega}$ from the frequency-domain to the time-domain and plotted as a function of (x, y) and (y, t) in Figures 5.15 and 5.16, respectively. Similarly, like the image reconstruction using the Hertzian dipole model the shape of the plastic pipe is badly revealed hence the quality of the reconstructed images is very improved by use of the PWTS.

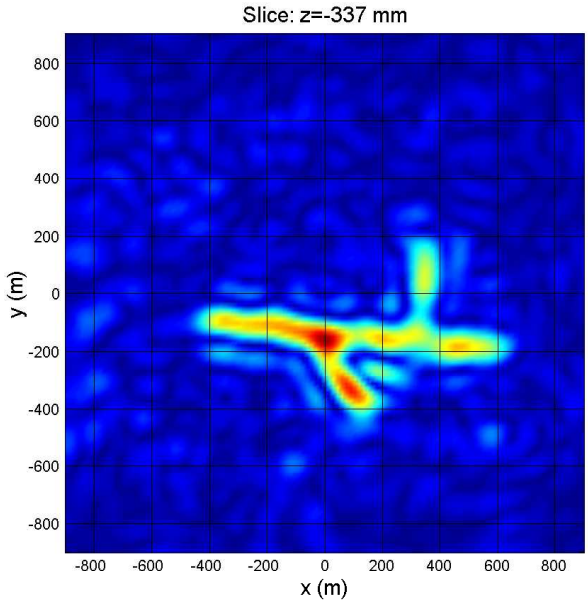

Figure 5.11: Values of the object function in (5.30) using PWTS of the equiangular planar spiral antenna. The plastic pipe containing water is buried in dry loam. Frequencies in the range from 0.6 GHz to 1.5 GHz are used.

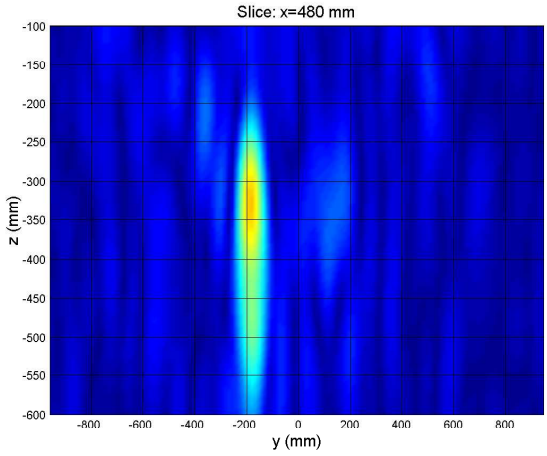

Figure 5.12: Values of the object function in (5.30) using PWTS of the equiangular planar spiral antenna. The plastic pipe containing water is buried in dry loam. Frequencies in the range from 0.6 GHz to 1.5 GHz are used.

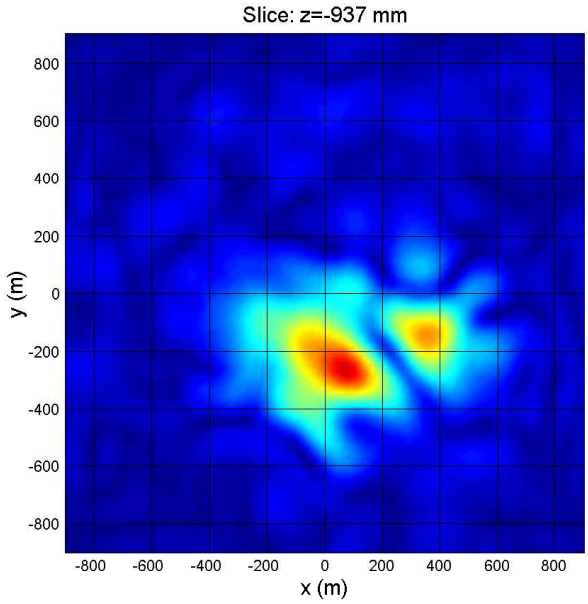

Figure 5.13: Values of the object function using the Hertzian-dipole model of the spiral antenna as suggested in [24]. Frequencies in the range from 0.6 GHz to 1.5 GHz are used.

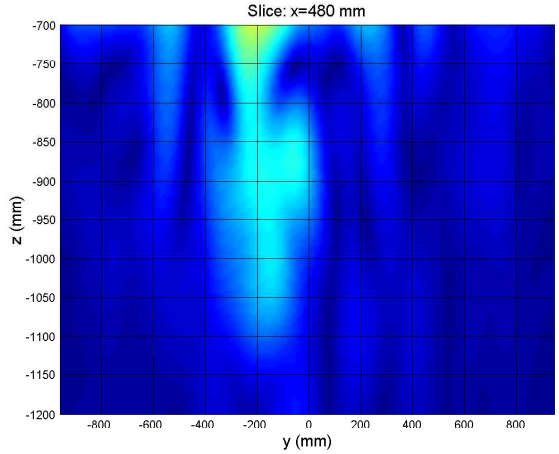

Figure 5.14: Values of the object function using the Hertzian-dipole model of the spiral antenna as suggested in [24]. Frequencies in the range from 0.6 GHz to 1.5 GHz are used.

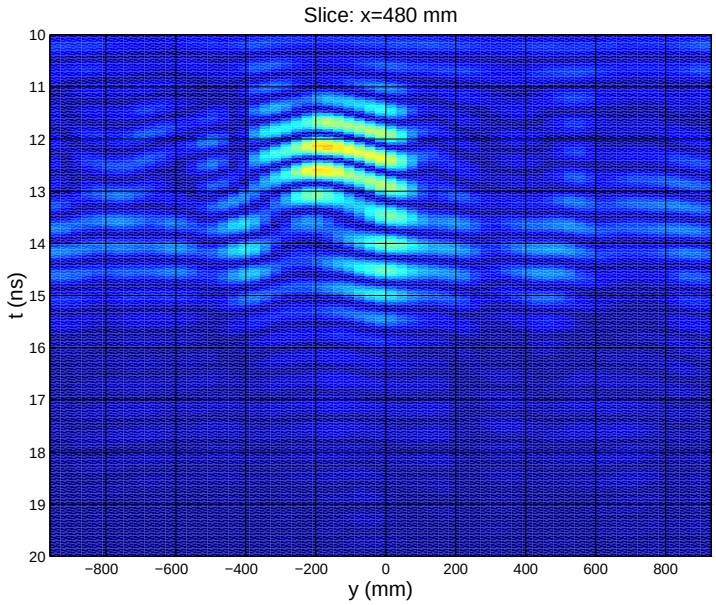

Figure 5.15: Horizontal slice of an echogram for data collected using the bowtie antenna.

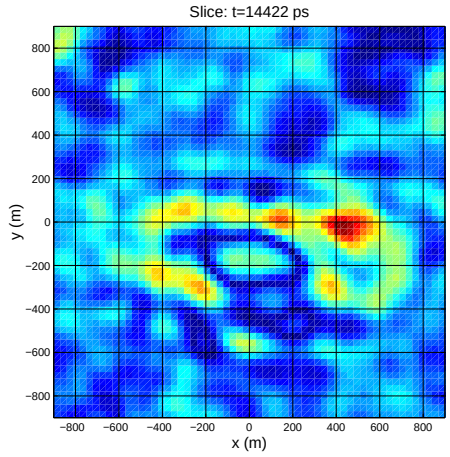

Figure 5.16: Vertical slice of an echogram for data collected using the bowtie antenna.

5.4 Summary

Image reconstruction using the PWTS of the GPR antennas is performed using the procedure developed by Meincke in [25]. In this method a frequency-independent object function is estimated which is defined as the difference between the complex permittivity of the scatterer and the permittivity of the background medium. This object function is modified and used for qualitative imaging of a plastic pipe buried in loam.

For the non-dispersive linearly polarized bowtie antenna knowledge about the PWTS is not necessary in the imaging procedure. A simple Hertzian-dipole model can be used for construction of images that reveals the shape and location of the object buried in loam as suggested by Meincke and Hansen in [22]. For a dispersive broadband equiangular planar spiral antenna knowledge about the antenna should be included as a measured foot print or as a PWTS. Measured foot prints are used by Van Dongen et al. in [77] and a measured PWTS is used in this thesis. It appears that spiral antennas are just as useful as non-dispersive linearly polarized GPR antenna if the radiation properties of the spiral antenna are properly included.

Chapter 6

Conclusions

In this thesis various aspects of planar near-field measurements of GPR antennas have been investigated. The purpose of the measurements is to include information about the GPR antennas in the imaging reconstruction and in that way extend the usable types of antennas for GPR systems.

In Chapter 2 the radiated electromagnetic field by an antenna in free space is written as an expansion of plane waves. Hence, the antenna can be characterized by a plane-wave transmitting spectrum (PWTS). This method can also be used for description of the radiated electromagnetic field in homogeneous soil by a GPR antenna close to a planar air-soil interface. The air-soil interface is considered as an integrated part of the GPR antenna and the radiated electromagnetic field in the soil is written as an expansion of plane waves. Similarly, the GPR antenna can be characterized by a plane-wave transmitting spectrum. The PWTS can be used for an accurate calculation of the radiated electromagnetic field at any position below the air-soil interface. To describe some important properties of the near field new antenna parameters are defined. These antenna parameters concern the power transmission through the air-soil interface and the polarization of the electric field tangential to the air-soil interface. Based on the plane-wave theory a measurement procedure of the PWTS is suggested. In this measurement procedure the radiated electromagnetic field is measured in the soil using a buried antenna. The plane-wave transmitting spectrum is calculated by solving a matrix equation and a parameter for evaluation of the solvability of the matrix equation is defined.

Loop antennas buried in the soil are used for measurements of the radiated electromagnetic field by the GPR antenna. The loop antenna is constructed of coaxial cable with an excitation cut. In Chapter 3 the model of the loop antenna is composed of two submodels that describe the transmission through the coaxial cable to the excitation cut and the outer surface of the loop antenna, respectively. Methods for estimation of the model parameters are developed. The constitutive parameters of the soil surrounding the loop antenna are considered as model parameters for the loop antenna and two methods for estimation of the constitutive parameters are suggested. In the first

method constitutive parameters are estimated using the measured admittance of the loop. The estimation is performed by a comparison between the measured admittance and a calculated admittance using a model of the loop. In the second method constitutive parameters are estimated using measurements of the voltage transfer function between the buried loop and a known GPR antenna. The estimation is also based on a comparison between the measured voltage transfer function and a calculated voltage transfer function using a model of the system. The second method has appeared to be good for estimation of constitutive parameters for moist loam where the frequency dependence is unknown. The estimated constitutive parameters are compared with calculated constitutive parameters for silty clay using a four component-model as suggested by Mironov et al. in [58]. The estimated complex permittivity for the moist loam appeared to be typical.

In Chapter 4 the measurement technique of the GPR antennas is described and successfully tested on a loop antenna above the air-soil interface with a known PWTS. The test shows that reasonable measurements of the PWTS for propagating plane waves in free space can be performed. The plane-wave transmitting spectra are measured for a bowtie antenna and an equiangular planar spiral antenna, respectively. The antenna parameters defined in Chapter 2 are calculated and these parameters reveal the polarization of the electric field tangential to the air-soil interface.

The measured plane-wave transmitting spectra are used for image reconstruction in Chapter 5. Explicit knowledge about the PWTS of the bowtie antenna is not necessary since a good image reconstruction can be obtained using a Hertzian dipole model as suggested by Meincke and Hansen in [22]. However, for dispersive antennas like the equiangular planar spiral antenna it is necessary to include the electromagnetic properties of the GPR antenna. This can be done using foot prints as suggested by Dongen et al. in [77] or using the PWTS as suggested by Meincke in [25]. In this thesis the PWTS is measured for the bowtie antenna as designed by Eide in [23] and the equiangular planar spiral antenna. Image reconstruction is performed using the PWTS for both antennas and these images appear to reveal the shape and position of a buried plastic pipe. Therefore, dispersive broad antennas can be used as GPR antenna if the PWTS is included in the image reconstruction.

In this thesis only data for one polarization of the transmitter and receiver antenna is used in the image reconstruction. In future work development of a technique for image reconstruction based on plane-wave theory and a full-polarimetric data set is desirable. Another topic of interest is inclusion of PWTS in inversion schemes that can reveal quantitatively knowledge about the complex permittivity of high-contrast objects.

Appendix A

The Phasor and Frequency-Domain Formulation

The phasor- and frequency-domain formulation is defined in the following Sections A.1 and A.2 as in [35]. The time-domain Maxwell's equations are written as

$$\nabla \times \mathbf{E}(\mathbf{r},t) = -\frac{\partial \mathbf{B}(\mathbf{r},t)}{\partial t}, \tag{A.1}$$

$$\nabla \times \mathbf{H}(\mathbf{r},t) = \frac{\partial \mathbf{D}(\mathbf{r},t)}{\partial t} + \mathbf{J}(\mathbf{r},t), \tag{A.2}$$

$$\nabla \cdot \mathbf{B}(\mathbf{r},t) = 0, \tag{A.3}$$

$$\nabla \cdot \mathbf{D}(\mathbf{r},t) = \rho(\mathbf{r},t), \tag{A.4}$$

with the constitutive relations [83]

$$\mathbf{B}(\mathbf{r},t) = \mu_0 \left(\mathbf{H}(\mathbf{r},t) + \frac{1}{2\pi} \int_{-\infty}^{\infty} \chi_m \left(\mathbf{r}, t-t'\right) \mathbf{H}(\mathbf{r},t') dt' \right), \tag{A.5}$$

$$\mathbf{D}(\mathbf{r},t) = \varepsilon_0 \left(\mathbf{E}(\mathbf{r},t) + \frac{1}{2\pi} \int_{-\infty}^{\infty} \chi_e \left(\mathbf{r}, t-t'\right) \mathbf{E}(\mathbf{r},t') dt' \right), \tag{A.6}$$

$$\mathbf{J}(\mathbf{r},t) = \sigma(\mathbf{r}) \mathbf{E}(\mathbf{r},t), \tag{A.7}$$

where the conductivity is denoted by σ and the magnetic and electric susceptibility are denoted by χ_m and χ_e, respectively. Causality demands that $\chi_m = 0$ and $\chi_e = 0$ for $t < 0$. Only real fields and charge densities are considered in the time-domain. In Figure A.1 a monostatic GPR system is considered. The incident and reflected voltage pulse in the reference plane are denoted by V_A^+ and V_A^-, respectively. The position of the reference point for the GPR system is denoted by $\mathbf{r}_A$.

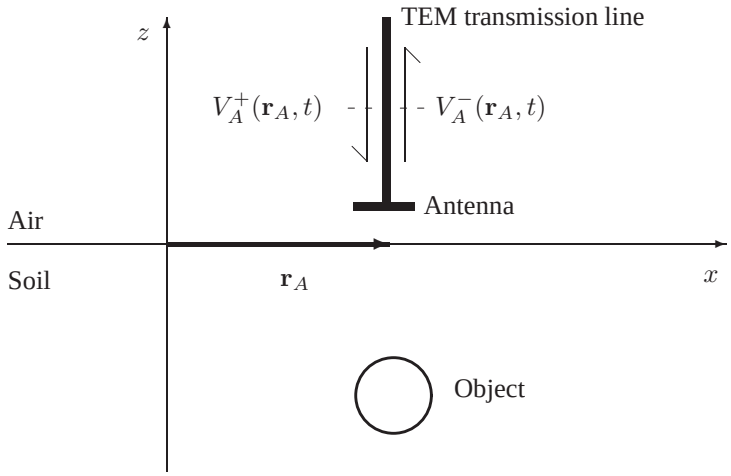

Figure A.1: Reflection measurement in a monostatic GPR system. The time-domain notation has been used.

A.1 Phasor Formulation

Sinusoidal time-domain variations can be described using complex field amplitudes. In the phasor formulation the electric field is written as a product between the complex amplitude $\mathbf{E}$ and the time factor $e^{-i\omega t}$. The time independent complex amplitude $\mathbf{E}$ is denoted a phasor. The time-domain $\mathbf{E}$-field is

$$\mathbf{E}(\mathbf{r}, t) = \text{ Re}[\mathbf{E}(\mathbf{r}, \omega)e^{-i\omega t}], \quad \omega > 0. \tag{A.8}$$

where only positive frequencies are considered. Using the phasor formulation Maxwell's equations are written as

$$\nabla \times \mathbf{E}(\mathbf{r}, \omega) = i\omega\mathbf{B}(\mathbf{r}, \omega), \tag{A.9}$$
$$\nabla \times \mathbf{H}(\mathbf{r}, \omega) = -i\omega\mathbf{D}(\mathbf{r}, \omega) + \mathbf{J}(\mathbf{r}, \omega), \tag{A.10}$$
$$\nabla \cdot \mathbf{B}(\mathbf{r}, \omega) = 0, \tag{A.11}$$
$$\nabla \cdot \mathbf{D}(\mathbf{r}, \omega) = \rho(\mathbf{r}, \omega). \tag{A.12}$$

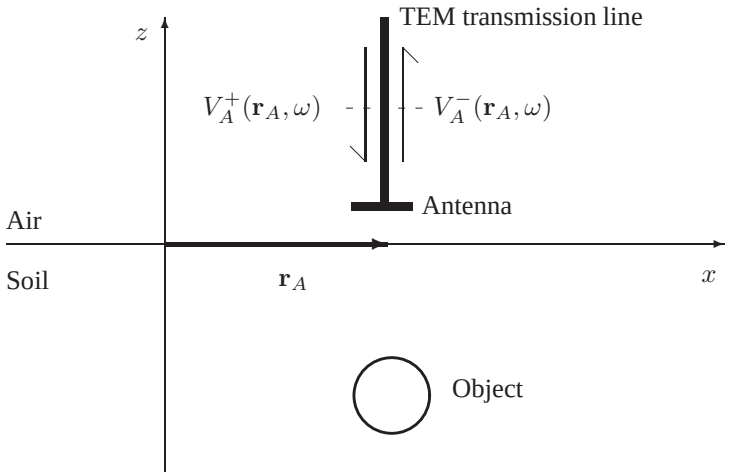

Figure A.2: Reflection measurement in a monostatic GPR system. The phasor formulation has been used.

Using the phasor notation the reflection coefficient is defined as

$$S_{AA}(\mathbf{r}_A,\omega) = \frac{V_A^-(\mathbf{r}_A,\omega)}{V_A^+(\mathbf{r}_A,\omega)}, \quad \omega > 0, \tag{A.13}$$

where V_A^+ and V_A^- are the incident and reflected voltage wave in the reference plane as defined in Figure A.2.

A.2 Frequency-Domain Formulation

The frequency-domain formulation is obtained if Maxwell's equations in (A.1-A.4) are Fourier transformed

$$\nabla \times \mathbf{E}_\omega(\mathbf{r}) = i\omega \mathbf{B}_\omega(\mathbf{r}), \tag{A.14}$$
$$\nabla \times \mathbf{H}_\omega(\mathbf{r}) = -i\omega \mathbf{D}_\omega(\mathbf{r}) + \mathbf{J}_\omega(\mathbf{r}), \tag{A.15}$$
$$\nabla \cdot \mathbf{B}_\omega(\mathbf{r}) = 0, \tag{A.16}$$
$$\nabla \cdot \mathbf{D}_\omega(\mathbf{r}) = \rho_\omega(\mathbf{r}), \tag{A.17}$$

where the Fourier transform pair is defined as

$$\mathbf{E}_\omega(\mathbf{r}) = \frac{1}{2\pi}\int_{-\infty}^{\infty} \mathbf{E}(\mathbf{r},t) e^{i\omega t} dt, \tag{A.18}$$
$$\mathbf{E}(\mathbf{r},t) = \int_{-\infty}^{\infty} \mathbf{E}_\omega(\mathbf{r}) e^{-i\omega t} d\omega. \tag{A.19}$$

Since $\mathrm{Im}[\mathbf{E}(\mathbf{r},t)] = \mathbf{0}$, it is seen from (A.18) that

$$\mathbf{E}_{-\omega}(\mathbf{r}) = (\mathbf{E}_{\omega}(\mathbf{r}))^{*}. \tag{A.20}$$

The constitutive relations are written as

$$\mathbf{B}_{\omega}(\mathbf{r}) = \mu_0(1+\chi_{m\,\omega}(\mathbf{r}))\mathbf{H}_{\omega}(\mathbf{r}), \tag{A.21}$$
$$\mathbf{D}_{\omega}(\mathbf{r}) = \varepsilon_0(1+\chi_{e\,\omega}(\mathbf{r}))\mathbf{E}_{\omega}(\mathbf{r}), \tag{A.22}$$
$$\mathbf{J}_{\omega}(\mathbf{r}) = \sigma\mathbf{E}_{\omega}(\mathbf{r}). \tag{A.23}$$

The Fourier-transform pair of the susceptibility are defined as

$$\chi_{e\,\omega}(\mathbf{r}) = \frac{1}{2\pi}\int_{-\infty}^{\infty}\chi_e\,(\mathbf{r},t)e^{i\omega t}dt, \tag{A.24}$$
$$\chi_e\,(\mathbf{r},t) = \int_{-\infty}^{\infty}\chi_{e\,\omega}(\mathbf{r})e^{-i\omega t}d\omega, \tag{A.25}$$
$$\chi_{m\,\omega}(\mathbf{r}) = \frac{1}{2\pi}\int_{-\infty}^{\infty}\chi_m\,(\mathbf{r},t)e^{i\omega t}dt, \tag{A.26}$$
$$\chi_m\,(\mathbf{r},t) = \int_{-\infty}^{\infty}\chi_{m\,\omega}(\mathbf{r})e^{-i\omega t}d\omega. \tag{A.27}$$

The permeability and permittivity can be written as

$$\mu_{\omega}(\mathbf{r}) = \mu_0(1+\chi_{m\,\omega}(\mathbf{r})), \tag{A.28}$$
$$\varepsilon_{\omega}(\mathbf{r}) = \varepsilon_0(1+\chi_{e\,\omega}(\mathbf{r})), \tag{A.29}$$

and since $\mathrm{Im}[\chi_e\,(\mathbf{r},t)] = 0$ and $\mathrm{Im}[\chi_m\,(\mathbf{r},t)] = 0$ then

$$\chi_{e\,\omega}(\mathbf{r}) = (\chi_{e\,-\omega}(\mathbf{r}))^{*}, \tag{A.30}$$
$$\varepsilon_{\omega}(\mathbf{r}) = (\varepsilon_{-\omega}(\mathbf{r}))^{*}, \tag{A.31}$$
$$\chi_{m\,\omega}(\mathbf{r}) = (\chi_{m\,-\omega}(\mathbf{r}))^{*}, \tag{A.32}$$
$$\mu_{\omega}(\mathbf{r}) = (\mu_{-\omega}(\mathbf{r}))^{*}. \tag{A.33}$$

The real and imaginary parts of the permittivity and permeability are also denoted as

$$\varepsilon_{\omega}(\mathbf{r}) = \varepsilon'_{\omega}(\mathbf{r}) + i\varepsilon''_{\omega}(\mathbf{r}), \tag{A.34}$$
$$\mu_{\omega}(\mathbf{r}) = \mu'_{\omega}(\mathbf{r}) + i\mu''_{\omega}(\mathbf{r}), \tag{A.35}$$

where ε'_{ω}, ε''_{ω}, μ'_{ω} and μ''_{ω} are real quantities. The relative permittivity and permeability are defined as

$$\varepsilon_{r,\omega}(\mathbf{r}) = \frac{\varepsilon_{\omega}(\mathbf{r})}{\varepsilon_0}, \tag{A.36}$$
$$\mu_{r,\omega}(\mathbf{r}) = \frac{\mu_{\omega}(\mathbf{r})}{\mu_0}. \tag{A.37}$$
$$\tag{A.38}$$

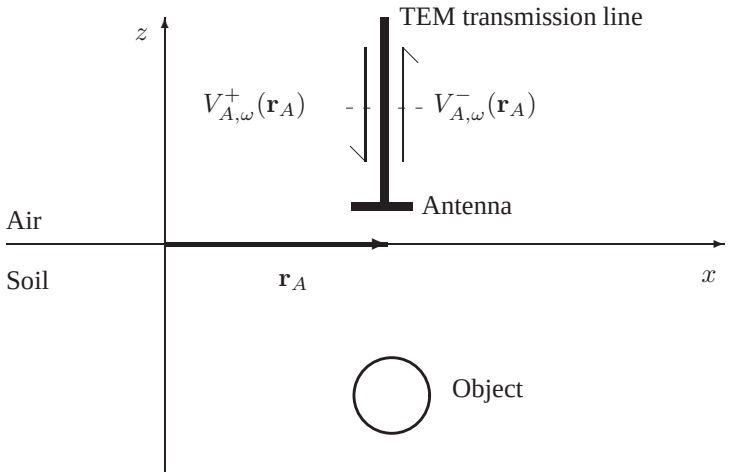

Figure A.3: Reflection measurement in a monostatic GPR system. The frequency-domain formulation has been used.

In Figure A.3 the incident and reflected voltage wave in the reference plane are denoted by $V^+_{A,\omega}$ and $V^-_{A,\omega}$. The Fourier transform pair of the voltage pulse is defined as

$$V^{\pm}_{A,\omega}(\mathbf{r}) = \frac{1}{2\pi}\int_{-\infty}^{\infty} V^{\pm}_{A}(\mathbf{r},t)e^{i\omega t}dt, \tag{A.39}$$

$$V^{\pm}_{A}(\mathbf{r},t) = \int_{-\infty}^{\infty} V^{\pm}_{A,\omega}(\mathbf{r})e^{-i\omega t}d\omega. \tag{A.40}$$

Since $\text{Im}[V^{\pm}_{A}(\mathbf{r}_A,t)] = 0$ then

$$V^{\pm}_{A,\omega}(\mathbf{r}) = (V^{\pm}_{A,-\omega}(\mathbf{r}))^*. \tag{A.41}$$

Using the frequency-domain notation the reflection coefficient is defined as

$$S_{AA,\omega}(\mathbf{r}_A) = \frac{V^-_{A,\omega}(\mathbf{r}_A)}{V^+_{A,\omega}(\mathbf{r}_A)}, \tag{A.42}$$

and in order to fullfill (A.41) then

$$S_{AA,\omega}(\mathbf{r}_A) = (S_{AA,-\omega}(\mathbf{r}_A))^*. \tag{A.43}$$

The Fourier transform in (A.40) can be written as

$$V^{\pm}_{A}(\mathbf{r}_A,t) = \int_{0}^{\infty} \text{Re}\left[2V^{\pm}_{A,\omega}(\mathbf{r}_A)e^{-i\omega t}\right] d\omega. \tag{A.44}$$

where the a pulse $V_A^{\pm}$ is written as an integration over a continuum of voltage waves $V_{A,\omega}^{\pm}$ for positive angular frequencies $\omega > 0$. For positive frequencies the reflection coefficient $S_{AA,\omega}$ in the frequency-domain formulation is equal to the reflection coefficient using the phasor formulation

$$S_{AA,\omega}(\mathbf{r}_A) = S_{AA}(\mathbf{r}_A, \omega), \quad \omega > 0. \tag{A.45}$$

Using the plane-wave theory in Chapter 2 the relation between free space magnitudes for positive and negative are given by

$$k_{0,\omega} = -k_{0,-\omega}, \tag{A.46}$$
$$\gamma_{0,\omega}(k_x, k_y) = -(\gamma_{0,-\omega}(-k_x, -k_y))^*, \tag{A.47}$$
$$\mathbf{k}_{0,\omega}^{\pm}(k_x, k_y) = -(\mathbf{k}_{0,-\omega}^{\pm}(-k_x, -k_y))^*, \tag{A.48}$$
$$\mathbf{T}_{A0,\omega}(k_x, k_y) = (\mathbf{T}_{A0,-\omega}(-k_x, -k_y))^*, \tag{A.49}$$
$$\mathbf{R}_{A0,\omega}(k_x, k_y) = (\mathbf{R}_{A0,-\omega}(-k_x, -k_y))^*, \tag{A.50}$$
$$\overline{\mathbf{S}}_{A0,\omega}(k_x, k_y, k_x', k_y') = (\overline{\mathbf{S}}_{A0,-\omega}(-k_x, -k_y, -k_x', -k_y'))^*. \tag{A.51}$$

Similarly, the magnitudes in soil is given by

$$k_{1,\omega} = -k_{1,-\omega} \tag{A.52}$$
$$\gamma_{1,\omega}(k_x, k_y) = -(\gamma_{1,-\omega}(-k_x, -k_y))^* \tag{A.53}$$
$$\mathbf{k}_{1,\omega}^{\pm}(k_x, k_y) = -(\mathbf{k}_{1,-\omega}^{\pm}(-k_x, -k_y))^* \tag{A.54}$$
$$\mathbf{T}_{A1,\omega}(k_x, k_y) = (\mathbf{T}_{A1,-\omega}(-k_x, -k_y))^*, \tag{A.55}$$
$$\mathbf{R}_{A1,\omega}(k_x, k_y) = (\mathbf{R}_{A1,-\omega}(-k_x, -k_y))^*. \tag{A.56}$$

Appendix B

Normalization of Maxwell's Equations

A PEC object in a homogeneous medium is considered. Maxwell's equations are normalized by introducing the normalized length $\mathbf{r}_N$ [84]

$$\mathbf{r}_N = \omega\sqrt{\mu_0\varepsilon'}\mathbf{r}, \tag{B.1}$$

the normalized electric field $\mathbf{E}_{N,\omega}$ and the normalize magnetic field $\mathbf{H}_{N,\omega}$

$$\mathbf{E}_{N,\omega} = \sqrt{\sqrt{\frac{\varepsilon'_\omega}{\mu_0}}}\mathbf{E}_\omega, \tag{B.2}$$

$$\mathbf{H}_{N,\omega} = \sqrt{\sqrt{\frac{\mu_0}{\varepsilon'_\omega}}}\mathbf{H}_\omega, \tag{B.3}$$

the normalized volume current density $\mathbf{J}_{N,\omega}$

$$\mathbf{J}_{N,\omega} = \frac{1}{\omega\sqrt{\mu_0\varepsilon'_\omega}}\sqrt{\sqrt{\frac{\mu_0}{\varepsilon'_\omega}}}\mathbf{J}_\omega \tag{B.4}$$

the normalized volume charge density $\rho_{N,\omega}$

$$\rho_{N,\omega} = \frac{1}{\omega\sqrt{\mu_0\varepsilon'_\omega}}\sqrt{\sqrt{\frac{\varepsilon'_\omega}{\mu_0}}\frac{\rho_\omega}{\varepsilon'_\omega}}. \tag{B.5}$$

Using the definitions in (B.1-B.5) Maxwell's equation can be written as

$$\nabla_N \times \mathbf{E}_{N,\omega} = i\mathbf{H}_{N,\omega}, \tag{B.6}$$
$$\nabla_N \times \mathbf{H}_{N,\omega} = -i\left(1 + i\tan(\delta_\omega)\right)\mathbf{E}_{N,\omega} + \mathbf{J}_{N,\omega}, \tag{B.7}$$
$$\nabla_N \cdot \mathbf{E}_{N,\omega} = \frac{\rho_{N,\omega}}{1 + i\tan(\delta_\omega)}, \tag{B.8}$$
$$\nabla_N \cdot \mathbf{H}_{N,\omega} = 0. \tag{B.9}$$

where the loss tangent $\tan(\delta_\omega)$ is defined as

$$\tan(\delta_\omega) = \frac{\omega\varepsilon''_\omega + \sigma_\omega}{\omega\varepsilon'_\omega}. \tag{B.10}$$

Similarly, the normalized surface current density $\mathbf{J}_{SN,\omega}$ is defined as

$$\mathbf{J}_{SN,\omega} = \sqrt{\sqrt{\frac{\mu_0}{\varepsilon'_\omega}}}\mathbf{J}_{S,\omega}, \tag{B.11}$$

and the surface charge density $\rho_{SN,\omega}$ is defined as

$$\rho_{SN,\omega} = \sqrt{\sqrt{\frac{\varepsilon'_\omega}{\mu_0}}}\frac{\rho_{S,\omega}}{\varepsilon'_\omega}. \tag{B.12}$$

The boundary conditions at a surface of a PEC is given by

$$\mathbf{n} \times \mathbf{E}_{N,\omega} = \mathbf{0}, \tag{B.13}$$
$$\mathbf{n} \times \mathbf{H}_{N,\omega} = \mathbf{J}_{SN,\omega}, \tag{B.14}$$
$$\mathbf{n} \cdot \mathbf{E}_{N,\omega} = \frac{\rho_{SN,\omega}}{1 - \tan(\delta_\omega)}, \tag{B.15}$$
$$\mathbf{n} \cdot \mathbf{H}_{N,\omega} = 0, \tag{B.16}$$

where the unit vector $\mathbf{n}$ is directed out of the PEC. Two cases 1 and 2 are considered where the size and geometry of the PEC are identical. From (B.1-B.16) it is seen that the normalized Maxwell equations and boundary conditions are identical if $\omega_1\sqrt{\varepsilon'_{\omega_1}} = \omega_2\sqrt{\varepsilon'_{\omega_1}}$ and $\tan(\delta_{\omega_1}) = \tan(\delta_{\omega_2})$. Since the normalized Maxwell's equations are identical the solutions can be written as a scaling of one another.

Appendix C

System Error Model for the Network Analyzer and S-parameter Test Set

This Chapter contains specifications for the network analyzer HP 8753A and the S-parameter test set HP 85046A. Further, specifications for the system configuation as shown in Figure C.1 are listed. This configuration is referred to as a typical one in the Operating and Service Manual [85, Section 3, Operation, page 3].

The desired S-parameters are defined as

$$S_{nPP,\omega} = \left.\frac{V^-_{nP,\omega}}{V^+_{nP,\omega}}\right|_{V^+_{A,\omega}=0}, \tag{C.1}$$

$$S_{AA,\omega} = \left.\frac{V^-_{A,\omega}}{V^+_{A,\omega}}\right|_{V^+_{nP,\omega}=0}, \tag{C.2}$$

$$S_{nPA,\omega} = \left.\frac{V^-_{nP,\omega}}{V^+_{A,\omega}}\right|_{V^+_{nP,\omega}=0}, \tag{C.3}$$

$$S_{nAP,\omega} = \left.\frac{V^-_{A,\omega}}{V^+_{nP,\omega}}\right|_{V^+_{A,\omega}=0}. \tag{C.4}$$

C.1 Uncertainty Equations

The suggested reflection and transmission uncertainty analysis is performed as suggested in [68]. The error model in Figure C.2 yields an equation for the reflection and

Source	
Frequency characteristics	
Range	300 kHz to 3 GHz
Accuracy (at 25^oC $\pm 5^o$C)	± 10 ppm
Resolution	1 Hz
Output power characteristics	
Range	-5 to $+20$ dBm
Resolution	0.1 dB
Level accuracy (at $+10$ dBm output level, 50 MHz	± 0.5 dB
Flatness	± 1 dB
Receiver	
Input characteristics	
Frequency range	300 kHz to 3 GHz
Impedance	50 Ω
300 kHz to 2 MHz	$>$ 20 dB return loss
2 MHz to 2 GHz	$>$ 23 dB return loss
2 GHz to 3 GHz	$>$ 20 dB return loss
Connector	50 Ω type N-female
Dynamic range	
A, B	100 dB
R	35 dB
Maximum input level	0 dBm
Damage level	20 dBm
Noise level IF BW 3 kHz (A,B)	-90 dBm
Minimum R level	-35 dBm
Input crosstalk (IF BW 10 Hz)	
300 kHz to 1 GHz	-100 dB
1 GHz to 3 GHz	-90 dB
Amplitude characteristics	
Absolute amplitude accuracy (A,B,R)	± 1 dB
Ratio accuracy	± 0.5 dB

Table C.1: Specification for the network analyzer HP 8753A.

Nominal insertion loss for the mechanical switches	300 kHz to 3 GHz
RF IN to port 1, 2	12.5 dB + 0.5 dB/GHz
RF IN to R	18 dB + 1.5 dB/GHz
RF IN to A, B	19 dB + 1.5 dB/GHz
Typical isolation between port 1 and 2	100 dB
Impedance	
Port 1, 2	50 Ω
RF IN, R, A, B	50 Ω

Table C.2: Specification for the S-parameter test set HP 85046A.

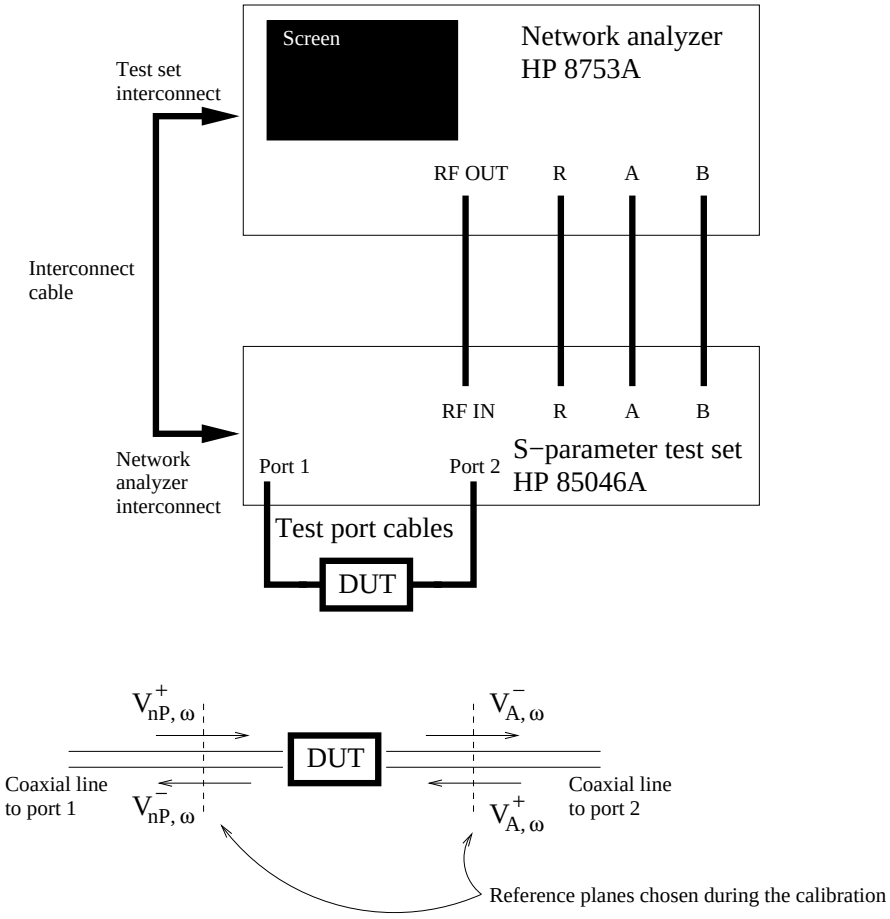

Figure C.1: The used measurement setup with the network analyzer HP 8753A and the S-parameter test set HP 85046A.

transmission uncertainty. During the measurements procedure errors are measured in addition to the desired S-parameters. Using Figure C.2 the measured reflection coefficient is written as

$$\left.\frac{b_{nP,\omega}}{a_{nP,\omega}}\right|_{a_{A,\omega}=0} = S_{nPP,\omega} + [\text{Additional error terms}], \tag{C.5}$$

and the measured transmission coefficiet is written as

$$\left.\frac{b_{A,\omega}}{a_{nP,\omega}}\right|_{a_{A,\omega}=0} = S_{nAP,\omega} + [\text{Additional error terms}]. \tag{C.6}$$

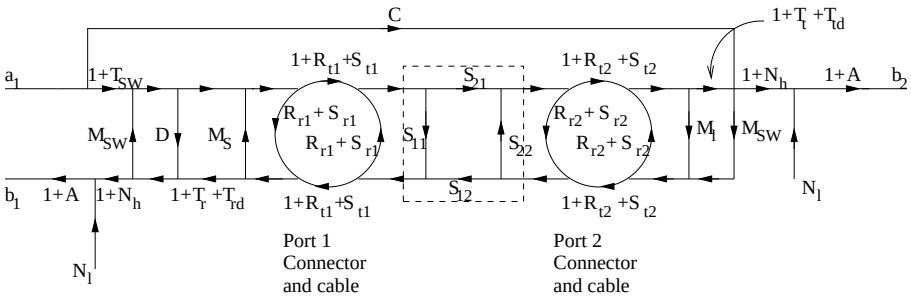

Figure C.2: System error model for the network analyzer HP 8753A and S-parameter set HP 85046A as suggested in the system operating and programming manual [68].

Only first order terms and the significant second order terms the systematic error are considered and the errors are devided into systematic and random errors. Table C.3 shows typical figures for the configuration.

C.1.1 Reflection Uncertainty Equations

The uncertainty of the measured amplitude of the reflections coefficient $S_{nPP,\omega}$ is considered in this Section. The random errors are divided into the following four types:

1) The random low-level noise

$$W_r = 3N_l. \tag{C.7}$$

2) The random high-level noise

$$X_r = 3N_h|S_{nPP,\omega}|. \tag{C.8}$$

3) The random port 1 repeatability

$$Y_r = 3R_{r1} + 2R_{t1}|S_{nPP,\omega}| + R_{r1}|S_{nPP,\omega}|^2. \tag{C.9}$$

4) The random port 2 repeatability

$$Z_r = R_{r2}|S_{nPA,\omega}||S_{nAP,\omega}| \tag{C.10}$$

The systematic error is given by

$$\begin{aligned} S_r = (1 + T_{SW})(D + S_{r1}) &+ (T_{SW} + T_r)|S_{nPP,\omega}| \\ &+ (M_{SW} + M_s + S_{r1})|S_{nPP,\omega}|^2 \\ &+ M_l|S_{nPA,\omega}||S_{nAP,\omega}| + A_m|S_{nPP,\omega}|, \end{aligned} \tag{C.11}$$

A_m	Amplitude of dynamic accuracy
A_p	Phase of dynamic accuracy
N_l	Noise floor
N_h	High level noise
T_{SW}	Switch tracking
M_{SW}	Switch port match
R_r	Reflection repeatability
T_r	Transmission repeatability
$T_{rd,m}$	Amplitude of reflection tracking drift
$T_{rd,p}$	Phase of reflection tracking drift
$T_{td,m}$	Amplitude of the transmission tracking drift
$T_{td,p}$	Phase of the transmission tracking drift
D	Residual directivity
M_s	Residual source match
M_l	Residual load match
C	Residual crosstalk
T_r	Residual reflection tracking
T_t	Residual transmission tracking
S_r	Cable reflection stability
S_t	Cable transmission stability

the total amplitude uncertainty $E_{r,m}$ of the reflection amplitude $|S_{nPP,\omega}|$ is given by

$$E_{r,m} = S_r + \sqrt{W_r^2 + X_r^2 + Y_r^2 + Z_r^2} + |S_{nPP,\omega}|T_{rd,m}. \tag{C.12}$$

The total reflection phase uncertainty $E_{r,p}$ is determined from a comparison of the amplitude uncertainty $E_{r,m}$ with the signal amplitude $|S_{nPP,\omega}|$. The total reflection phase uncertainty is given by

$$E_{r,p} = \arcsin\left(\frac{S_r + \sqrt{W_r^2 + X_r^2 + Y_r^2 + Z_r^2}}{|S_{nPP,\omega}|}\right) + T_{rd,p} + 2S_{t1} + A_p. \tag{C.13}$$

In Figure C.3 the amplitude uncertainty $E_{r,m}$ for $S_{nPP,\omega}$ is plotted as a function of the amplitude $|S_{nPP,\omega}|$. The uncertainty is monotonous increasing from 0.02 at $|S_{nPP,\omega}| = 0$ to 0.07 at $|S_{nPP,\omega}| = 1$ so that the relative uncertainty is high at low amplitudes of the the reflection coefficient $S_{nPP,\omega}$. In Figure C.4 the phase uncertainty $E_{r,p}$ for $S_{nPP,\omega}$ is plotted as a function of the amplitude $|S_{nPP,\omega}|$. The monotonous decreasing from $E_{r,p} = 25^o$ at $|S_{nPP,\omega}| = 0.05$ to $E_{r,p} = 4.3^o$ at $|S_{nPP,\omega}| = 1$. Therefore, for this configuration the uncertainties are reasonable for high amplitudes of the reflection coefficient $S_{nPP,\omega}$. Using a maximum uncertainty of 10^o the measurements are usable for $|S_{nPP,\omega}| > 0.13$.

Directivity	D	0.01/0.018 *)
Crosstalk	C	0.00001
Reflection tracking	T_r	0.016
Transmission tracking	T_t	0.01
Source match	M_s	0.032
Load match	M_l	0.032
Amplitude of dynamic accuracy amplitude	A_m	0.0008
Phase of dynamic accuracy amplitude	A_p (Deg)	0.08
Switch tracking	T_{SW}	0
Switch port match	M_{SW}	0
Noise level	N_l	0.00003
High level noise	N_h	0.00046
Connector reflection repeatability	R_r	0
Connector transmission repeatability	R_t	0
Amplitude of reflection tracking drift (ΔT in K)	$T_{tr,m}$	$0.0015\Delta T$
Phase of reflection tracking drift (ΔT in K, f in GHz)	$T_{tr,p}$ (Deg)	$(0.1 + 0.15f)\Delta T$
Amplitude of transmission tracking drift (ΔT in K)	$T_{td,m}$	$0.0015\Delta T$
Phase of transmission tracking drift (ΔT in K, f in GHz)	$T_{td,p}$ (Deg)	$(0.1 + 0.15f)\Delta T$
Port 1, cable reflection amplitude stability	S_{r1}	0.00032
Port 1, cable transmission phase stability (f in GHz)	S_{t1} (Deg)	$0.05f$
Port 2, cable reflection amplitude stability	S_{r2}	0.00032
Port 2, cable transmission phase stability (f in GHz)	S_{t2} (Deg)	$0.05f$

Table C.3: Typical performance figures for the HP 8753A used with the HP 85046A test set for measuring 3.5 mm devices and the intermediate frequency bandwidth (IF BW) at 10 Hz [68, Page 38]. *) The directivity D is 0.01 from 300 kHz to 1.3 GHz and 0.018 from 1.3 GHz to 3 GHz. The phase drift with temperature was arrived at using the HP 11857D cables and a full two-port calibration.

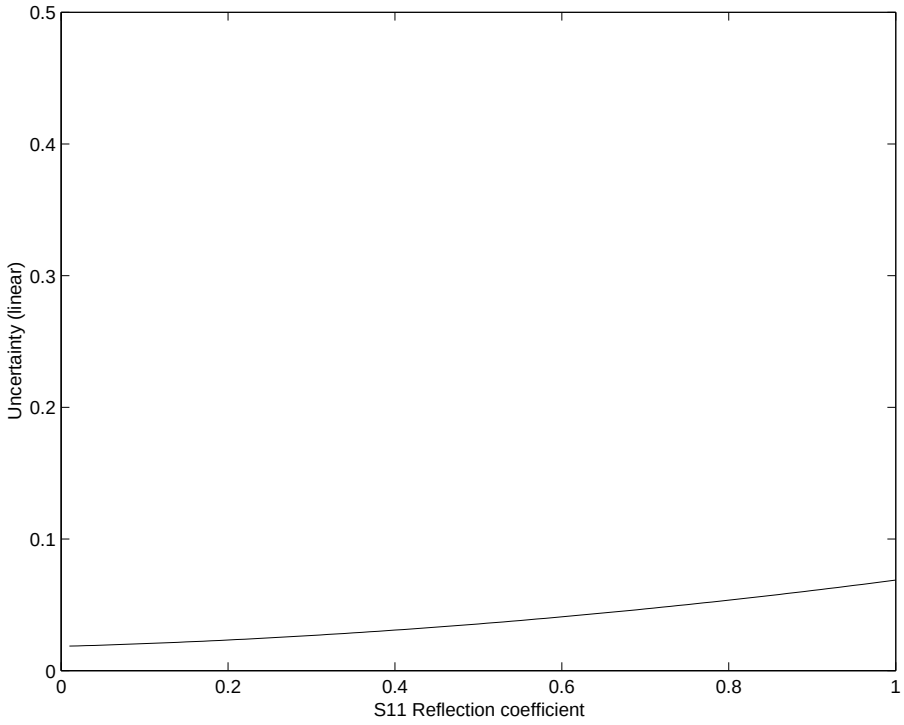

Figure C.3: The amplitude uncertainty $E_{r,m}$ as a function of the the amplitude $|S_{nPP,\omega}|$. The considered frequency is $f = 3$ GHz, the temperature drift is $\Delta T = 0$, and the transmission coefficients is $S_{nPA,\omega} = S_{nAP,\omega} = 0$.

C.1.2 Transmission Uncertainty Equations

The uncertainty of the measured amplitude of the transmission coefficient $S_{nAP,\omega}$ is considered in this Section. The random errors are devieded into the following four types:
1) The random low-level noise

$$W_r = 3N_l. \tag{C.14}$$

2) The random high-level noise

$$X_r = 3N_h|S_{nPP,\omega}|. \tag{C.15}$$

3) The random port 1 repeatability

$$Y_r = 3R_{r1} + 2R_{t1}|S_{nPP,\omega}| + R_{r1}|S_{nPP,\omega}|^2. \tag{C.16}$$

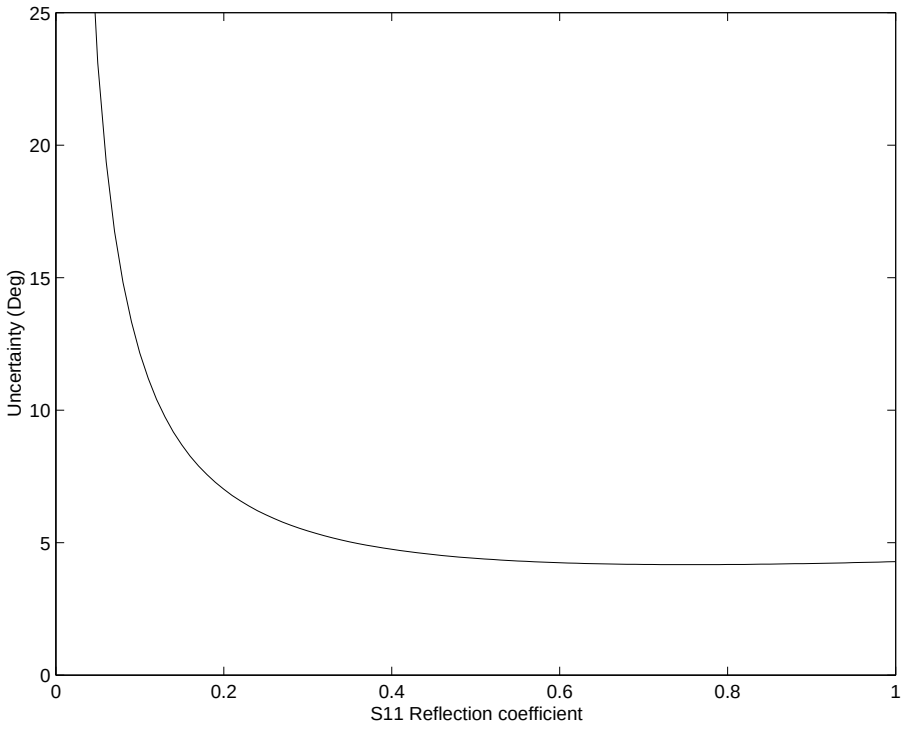

Figure C.4: The phase uncertainty $E_{r,p}$ as a function of the the amplitude $|S_{nPP,\omega}|$. The considered frequency is $f = 3$ GHz, the temperature drift is $\Delta T = 0$, and the transmission coefficients is $S_{nPA,\omega} = S_{nAP,\omega} = 0$.

4) The random port 2 repeatability

$$Z_r = R_{r2}|S_{nPA,\omega}||S_{nAP,\omega}| \tag{C.17}$$

The systematic error is given by

$$\begin{aligned} S_t = C + (T_{SW} + T_t)S_{nAP,\omega} + (M_{SW} + M_s + S_{r1})S_{nPP,\omega}S_{nAP,\omega} \\ + (M_{SW} + M_s + S_{r2})S_{nPA,\omega}S_{AA,\omega} + A_m S_{nAP,\omega}, \end{aligned} \tag{C.18}$$

the total amplitude uncertainty $E_{t,m}$ of the reflection amplitude $|S_{nAP,\omega}|$ is given by

$$E_{t,m} = S_t + \sqrt{W_r^2 + X_r^2 + Y_r^2 + Z_r^2} + |S_{nAP,\omega}|T_{td,m}. \tag{C.19}$$

The total reflection phase uncertainty $E_{t,m}$ of $S_{nAP,\omega}$ is given by

$$E_{t,p} = \arcsin\left(\frac{S_t + \sqrt{W_r^2 + X_r^2 + Y_r^2 + Z_r^2}}{|S_{nAP,\omega}|}\right) + T_{td,p} + S_{t1} + S_{t2} + A_p. \tag{C.20}$$

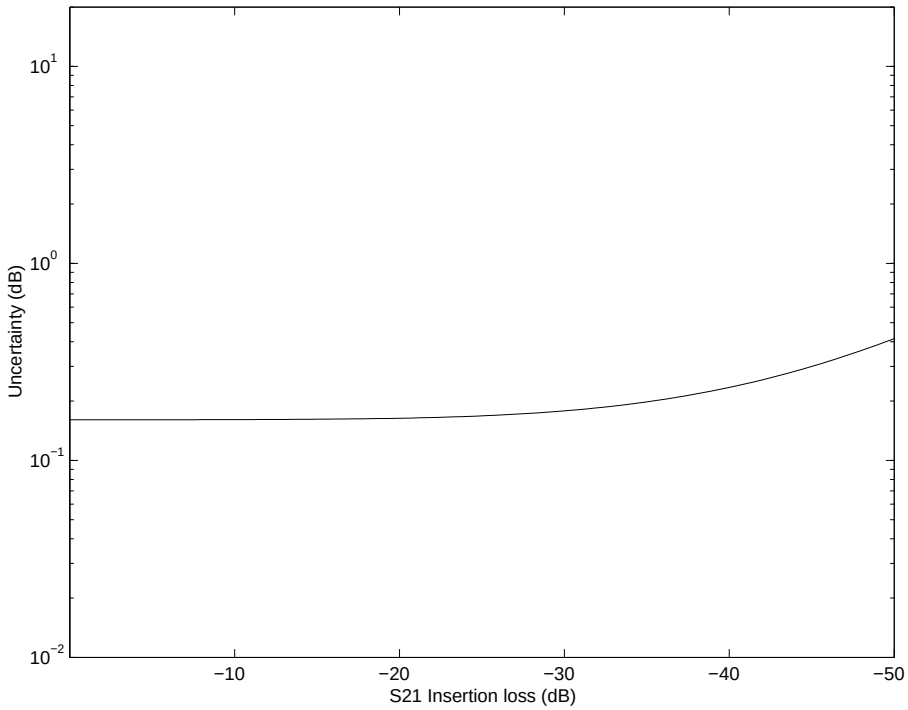

Figure C.5: The amplitude uncertainty $E_{t,m}$ as a function of the the amplitude $|S_{nAP,\omega}|$. The considered frequency is $f = 3$ GHz, the temperature drift is $\Delta T = 0$, and the amplitude of the reflection coefficients is $|S_{AA,\omega}| = |S_{nPP,\omega}| = 0.1$.

In Figure C.5 the amplitude uncertainty y $E_{t,m}$ for $S_{nAP,\omega}$ is plotted as a function of the amplitude $|S_{nAP,\omega}|$. The uncertainty is monotonous descreasing from 0.4 dB at $|S_{nAP,\omega}| = -50$ dB to 0.16 dB at $|S_{nAP,\omega}| = 0$ dB.

In Figure C.6 the phase uncertainty y $E_{t,p}$ for $S_{nAP,\omega}$ is plotted as a function of the amplitude $|S_{nAP,\omega}|$. The uncertainty is monotonous descreasing from 3^o at $|S_{nAP,\omega}| = -50$ dB to 1.2^o at $|S_{nAP,\omega}| = 0$ dB. Therefore, the measurements of transmission coefficient is usable for the amplitudes in the range -50 dB $< |S_{nAP,\omega}| <$ 0 dB.

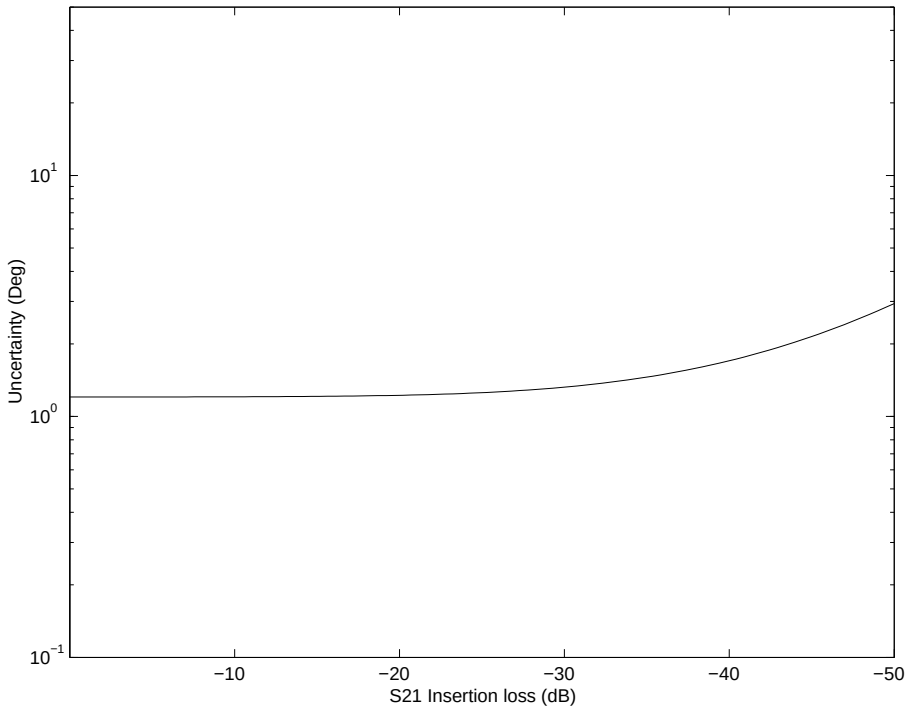

Figure C.6: The phase uncertainty $E_{t,p}$ as a function of the the amplitude $|S_{nAP,\omega}|$. The considered frequency is $f = 3$ GHz, the temperature drift is $\Delta T = 0$, and the amplitude of the reflection coefficients is $|S_{AA,\omega}| = |S_{nPP,\omega}| = 0.1$.

References

[1] D.J. Daniels, *Ground Penetrating Radar*, The Institution of Electrical Engineers IEE, London, UK, 2 edition, 2004.

[2] E.S. Eide and J.F. Hjelmstad, "3D utility mapping using electronically scanned antenna array," *Proceedings of SPIE- The International Society for Optical Engineering*, vol. 4758, pp. 192–196, 2002.

[3] G. Jung, J. Jung, S. Cho, and H. Kim, "Evaluation of road settlements on soft ground from GPR investigation," in *10th International Conference on Ground Penetrating Radar*, Delft University of Technology, June 2004, vol. 2, pp. 651–654.

[4] C. Bristow, "GPR in sediments: Recent advances in stratigraphic applications," in *10th International Conference on Ground Penetrating Radar*, Delft University of Technology, June 2004, vol. 2, pp. 569–572.

[5] J.A. Doolittle, F.E. Minzenmayer, S.W. Waltman, and E.C. Benham, "Ground penetrating radar soil suitibility maps," *Journal of Environmental and Engineering Geophysics*, vol. 8, pp. 49–56, June 2003.

[6] L.B. Conyers, "Moisture and soil differences as related to the spatial accuracy of GPR amplitude maps at two archaeological test sites," in *10th International Conference on Ground Penetrating Radar*, Delft University of Technology, June 2004, vol. 2, pp. 435–438.

[7] V.L. Mironov, M.C. Dobson, V.H. Kaupp, S.A. Komarov, and V.N. Kleshchenko, "Generalized refractive mixing dielectric model for moist soils," *Geoscience and Remote Sensing Symposium*, vol. 6, pp. 3556–3558, June 2002.

[8] M.I. Skolnik, *Introduction to Radar Systems*, McGraw-Hill, Singapore, 2 edition, 1981.

[9] A. Schatzberg and A.J. Deveney, "Super-resolution in diffraction tomography," *Inverse Problems*, vol. 8, pp. 149–164, 1992.

[10] M. Sato, Y. Hamada, X. Feng, F. Kong, Z. Zeng, and G. Fang, "GPR using an array antenna for landmine detection," *Near Surface Geophysics*, vol. 2, pp. 7–13, Feb. 2004.

[11] Y. Wakita, H. Yamada, and Y. Yamaguchi, "Soil parameter estimation technique using a dipole antenna," *Electronics and Communications in Japan*, vol. 83, pp. 60–68, 2000.

[12] H. Schantz, *The Art and Science of Ultrawideband Antennas*, Artech House, USA, 2005.

[13] E. S. Eide, "Ultra-wideband transmit/receive antenna pair for ground penetrating radar," *IEE Proceedings Microwaves, Antennas and Propagation*, vol. 147, pp. 231–235, June 2000.

[14] E. S. Eide, "An ultra wideband antenna array for ground penetrating radar," in *AP2000: Millenium Conference on Antennas and Propagation*, Davos, Switzerland, Apr. 2000.

[15] A.A. Lestari, A.G. Yarovoy, and L.P. Ligthart, "Numerical and experimental analysis of circular-end wire bow-tie antennas over a lossy ground," *IEEE Transactions on Antennas and propagation*, vol. 52, pp. 26–35, Jan. 2004.

[16] A.A. Lestari, A.G. Yarovoy, and L.P. Lighthart, "Capacitively-tapered bowtie antenna," in *Conference Proceedings on CD-ROM, Millennium Conference on Antennas and Propagation*, Davos, Switzerland, Apr. 2000.

[17] A.G. Yarovoy and L.P. Lighthart, "Ultra-wideband antennas for ground penetrating radar," in *Proceeding International Sympoosium on Antennas for Radar Earth Observation, Symposium*, Delft University of Technology, The Netherlands, June 2000.

[18] J. Thaysen, H. Lenler-Eriksen, and K.B. Jakobsen, "Wideband cavity backed spiral antenna for stepped frequency ground penetrating radar," *IEEE Antennas and Propagation Society International Symposium*, vol. 1B, pp. 418–421, 2005.

[19] A.G. Yarovoy, R.V. De Jongh, and L.P. Lighthart, "Ulta-wideband sensor for electromagnetic field measurements in time domain," *Electronics Letters*, vol. 36, pp. 1679–1680, Sept. 2000.

[20] R.V. De Jongh, A.G. Yarovoy, and L.P. Lighthart, "Experimental set-up for measurement of GPR antenna radiation patterns," in *Proceeding of the 28th European Microwave conference*, Amsterdam, The Netherlands, Oct. 1998, vol. 2, pp. 539–543.

[21] D.M. Kerns, "Plane-wave scattering-matrix theory of antennas and antenna-antenna interactions," in *National Bureau of Standards*, Washington, DC, USA. Monograph 162, 1981.

[22] P. Meincke and T.B. Hansen, "Plane-wave characterization of antennas close to a planar interface," *IEEE Transactions on Geoscience and Remote Sensing*, vol. 42, pp. 1222–1232, June 2004.

[23] E. Eide, "Radar imaging of small objects closely below the earth surface," *Ph.D. thesis, Institutt for teleteknikk, Norges teknisk-naturvitenskapelige universitet (NTNU), Trondheim*, 2000, Doktor ingeniøravhandling 2000:72.

[24] P. Meincke and T.B. Hansen, "Inversion scheme for ground penetrating radar that takes into account the planar air-soil interface," *IEEE Transactions on Geoscience and Remote Sensing*, vol. 38, pp. 496–506, Jan. 2000.

[25] P. Meincke, "Linear GPR imaging based on electromagnetic plane-wave spectra and diffraction tomography," in *Proceedings of the Tenth International Conference on Ground Penetrating Radar*, Delft, Netherlands, June 2004, vol. 1, pp. 55–58.

[26] T.B. Hansen and A.D. Yaghjian, *Plane-Wave Theory of Time-Domain Fields: Near-Field Scanning Applications*, The IEEE Press Series on Electromagnetic Wave Theory, New York, USA, 1999.

[27] H. Lenler-Eriksen and P. Meincke, "Ground penetrating radar antenna measurements based on plane-wave expansions," *IEEE APS-S International Symposium*, vol. 1A, pp. 214–217, 2005.

[28] E. Jørgensen, "Higher-order integral equation methods in computational electromagnetics," *Ph.D. thesis, Electromagnetic Systems, Ørsted·DTU*, May 2003.

[29] H. Lenler-Eriksen, P. Meincke, and E. Jørgensen, "Estimation of constitutive parameters using a loop antenna," in *2nd International Workshop on Advanced GPR (IWAGPR)*, Delft, Netherlands, May 2003, pp. 207–211.

[30] H. Lenler-Eriksen and P. Meincke, "Estimation of complex permittivity using loop antenna," *Electronics Letters*, vol. 40, pp. 285–287, Mar. 2004.

[31] H. Lenler-Eriksen, P. Meincke, A. Sarri, V. Chatelée, B. Nair, I. Craddock, G. Alli, J. Dauvignac, Y. Huang, D. Lymperopoulos, and R. Nilavalan, "Joint ACE ground penetrating radar antenna test facility at the Technical University of Denmark," *IEEE AP-S International Symposium*, vol. 4A, pp. 109–111, jul 2005.

[32] H. Lenler-Eriksen and P. Meincke, "The ACE-DTU planar near-field ground penetrating radar antenna test facility," in *Proceedings of 13th International Symposium on Antennas (JINA)*, Nice, France, Nov. 2004, pp. 368–369.

[33] H. Lenler-Eriksen and P. Meincke, "Measurement of plane-wave spectra of ground penetrating radar antennas," *Microwave and Optical Technology Letters*, pp. 215–216, Feb. 2005.

[34] P. Meincke, O. Kim, and H. Lenler-Eriksen, "Including arbitrary antenna patterns in microwave imaging of buried objects," *URSI International Conference on Electromagnetic Theory*, vol. 2, pp. 1200–1202, 2004.

[35] J. Appel-Hansen, "Notes for the course 48318 advanced field theory, FN 155," Tech. Rep., Technical University of Denmark, Lyngby, Denmark, 2000.

[36] D.M. Kerns, "Analytical techniques for the correction of near-field antenna measurements made with an arbitrary but known measuring antenna," in *Abstracts of URSI-IRE Meeting*, Washington, DC, USA, Apr. 1963, pp. 6–7.

[37] D.M. Kerns, "Correction of near-field antenna measurements made with an arbitrary but known measuring antenna," *Electronics Letters*, vol. 6, pp. 346–347, May 1970.

[38] T.B. Hansen and A.D. Yaghjian, "Formulation of probe-corrected planar near-field scanning in the time domain," *IEEE Transactions on Antennas and Propagation*, vol. 43, pp. 569–584, June 1995.

[39] J. Appel-Hansen, E.S. Gillespie, T.G. Hickman, and J.D. Dyson, "Antenna measurements," in *The Handbook of Antenna Design*, A.W. Rudge, K. Milne, A.D. Olver, and P. Knight, Eds., vol. 1, Chapter 8. Short Run Press Ltd., England, 1982.

[40] A.D. Yaghjian, "An overview of near-field antenna measurements," *IEEE Transactions on Antennas and Propagation*, vol. AP-34, pp. 30–45, Jan. 1986.

[41] R.V. de Jongh, A.G. Yarovoy, L.P. Ligthart, I.V. Kaploun, and A.D. Schukin, "Design and analysis of new GPR antenna concepts," in *Proceedings of GPR'98, 7th International Conference on Ground Penetrating Radar*, Lawrence, Kansas, USA, May 1998, vol. 1, pp. 81–86.

[42] A.G. Yarovoy, P. Aubry, and L.P. Lighthart, "GPR antenna measurement in time domain," in *Conference proceedings on CD-ROM, Millennium Conference on Antennas and Propagation - AP2000*, Davos, Switzerland, Apr. 2000.

[43] C.A. Balanis, *Antenna Theory, Analysis and Design*, John Wiley, USA, 2 edition, 1997.

[44] "IEEE standard definitions of terms for antennas," IEEE Std 145-1993, published by the Institute of Electrical and Electronics Engineers, Inc., 345 East 47th Street, New York, NY 10017, USA, June 1993.

[45] T. T. Wu, "Theory of the thin circular loop antenna," *Journal of Mathematical Physics*, vol. 3, pp. 1301–1304, 1962.

[46] J. van der Kruk, C.P.A. Wapenaar, J.T. Fokkema, and P.M. van den Berg, "Improved three-dimensional image reconstruction technique for multi-component

ground penetrating radar data," *Subsurface Sensing Technologies and Applications*, vol. 4, pp. 61–99, Jan. 2003.

[47] S. Adachi and Y. Mushiake, "Studies of large circular loop antennas," in *Reports of the Research Institute of Electrical Communication*, Tohoku University, Series B, 1957, vol. 9, pp. 79–103.

[48] J.J. Goedbloed, *Electromagnetic Compatibility*, Chapter 2, pp. 40–44, Prentice Hall, New York, 1992.

[49] D.M. Pozar, *Microwave Engineering*, Chapter 4, Wiley, USA, 2 edition, 1998.

[50] E. Jørgensen, J.L. Volakis, P. Meincke, and O. Breinbjerg, "Higher order hierarchical Legendre basis functions for electromagnetic modeling," *IEEE Transactions on Antennas and Propagation*, vol. 52, pp. 2985–2995, 2004.

[51] M.N. Afsar, J.R. Birch, and R.N. Clarke, "The measurement of the proporties of materials," *Proceedings of the IEEE*, vol. 74, pp. 183–199, Jan. 1986.

[52] W.R. Scott and G.S. Smith, "Measured electrical constitutive parameters of soil as functions of frequency and moisture content," *IEEE Transactions on Geoscience and Remote Sensing*, vol. 30, pp. 621–623, 1992.

[53] T.J. Heimovaara, "Frequency domain analysis of time domain reflectrometry waveforms, 1. measurement of the complex dielectric permittivity of soils," *Water Resources Research*, pp. 189–200, 1994.

[54] W.G. Fano and V. Trainotti, "Dielectric properties of soils," *Conference on Electrical Insulation and Dielectric Phenomena*, pp. 75–78, Oct. 2001.

[55] D.L. Herrick, "A vertical slotted cylinder array for subsurface moisture profiling," *IEEE 1978 Region 6 Conference Record 'Electronics for Resources Management'*, pp. 98–100, 1978.

[56] R.C. Jain and W.A.G. Voss, "Dielectric measurement methods for industial scientific and medical applications in microwave frequency range," *IETE Technical Review*, vol. 11, pp. 297–311, 1994.

[57] R.C. Weast, Ed., *Handbook of Chemistry and Physics*, CRC Press, Florida, 1 edition, 1990.

[58] V.L. Mironov and P.P. Bobrov, "Soil dielectric spectroscopic parameters dependence on humus content," *Geoscience and Remote Sensing Symposium*, vol. 2, pp. 1106–1108, 2003.

[59] V.L. Mironov, M.C. Dobson, V.H. Kaupp, S.A. Komarov, and V.N. Kleshchenko, "Generalized refractive mixing dielectric model for moist soils," *IEEE Transactions on Geoscience and Remote Sensing*, vol. 42, pp. 773–785, Apr. 2004.

[60] J.E. Hipp, "Soil electromagnetic parameters as functions of frequency, soil density, and soil moisture," *Proceedings of the IEEE*, vol. 62, pp. 98–103, Jan. 1974.

[61] P.K. Bhagat and P.K. Kadaba, "Relaxation models for moist soils suitable at microwave frequencies," *Material Science and Engineering*, vol. 28, pp. 47–51, 1977.

[62] P. Hoekstra and A. Delaney, "Dielectric proporties of soils at uhf and microwave frequencies," *Journal of Geophysical Research*, vol. 79, pp. 1699–1708, Apr. 1974.

[63] M. Hallikainen, F.T. Ulaby, L. Wu, M.C. Dobson, and M. El-Rayes, "Microwave dielectric behavior of wet soil- part I: Empirical models and experimental observations," *IEEE transactions on Geoscience and Remote Sensing*, vol. GE-23, pp. 25–34, Jan. 1985.

[64] M.C. Dobson, F.T. Ulaby, M.T. Hallikainen, and M.A. El-Rayes, "Microwave dielectric behavior of wet soil- part II: Dielectric mixing models," *IEEE Transactions on Geoscience and Remote Sensing*, vol. GE-23, pp. 35–46, Jan. 1985.

[65] D. Wobshall, "A theory of the complex dielectric permittivity of soil containing water: The semidisperse model," *IEEE Transactions on Geoscience Electronics*, vol. GE-15, pp. 49–58, Jan. 1977.

[66] T.J. Heimovaara, W. Bouten, and J.M. Verstraten, "Frequency domain analysis of time domain reflectrometry waveforms, 2. a four-component complex dielectric mixing model for soils," *Water Resources Research*, pp. 201–210, 1994.

[67] A.A. Asheko and K.E. Nemchenko, "Relaxation parameters in the main dispersion range of water," *Journal of Molecular Liquids*, vol. 105, pp. 295–298, 2003.

[68] Hewlett Pachard, USA, *System operating and programming manual, HP8753A Network Analyzer, General Information and Specifications including System Performance*, June 1986, Manual Part No. 08753-90003.

[69] JVL Industi Elektronik A/S, Danmark, *DMC10, DC-Servomoter Controller, Bruger Manual*, Jan. 1995.

[70] BAHR Modultechnik, *Positioning system ELZ 30, 40, 60, 80, 80S, 100, 125*.

[71] Tecnoingranaggi Riduttori, *Precision Planetary Gear Reducer*, Nov. 1998.

[72] J.D. Dyson, "Equiangular spiral antenna," *IRE Transactions on Antennas and Propagation*, vol. AP-7, pp. 181–187, Apr. 1959.

[73] M. Sato and X. Feng, "GPR migration algorithm for landmines buried in inhomogeneous soil," *2005 IEEE Antennas and Propagation Society, International Symposium*, vol. 1B, pp. 206–209, July 2005.

[74] R.W. Deming and A.J. Devaney, "Diffraction tomography for multi-monostatic ground penetrating radar imaging," *Inverse Problems*, vol. 13, pp. 29–45, 1997.

[75] P. Meincke, "Linear GPR inversion for lossy soil and a planar air-soil interface," *IEEE Transactions on Geoscience and Remote Sensing*, vol. 39, pp. 2713–2721, Dec. 2001.

[76] P.C. Hansen, *Rank-Deficient and Discrete Ill-Posed Problems, numerical aspects of linear inversion*, Socity for Industrial and Applied Mathematics (SIAM), Philadelphia, USA, 1997.

[77] K.W.A. van Dongen, P.M. van den Berg, and I. Nicolaescu, "Subsurface imaging using measured near-field antenna footprints," *Near Surface Geophysics*, vol. 2, pp. 33–39, Feb. 2004.

[78] P. Meincke and O. Kim, "Accurate antenna models in ground penetrating radar diffraction tomography," *IEEE Antennas and Propagation Society International Symposium*, vol. 4, pp. 306–309, June 2002.

[79] J. van der Kruk, "Three-dimensional GPR imaging in the horizontal wavenumber domain for different heights of source and receiver antenna," *Near Surface Geophysics*, vol. 2, pp. 25–31, Feb. 2004.

[80] J. van der Kruk, "Multi-component GPR imaging for different heights of source and receiver antennas," in *2nd International Workshop on Advanced GPR*, Delft, The Netherlands, May 2003, pp. 189–194.

[81] T.B. Hansen and P. Meincke, "Scattering from a buried circular cylinder illuminated by a three-dimentional source," *Radio Science*, vol. 37, pp. 41–423, 2002.

[82] S. Tjora, E. S. Eide, and L. Lundheim, "Evaluation of methods for ground bounce removal in GPR utility mapping," in *10th International Conference on Ground Penetrating Radar*, Delft University of Technology, June 2004, vol. 1, pp. 379–382.

[83] M.J. Cloud and E. Rothwell, *Electromagnetics*, vol. 2, Chapter 2.2.2, Electrical Engineering Textbook Series, 2001.

[84] R.W. King and G.S. Smith, *Antennas in Matter, Fundamentals, Theory, and Applications*, Chapter 12, pp. 727–736, The MIT Press, England, 1981.

[85] Agilent Technologies, USA, *Operating and Service Manual, Agilent Technologies 85046A/B S-Parameter Test Set*, Apr. 1999, Manual Part No. 08753-90003.